2009

FIRST AEROSOL MEASUREMENTS WITH THE PURPLE CROW LIDAR: LOFTED PARTICULATE MATTER STRADDLING THE STRATOSPHERIC BOUNDARY

Paul J. Doucet

FIRST AEROSOL MEASUREMENTS WITH THE PURPLE CROW LIDAR: LOFTED PARTICULATE MATTER STRADDLING THE STRATOSPHERIC BOUNDARY

(Spine title: First Aerosol Measurements with the Purple Crow Lidar)

(Thesis format: Monograph)

by

Paul J. Doucet

Graduate Program in Physics

Submitted in partial fulfillment

of the requirements for the degree of

Master of Science

The School of Graduate and Postdoctoral Studies

The University of Western Ontario

London, Ontario, Canada

Abstract

Independent aerosol backscatter and extinction measurements with the high power-aperture Purple Crow Lidar (42.87 deg N, 81.38 deg W, 225 m) are obtained for the first time. This is achieved through application of a Raman-Lidar technique for determining the field of view of the rotating liquid mercury mirror, and through development of a novel method for isolating the attenuation behaviour of the low-altitude mechanical signal chopper.

Eleven nights of high-altitude (> 12 km) aerosol observations are presented with measurements of the intrinsic extinction-to-backscatter aerosol ratio (Lidar ratio). These include cirrus clouds, smoke near the tropopause from biomass burning during June-July 2002 and stratospheric aerosols from the Kasatochi volcanic eruption of August 2008. Detailed structure in the Lidar ratio, reflecting physical particle properties, is observed – in contrast to the single value often assumed by Rayleigh Lidars.

A coincidental measurement by the space-borne Calipso Lidar is found to have good agreement.

Keywords: Purple Crow Lidar, aerosols, atmosphere, backscatter, attenuation, Lidar ratio, stratospheric aerosols, Kasatochi, volcano, biomass burning, smoke, PyroCB, pyrocumulonimbus, Raman Lidar, Mie scattering, Rayleigh scattering, Raman scattering

Acknowledgements

I would like to thank my lab-mates Andy, Emily and Blessing for their help over the years, as well as the many student observers for their many late nights spent collecting Lidar data.

I would also like to gratefully acknowledge the contribution by the Meteological Service of Canada and the World Ozone and Ultraviolet Radiation Data Centre for furnishing ozonesonde data, and the many contributions by Dr. Argall to the construction of the Lidar and the development of analysis code. I am further thankful to Mr. Mike Fromm for his correspondences on the subject of PyroCBs and for alerting us to their presence in our data.

Finally I would like to extend thanks to my supervisor, Prof. Sica.

This work is dedicated to my loving parents, John and Pauline.

Contents

List of Tables

List of Figures

List of Symbols

- z Vertical altitude above Lidar
- λ_0 Source laser wavelength
- λ_R A Raman-shifted wavelength of the source laser
- λ_{N2} Specific N_2 Raman shifted wavelength
- β Backscatter coefficient
- α Extinction coefficient (synonym: Attenuation coefficient)
- γ Extinction-to-Backscatter ratio (synonyms: Lidar ratio, Aerosol ratio)
- K A constant
- $O(z)$ Geometric overlap function
- $S(z)$ Shutter function (defined in text)
- $R(z)$ Aerosol Scattering Ratio, total amount of backscatter relative to Rayleigh background
- $\mathbf{P}(z)$ Measured laser power (photocounts)
- $\mathbf{T}(z)$ Transmission factor (integral of α from ground to altitude z).

Chapter 1

Introduction

Aerosols represent what is arguably the most important and variable influence on the optical properties of the atmosphere – as any dreary, overcast day will illustrate. Aerosols consist of all solid and liquid particulate matter in the atmosphere – including water droplets, ice crystals, cloud condensation nuclei, smoke, dust, marine and anthropogenic aerosols. They are important to many areas such as regional weather, global climate, air quality, and atmospheric chemistry. Lidar (Light Detection and Ranging) systems are the instrument of choice for many remote sounding aerosol studies, due to their accurate ranging capabilities and the direct acquisition of optical measurements that are often the focus of the investigation. The fundamental Lidar quantities are backscatter – the amount of light received by the detectors as a result of scattering by the constituents in some volume being excited by laser – and extinction (or attenuation) – the amount of light removed by those same constituents.

Rayleigh / Mie scattering Lidars that measure elastic laser backscatter exclusively are the most common design due to their simplicity. They ben-

efit from strong elastically-scattered signals, however extinction values must be inferred from the backscattered data (Klett, 1981) with considerable uncertainty. This uncertainty can be reduced using multi-angle measurements (Reagan et al., 1988).

Most Lidars designed for aerosol measurements have a lower power-aperture and operate within the planetary boundary layer and lower troposphere. Raman Lidars, that measure inelastic Raman-shifted backscatter by molecules at characteristic wavelengths, are able to determine both aerosol extinction and backscatter.

The technique for using Raman Lidars to measure aerosols, described in Ansmann et al. (1990), provides a method for independently measuring the aerosol extinction. In this seminal paper, a 308 nm XeCl laser was used to obtain an extinction profile between 0-8 km using a 20 minute average of an aerosol feature with peak aerosol extinction of 0.6 km^{-1}. This was followed by more detailed measurements by Ansmann et al. (1992). In this follow up, a cirrus cloud between 8-10 km was measured as having a peak extinction of 0.8 km^{-1}. The extinction to backscatter ratio – a useful indicator of the particle size, shape and orientation that is also referred to as the Lidar ratio – was measured to be 15.5 sr (steradians). No significant change in the Lidar ratio was detected when the Lidar was tilted from the vertical, implying that there was little specular reflection from large horizontally-oriented ice crystals.

In Ferrare et al. (2001), the average Lidar ratio between 1-6 km over 212 days was measured from north central Oklahoma at 355 nm. A mean value of 68 sr was found, with higher values during high aerosol optical thickness and humidity. Ratios below 60 sr were associated with air masses from the rural westerly direction, while values above 60 sr tended to originate from the more urban eastward direction.

Several observations of low-altitude smoke with Lidar ratios between 50-90 sr were made by Amiridis et al. (2009) at 355 nm. Detailed extinction studies have been made of cirrus clouds near the tropopause (Ansmann et al., 1992), which are important climate change inputs (Solomon et al., 2007). Raman Lidar measurements were taken of stratospheric aerosols with a XeCl laser at 308 nm following the eruption of Mount Pinatubo (Ansmann et al., 1993), where Lidar ratio values between 10-90 sr with a mean of 25 sr were observed.

The Purple Crow Lidar (PCL) has a record of over 300 nights of fair-weather observations since the installation of the Raman detector channels (Argall et al., 2007). Aerosols have been qualitatively observed in the data but no formal quantitative analysis applied. These observations included high-altitude layers of diffuse particulate matter near the tropopause believed to be smoke originating from violent updraft events of intense forest fires, termed pyro-cumulonimbus (PyroCB) events due to their vertical development and resemblance to cumulonimbus clouds. No direct measurements of aerosol extinction and the corresponding extinction-to-backscatter ratio of PyroCB layers were found in various publication searches.

Several parameters must first be calibrated before a method for measuring aerosols can be applied to the PCL data. The goal of this work is to perform these necessary calibrations and extract meaningful aerosol measurements from the existing record of PCL data, with design and operational recommendations for improving aerosol measurements in the future.

1.1 Lidar Analysis

The fundamental problem in Lidar is one of basic scattering physics, and many of the approaches used are borrowed from other types of scattering experiments. The most common Lidar design consists of a co-axial source and detector pair that measure the 180° backscatter as a function of distance along a straight path in an attenuating medium. Range resolution is obtained by emitting timed laser pulses. The Purple Crow Lidar, like many Lidars, is vertically-pointing and thus the path length is the same as the altitude, z.

The goal of Lidar analysis is the determination of the amount of backscattered light from each height and the degree to which the laser power is diminished along its path, thereby determining the optical characteristics of the atmosphere at each height. By further resolving these coefficients into components for each contributing process (most importantly – Rayleigh scattering, Mie scattering, Raman scattering, fluorescence and molecular absorption), the underlying physical theory behind each process can be evoked to relate these coefficients to more useful quantities (such as temperature, density and water vapour content).

The basic elastic single-scattering Lidar equation is parameterized in a fairly straightforward way in terms of backscattering and volume extinction coefficients β and α, respectively. These are the two key Lidar measurements, describing the amount of laser light reflected, and the amount of laser power attenuated per unit of volume.

Since each extinguishing volume along the path reduces the available laser power to subsequent volumes, the effect of attenuation must be integrated along the laser path: from the ground $z' = 0$ to the altitude under consideration, z. In practice, an additional range-dependent term must be introduced

due to the near field being out of focus, since the Lidar is focused at infinity. In terms of scattering, this effect can be explained in term of the incomplete overlap at lower altitudes between the laser beam scattering volume centered at z and the volume in the receiver's field of view.

Photodetectors measure the backscattered signal intensity over the area of the primary mirror in proportion to the total amount of light emitted by the scattering volume in all directions. These quantities are related through simple geometry by a ranging term, z^2. The strength of the measured signal, once the background counts are subtracted, due to a singly-scattering volume at height z for a vertically-pointing Lidar can be expressed as:

$$\mathbf{P}_{\lambda_0}(z) = K_{\lambda_0}\frac{O(z)}{z^2}\beta_{\lambda_0}(z)\exp\left(-2\int_0^z \alpha_{\lambda_0}(z')dz'\right) \tag{1.1}$$

where β and α are the backscatter and attenuation coefficients; K_{λ_0} is a range-independent system constant incorporating the source laser intensity, mirror size and detector efficiency at the measured wavelength; z^2 is the ranging term; and $O(z)$ represents the overlap function. The subscript λ_0 denotes the wavelength of the source laser.

In most practical Lidar systems, the system constant K_{λ_0} typically varies slowly with time, driven mostly by changes in the laser power (although it is effectively constant over the short time of a single laser shot). This system constant is usually normalized or divided out in most applications to account for these changes. The detector efficiency can also change rapidly over the time of a single laser shot from detector lag due to saturation, thereby having a range-dependent effect. This behaviour is mitigated through calibrated re-scaling of the received signal intensities in the saturation region (Sica et al., 1995). Most other sources of stray light, such as sky glow or the passing of a

star into the field of view, are constant over individual laser shots and therefore manifest themselves as a constant background count in the ranged data that is subtracted during processing.

The handling of the broad dynamic range of signal intensities, which increase exponentially with decreasing altitude, is a significant technical problem. As the PCL was designed for middle-upper atmosphere research, the detection system design was tailored towards this more sensitive detection region. A mechanical light chopper blocks light returns below an adjustable altitude, typically 33 km. Backscattered light at the laser wavelength is also split into separate detectors at a division of 95%/5% – the low-sensitivity channel is used to obtain useful measurements at altitudes where the high-sensitivity channel is near saturation.

For all of the unknown parameters in equation (1.1), there is but a single measured quantity – the signal power as a function of height. As physical theories are introduced and the number of parameters increases, reductive steps are necessary to obtain any useful values. The general approach to deriving quantities from Lidar measurements follows these steps:

1. Eliminate terms by either dividing sets of equations, normalizing terms, or restricting measurements to conditions where terms disappear

2. Incorporate external measurements, such as radiosondes, or models to reduce the number of remaining unknown terms

3. Retain a single remaining unknown term, to which changes in the measured laser power with altitude are attributed.

When making such measurements, particular care must be taken to ensure the continued validity of the models and assumptions used.

1.2 Basic Rayleigh and Raman Lidar scattering Equations

The PCL has a single laser source wavelength and three detection wavelengths. The laser wavelength, 532nm, was selected to minimize the backscatter and extinction contributions due to fluorescence and molecular absorption. It is also relatively easy to produce and operate consistently through freqency-doubling of a solid state Nd:YAG source. At this wavelength, backscatter and extinction are dominated by Rayleigh scattering, Mie-aerosol scattering and Ozone absorption, with a small residual contribution from all other sources:

$$\begin{aligned} \beta_{\lambda_0}(z) &= \beta_{\lambda_0}^{\text{ray}}(z) + \beta_{\lambda_0}^{\text{aer}}(z) + \Delta\beta_{\lambda_0}(z) \\ \alpha_{\lambda_0}(z) &= \alpha_{\lambda_0}^{\text{ray}}(z) + \alpha_{\lambda_0}^{\text{aer}}(z) + \alpha_{\lambda_0}^{O_3}(z) + \Delta\alpha_{\lambda_0}(z) \end{aligned} \tag{1.2}$$

Assuming this residual contribution to be negligible provides the **elastic Lidar scattering equation**:

$$\boxed{\begin{aligned} \mathbf{P}_{\lambda_0}(z) &= K_{\lambda_0}\frac{O(z)}{z^2}\left[\beta_{\lambda_0}^{\text{ray}}(z) + \beta_{\lambda_0}^{\text{aer}}(z)\right]\mathbf{T}_{\lambda_0}^2(z) \\ \mathbf{T}_{\lambda_0}(z) &= \mathrm{e}^{-\int_0^z\left[\alpha_{\lambda_0}^{\text{ray}}(z') + \alpha_{\lambda_0}^{\text{aer}}(z') + \alpha_{\lambda_0}^{O_3}(z')\right]dz'} \end{aligned}} \tag{1.3}$$

This equation represents the measured signal intensity (photocounts), $\mathbf{P}_{\lambda_0}(z)$, due to elastic Rayleigh and Mie-aerosol scattering at the wavelength of the source laser, λ_0. The transmission, $\mathbf{T}_{\lambda_0}(z)$, represents the fraction of light from a reference ground height ($z = 0$) that reaches the altitude z.

In addition to the elastic backscatter measurements at 532 nm, two additional photocounters were added to the Purple Crow Lidar in 2000 at 607 nm

and 660 nm (Argall et al., 2007). These wavelengths correspond to Raman-shifted vibrational emission lines of the source laser beam by N_2 and H_2O, respectively. This allows for the Lidar to measure abundances of these specific gases.

Since Raman scattering is produced strictly by a specific molecular transition, the presence of aerosols does not produce any additional backscatter in the measured Raman channel ($\beta^{\text{aer}}_{\lambda_R}(z) = 0$). All of the measured backscatter is assumed to be caused by Raman scattering of the target species.

It is important to note that the laser beam is extinguished at the laser wavelength along its upward path and then at the Raman wavelength as it returns downward along the same path. The cross-section for Raman scattering is many orders of magnitude less than for Rayleigh (Argall et al., 2007). However, the Raman-scattered light is still attenuated by Rayleigh scattering during the downward path at the shifted wavelength, λ_R. Under these conditions, equation (1.1) can be rewritten as (the **Raman Lidar scattering equation**):

$$\boxed{\begin{aligned} \mathbf{P}_{\lambda_R}(z) &= K_{\lambda_R}\frac{O(z)}{z^2}\beta^{\text{ram}}_{\lambda_R}(z)\mathbf{T}_{\lambda_0}(z)\mathbf{T}_{\lambda_R}(z) \\ \mathbf{T}_{\lambda_R}(z) &= \mathrm{e}^{-\int_0^z\left[\alpha^{\text{ray}}_{\lambda_R}(z')+\alpha^{\text{aer}}_{\lambda_R}(z')+\alpha^{O_3}_{\lambda_R}(z')\right]dz'} \end{aligned}} \tag{1.4}$$

In general, the amount of backscattered light β is equal to the number density of the target gas N times an effective backscatter target cross-section $\frac{\partial\sigma}{\partial\omega}(\pi)$.

$$\beta = \frac{\partial\sigma}{\partial\omega}(\pi)N \tag{1.5}$$

The elastic back-scattering of light due to the combined presence of atmospheric gases is described by Rayleigh-type scattering and is proportional to the total atmospheric number density, $N_{\text{total}}(z)$.

$$\beta_{\lambda_0}^{\text{ray}}(z) = \frac{\partial \sigma}{\partial \omega}^{\text{ray}}(\pi) N_{\text{total}}(z) \tag{1.6}$$

The N_2-Raman backscatter coefficient is similarly equal to the number density of molecular Nitrogen times the cross-sectional area. Further, since Nitrogen is well-mixed throughout the atmosphere, the number density of Nitrogen is proportional to the total molecular density of the atmosphere (Argall et al., 2007). The N_2-Raman atmospheric backscatter coefficient is, therefore, directly proportional to the total molecular atmospheric density:

$$\beta_{\lambda_{\text{N2}}}^{\text{ram}}(z) = K_1 N_{\text{total}}(z) \tag{1.7}$$

This results in the N_2-Raman and Rayleigh backscatter coefficients also being directly proportional.

$$\beta_{\lambda_0}^{\text{ray}}(z) = K_2 \beta_{\lambda_{\text{N2}}}^{\text{ram}}(z) \tag{1.8}$$

Equation 1.7 is substituted into equation 1.4 along with a modified system constant $K'_{\lambda_{\text{N2}}}$ to produce the **N_2-Raman Lidar scattering equation**:

$$\begin{aligned} \mathbf{P}_{\lambda_{\text{N2}}}(z) &= K'_{\lambda_{\text{N2}}} \frac{O(z)}{z^2} N_{\text{total}}(z) \mathbf{T}_{\lambda_0}(z) \mathbf{T}_{\lambda_{\text{N2}}}(z) \\ \mathbf{T}_{\lambda_{\text{N2}}}(z) &= e^{-\int_0^z \left[\alpha_{\lambda_{\text{N2}}}^{\text{ray}}(z') + \alpha_{\lambda_{\text{N2}}}^{\text{aer}}(z') + \alpha_{\lambda_{\text{N2}}}^{O_3}(z') \right] dz'} \end{aligned} \tag{1.9}$$

It is useful to note that the transmission profile due to each individual extinction component can be separated as:

$$\mathbf{T}(z) = e^{-\int_0^z \left[\alpha^{\text{ray}}(z') + \alpha^{\text{aer}}(z') + \alpha^{O_3}(z')\right] dz'}$$

$$\mathbf{T}(z) = e^{-\int_0^z \alpha^{\text{ray}}(z')dz'} \; e^{-\int_0^z \alpha^{\text{aer}}(z')dz'} \; e^{-\int_0^z \alpha^{O_3}(z')dz'}$$

$$\mathbf{T}(z) = \mathbf{T}^{\text{ray}}(z)\, \mathbf{T}^{\text{aer}}(z)\, \mathbf{T}^{O_3}(z) \tag{1.10}$$

1.3 Aerosol Lidar Measurements

Lidar systems are, by their nature, well disposed for measuring the optical properties of atmospheric aerosols. Aerosol backscatter is readily measured by simple elastic Rayleigh systems. Extinction measurements have historically been derived from backscatter data by the use of inversion techniques (Klett, 1981), which require a priori assumptions about the aerosols under observation.

It is possible, using a Rayleigh Lidar, to measure the total amount of extinction (optical depth) of aerosol features by determining the clean-air signal above and below the feature, and thereby assign a mean ratio of the total backscatter to the total extinction, however this completely masks any structure within the feature, including possible changes of phase or composition (smoke mixed with water and ice, for instance).

The incorporation of Raman measurements allows for direct, independent measurement of aerosol extinction without such assumptions or limitations (Ansmann et al., 1990).

1.4 Aerosol Backscatter

A useful quantity closely related to the aerosol backscatter coefficient is the aerosol scattering ratio (**ASR**). This quantity represents the total combined backscatter due to Rayleigh and aerosol scattering relative to the backscatter due to Rayleigh scattering alone, and is defined as:

$$R \equiv \frac{\beta_{\lambda_0}^{\text{ray}}(z) + \beta_{\lambda_0}^{\text{aer}}(z)}{\beta_{\lambda_0}^{\text{ray}}(z)} \tag{1.11}$$

This quantity can be readily calculated, as the numerator term appears directly in the Rayleigh Lidar scattering equation (1.3), and the denominator is directly proportional to the total atmospheric molecular density (1.6) and thus can be deduced from N_2-Raman Lidar (1.8), radiosonde data, or any other a priori density measurement.

Dividing the Rayleigh Lidar scattering equation (1.3) by Raman Lidar equation (1.4) for N_2 produces:

$$\frac{\mathbf{P}_{\lambda_0}(z)}{\mathbf{P}_{\lambda_{\text{N2}}}(z)} = \frac{K_{\lambda_0}\frac{O(z)}{z^2}\left[\beta_{\lambda_0}^{\text{ray}}(z) + \beta_{\lambda_0}^{\text{aer}}(z)\right]\mathbf{T}_{\lambda_0}^2(z)}{K_{\lambda_{\text{N2}}}\frac{O(z)}{z^2}\beta_{\lambda_{\text{N2}}}^{\text{ram}}(z)\mathbf{T}_{\lambda_0}(z)\mathbf{T}_{\lambda_{\text{N2}}}(z)} \tag{1.12}$$

This simplifies to:

$$\frac{\mathbf{P}_{\lambda_0}(z)}{\mathbf{P}_{\lambda_{\text{N2}}}(z)} = \frac{K_{\lambda_0}}{K_{\lambda_{\text{N2}}}}\frac{\left[\beta_{\lambda_0}^{\text{ray}}(z) + \beta_{\lambda_0}^{\text{aer}}(z)\right]}{\beta_{\lambda_{\text{N2}}}^{\text{ram}}(z)}\frac{\mathbf{T}_{\lambda_0}(z)}{\mathbf{T}_{\lambda_{\text{N2}}}(z)} \tag{1.13}$$

and can be reorganized into the form:

$$\frac{\beta_{\lambda_0}^{\text{ray}}(z) + \beta_{\lambda_0}^{\text{aer}}(z)}{\beta_{\lambda_{\text{N2}}}^{\text{ram}}(z)} = \frac{K_{\lambda_{\text{N2}}}}{K_{\lambda_0}}\frac{\mathbf{P}_{\lambda_0}(z)}{\mathbf{P}_{\lambda_{\text{N2}}}(z)}\frac{\mathbf{T}_{\lambda_{\text{N2}}}(z)}{\mathbf{T}_{\lambda_0}(z)} \tag{1.14}$$

This equation can be substituted into the aerosol scattering ratio equation (1.11) by making use of the proportionality of the Raman and Rayleigh

backscatter (1.8):

$$R(z) = K_2 \frac{K_{\lambda_{N2}}}{K_{\lambda_0}} \frac{\mathbf{P}_{\lambda_0}(z)}{\mathbf{P}_{\lambda_{N2}}(z)} \frac{\mathbf{T}_{\lambda_{N2}}(z)}{\mathbf{T}_{\lambda_0}(z)} \tag{1.15}$$

Since $R(z)$ is defined such that it is equal to one within some region z_0 of negligible aerosol backscatter (clear sky altitude), it is possible to further simplify this expression through normalization:

$$\begin{aligned} R(z) &= K_2 \frac{K_{\lambda_{N2}}}{K_{\lambda_0}} \frac{\mathbf{P}_{\lambda_0}(z)}{\mathbf{P}_{\lambda_{N2}}(z)} \frac{\mathbf{T}_{\lambda_{N2}}(z)}{\mathbf{T}_{\lambda_0}(z)} / R_0 \\ R_0 &= K_2 \frac{K_{\lambda_{N2}}}{K_{\lambda_0}} \frac{\mathbf{P}_{\lambda_0}(z_0)}{\mathbf{P}_{\lambda_{N2}}(z_0)} \frac{\mathbf{T}_{\lambda_{N2}}(z_0)}{\mathbf{T}_{\lambda_0}(z_0)} \end{aligned} \tag{1.16}$$

This reduces to the useful expression for the aerosol scattering ratio:

$$\boxed{\begin{aligned} R'(z) &= \frac{\mathbf{P}_{\lambda_0}(z)}{\mathbf{P}_{\lambda_{N2}}(z)} \frac{\mathbf{T}_{\lambda_{N2}}(z)}{\mathbf{T}_{\lambda_0}(z)} \\ R(z) &= \frac{R'(z)}{R'(z_0)} \end{aligned}} \tag{1.17}$$

The aerosol scattering ratio is simply the ratio of the Rayleigh to N_2-Raman counts multiplied by the inverse ratio of the transmissions. Since the wavelengths of the two channels are close, the corresponding ratios will be close as well. As a zeroth-order approximation, the transmission term can be dropped and the aerosol scattering ratio taken to be simply the normalized ratio of the photocounts in the Rayleigh and N_2-Raman channels.

As an improved first-order approximation, static transmission profiles can be calculated from a model atmosphere. The accuracy of this approach is dictated by how closely the actual conditions resemble those assumed by the

model for all altitudes between the height under consideration and the normalization altitude (due to the integrated nature of transmission profiles). Generally this means that they must be free of significant aerosols – the main source of significant attenuation changes. Since aerosol attenuation is stronger for shorter wavelengths it has a greater effect on decreasing the transmission at the Rayleigh wavelength than N_2-Raman (increasing the value of $\mathbf{T}_{\lambda_{N2}}(z)/\mathbf{T}_{\lambda_0}(z)$).

For instance, if the ASR is normalized to one at a low altitude, an aerosol layer at higher altitude would cause an increase in the ratio of transmissions for all altitudes above the aerosol layer. This would be measured as a decrease in the ratio of Rayleigh to N_2-Raman photocounts, $\mathbf{P}_{\lambda_0}(z)/\mathbf{P}_{\lambda_{N2}}(z)$. If this aerosol layer were not included in the transmission profile used, this would result in the ASR being calculated as lower than the true value. This would also occur within a vertically-extended aerosol layer, such as a cumulus cloud – the measured ASR would be lower toward the upper portion of the cloud.

The result is that aerosol layers that are not accounted for in the transmission profiles cause $R(z)$ to be measured to be lower than the true value for all altitudes above a layer situated above the normalization altitude. Conversely, aerosol layers cause all altitudes below the normalization to measure a value of $R(z)$ greater than the true value.

Once $R(z)$ is determined, the backscatter coefficient can be obtained from (1.11) in concert with a model or radiosonde density profile to obtain $\beta^{\text{ray}}_{\lambda_0}(z)$:

$$\boxed{\beta^{\text{aer}}_{\lambda_0}(z) = \beta^{\text{ray}}_{\lambda_0}(z)(R(z) - 1)} \tag{1.18}$$

1.5 Aerosol Extinction

The basic method for measuring aerosol extinction by way of Raman Lidar described by Ansmann et al. (1990) is fairly straight-forward. It is derived by first re-arranging the terms of the N_2-Raman Lidar scattering equation (1.8):

$$\frac{z^2\mathbf{P}_{\lambda_{N2}}(z)}{K'_{\lambda_{N2}}O(z)N_{\text{total}}(z)} = e^{-\int_0^z \left[\alpha^{\text{ray}}_{\lambda_{N2}}(z') + \alpha^{\text{aer}}_{\lambda_{N2}}(z') + \alpha^{O_3}_{\lambda_{N2}}(z') + \alpha^{\text{ray}}_{\lambda_0}(z') + \alpha^{\text{aer}}_{\lambda_0}(z') + \alpha^{O_3}_{\lambda_0}(z')\right]dz'} \tag{1.19}$$

and then taking the derivative of the logarithm:

$$\frac{d}{dz}\left[\ln\frac{O(z)N_{\text{total}}(z)}{z^2\mathbf{P}_{\lambda_{N2}}(z)}\right] = \alpha^{\text{ray}}_{\lambda_{N2}}(z) + \alpha^{\text{aer}}_{\lambda_{N2}}(z) + \alpha^{O_3}_{\lambda_{N2}}(z) + \alpha^{\text{ray}}_{\lambda_0}(z) + \alpha^{\text{aer}}_{\lambda_0}(z) + \alpha^{O_3}_{\lambda_0}(z) \tag{1.20}$$

A relationship is assumed for the wavelength-dependence of the extinction coefficient of the form:

$$\frac{\alpha^{\text{aer}}_{\lambda_0}(z)}{\alpha^{\text{aer}}_{\lambda_{N2}}(z)} = \left(\frac{\lambda_{\lambda_{N2}}}{\lambda_{\lambda_0}}\right)^k \tag{1.21}$$

This allows (1.20) to be expressed in the useful form:

$$\boxed{\alpha^{\text{aer}}_{\lambda_0}(z) = \frac{\frac{d}{dz}\left[\ln\frac{O(z)N_{\text{total}}(z)}{z^2\mathbf{P}_{\lambda_{N2}}(z)}\right] - \alpha_i}{1+\left(\frac{\lambda_{\lambda_0}}{\lambda_{\lambda_{N2}}}\right)^k}} \qquad \boxed{\alpha_i = \alpha^{\text{ray}}_{\lambda_0}(z) - \alpha^{O_3}_{\lambda_0}(z) - \alpha^{\text{ray}}_{\lambda_{N2}}(z) - \alpha^{O_3}_{\lambda_{N2}}(z)} \tag{1.22}$$

This equation can be equivalently expressed as (Ansmann et al., 1990):

$$\alpha_{\lambda_0}^{\text{aer}}(z) = \frac{\left[\frac{O'(z)}{O(z)} + \frac{N'_{\text{total}}(z)}{N_{\text{total}}(z)} - \frac{2}{z} - \frac{\mathbf{P}'_{\lambda_{N2}}(z)}{\mathbf{P}_{\lambda_{N2}}(z)}\right] - \alpha_i}{1 + \left(\frac{\lambda_{\lambda_0}}{\lambda_{\lambda_{N2}}}\right)^k} \tag{1.23}$$

The main advantage to this formulation is that it is not dependent on any range-integrated quantities and is therefore not prone to accumulated error as the backscatter. This formulation, however, requires knowledge of the geometrical overlap term, $O(z)$, which must be measured. The atmospheric density, $N_{\text{total}}(z)$, as well as the Rayleigh and Ozone extinction coefficients can be determined from a model atmosphere, radiosonde-ozonesonde, or other means. A value for the coefficient k must be assumed, and can safely be taken to be one for the wavelengths used (Ansmann et al., 1990).

1.6 Aerosol Extinction-to-Backscatter Ratio

The aerosol extinction-to-backscatter ratio, γ, is a very useful quantity in characterizing aerosol targets (Ferrare et al., 2001). It relates the amount of absorption and anisotropic scattering at angles less than 180° to the relative amount of backscatter. Rayleigh-only type Lidar systems using inversion techniques for aerosol measurement typically make model-based assumptions of the value γ in order to calculate extinction coefficients from the backscatter data. For this reason, the extinction-to-backscatter ratio is traditionally referred to as the **Lidar ratio** in literature. The PCL, however, has the capability to measure this quantity directly from independent measurement of the extinction and backscatter:

$$\gamma = \frac{\alpha_{\lambda_0}^{\text{aer}}}{\beta_{\lambda_0}^{\text{aer}}} \tag{1.24}$$

The orbiting space-based Calipso Rayleigh Lidar does not have a Raman channel. It uses an iterative approach to identifying aerosol types (based on polarization, backscatter ratio at 532 and 1064 nm, total optical depth and other measures) and most often assigns an extinction-to-backscatter ratio based on the determined type (Winker, 2008). The aerosol extinction profiles are calculated based on the backscatter data from the assumed particle type. Its reference values for the extinction to backscatter ratio are listed in Table 1.1 and provide a useful guide for identifying aerosol types based on the measured Lidar ratio.

Material	**Ratio**
Water Cloud	18 sr
Ice Cloud	25 sr
Marine Aerosol	20 sr
Desert Dust	40 sr
Polluted Continental	70 sr
Clean Continental	35 sr
Polluted Dust	65 sr
Biomass Burning	70 sr

Table 1.1: Calipso extinction-to-backscatter ratio reference values

1.7 Outline

Determination of the aerosol backscatter (1.18) and extinction (1.23) (and corresponding Lidar ratio) requires knowledge of the Lidar-measured photocount profiles $\mathbf{P}$, overlap function $O(z)$, atmospheric transmission $\mathbf{T}$, Rayleigh and ozone extinction coefficients α_i, Rayleigh backscatter coefficients $\beta_{\lambda_0}^{\text{ray}}(z)$ as

well as the atmospheric density $N_{\text{total}}(z)$.

The atmospheric transmission (and corresponding extinction) profiles are typically obtained from models. A common approach is to use a single static profile for all measurements. This approach is refined by using quarterly profiles, calculated from radiosonde / ozonesonde flights. The error with these approaches due to night-to-night variability is discussed in Section 2.

The overlap function is specific to the design of the PCL. A method to measure its behaviour developed by Wandinger and Ansmann (2002) is employed in Section 3, and its variability is discussed.

One of the biggest obstacles to obtaining aerosol measurements with the Purple Crow has been the design of the Mie-Rayleigh detection channel, which incorporates a mechanical chopper that blocks most (but not all) of the signal returns below 30 km. A novel method was developed to correct for this effect, which is detailed in Section 4.

Atmospheric density is obtained from daily radiosonde flights from Detroit. These are assumed to be a better approximation to the actual conditions at the PCL site than a generic model. An attempt is made to quantify the error due to this assumption in the aerosol extinction coefficient by examining the extinction values for several "aerosol-free" nights in Section 5.

Finally, aerosol measurements are presented for a number of nights in Section 5, including observations of high-altitude smoke.

Chapter 2

Lidar Signal Attenuation

Most Lidar applications in the troposphere and stratosphere are significantly affected by signal attenuation – mostly by Rayleigh scattering, ozone absorption and aerosol scattering and absorption. As direct extinction measurements are typically not available during routine Lidar data collection, it is necessary to obtain values from models.

It is fairly common in Lidar calculations to use a static annual model. To improve upon this static transmission model, a quarterly seasonal model is derived from in-situ balloon-borne radiosonde/ozonesonde measurements. These measurements are also used to determine the variability in atmospheric density and ozone concentrations. This variability is used to characterize the systematic error caused by differences in the actual atmospheric conditions and those assumed by the seasonal model.

Measurements from 169 radiosonde/ozonesonde flights between 2003 and 2009 from Egbert, Ontario (44.23° N, −79.78° E) are used (Meteorological Service of Canada, 2008). These are routine measurements performed on a weekly basis, usually at around 11:00 or 17:00 UT. The atmospheric density

and ozone concentration profiles are grouped by quarter – January-March (Q1, winter), April-June (Q2, spring), July-September (Q3, Summer), October-December (Q4, fall). The first and fourth quarters are sampled fairly evenly while the second quarter contains more profiles in colder months, April and May, and the third quarter have a small sampling bias towards warmer months, July and August (Figure 2.1).

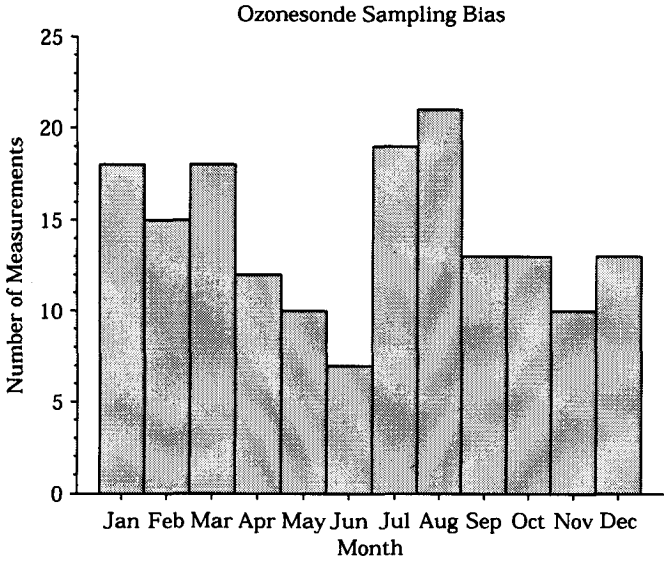

Figure 2.1: Distribution of profiles used for quarterly averages.

2.1 Rayleigh Scattering Extinction

The effect of Rayleigh extinction is equal to the total amount of light scattered by Rayleigh scattering. The total Rayleigh target cross-section defines the relationship between the total atmospheric density and the Rayleigh extinction coefficient at a given wavelength.

$$\alpha_{\lambda}^{\text{ray}}(z) = \sigma_{\lambda}^{\text{ray}} N_{\text{Total}}(z) \tag{2.1}$$

The total Rayleigh cross-section is $\sigma_{\lambda_0}^{ray} = 5.1680 \times 10^{-31}$ m^2 at 532 nm and $\sigma_{\lambda_{N2}}^{ray} = 3.0175 \times 10^{-31}$ m^2 at 607 nm (Bucholtz, 1995). All that is needed to calculate a Rayleigh extinction profile is a density profile.

The US1976 model atmosphere (US Standard Atmosphere, 1976) consists of a single annually-averaged profile suitable for mid-latitudes and is a useful reference for comparison (Figure 2.2).

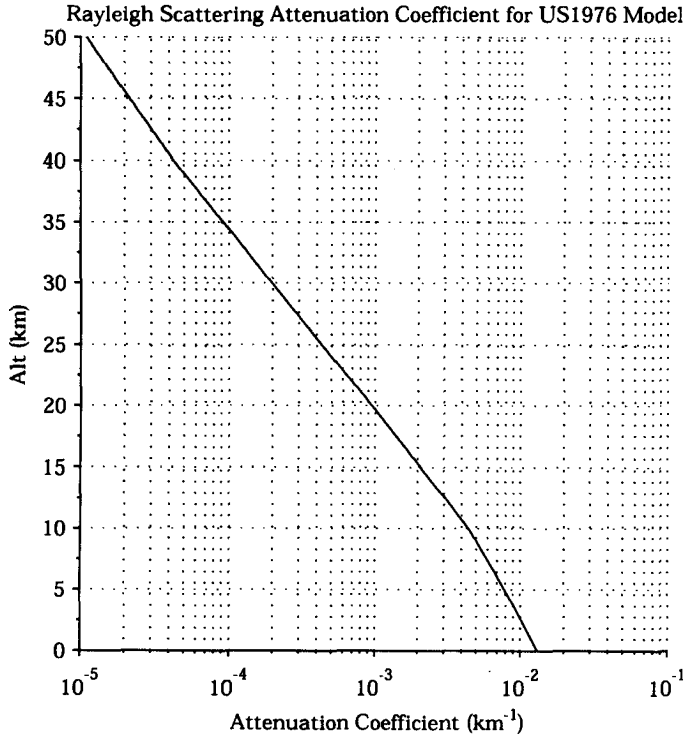

Figure 2.2: Standard model atmosphere US1976 extinction coefficient profile at 532 nm.

Density profiles are also obtained from radiosonde measurements and converted into Rayleigh scattering extinction profiles. The average of all extinction profiles for each quarter is calculated to obtain a seasonal model (Figure 2.3).

The quarterly Rayleigh extinction profiles remain within 10% of the US1976

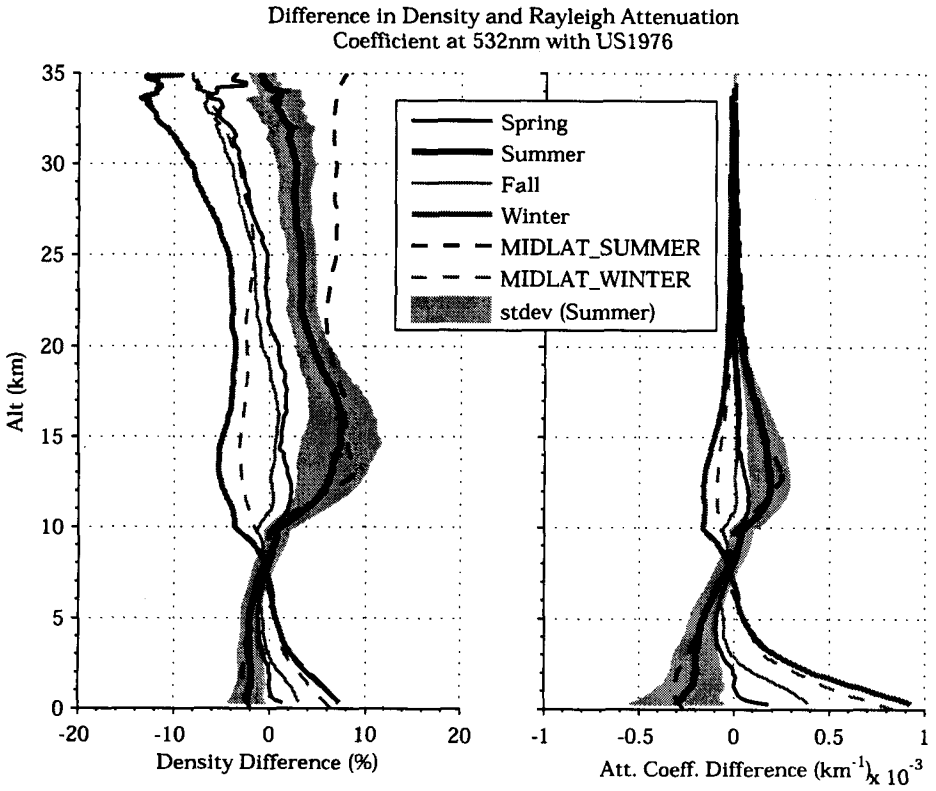

Figure 2.3: Average quarterly Rayleigh scattering extinction coefficient profiles. The absolute and relative differences from the US1976 model atmosphere are shown. MIDLAT-SUMMER and MIDLAT-WINTER model atmosphere profiles shown for comparison (Kantor and Cole, 1962). The standard deviation of all profiles in the Summer quarter is also indicated, to quantify the range of variability expected for a single observation relative to the average.

model for all altitudes and seasons. The relative difference gets larger toward higher altitudes, but the magnitude generally decreases with altitude (except for near the tropopause).

In spring and summer the Rayleigh extinction is lower in the troposphere and higher in the stratosphere compared to the annual model. In fall and winter the reverse is true. The differences are greatest in summer and winter.

The summer profile, for instance, is 3×10^{-4} km^{-1} lower than US1976 at the ground, nearly equal around 8 km, and 2×10^{-4} km^{-1} higher at 12 km – decreasing toward zero at higher altitudes. The seasonal Rayleigh extinction coefficient offers minor improvements over the annual model when used in the measurement of faint aerosol extinction at low altitudes Figure 2.3.

The standard deviation of the summer profiles relative to the seasonal average is 3×10^{-4} km^{-1} at the ground and 2×10^{-4} km^{-1} at 15 km. As a result, the error in the derived aerosol extinction due to variability in the Rayleigh component of the measured total extinction profile will be negligeable when when a quarterly density model is assumed. This error is further reduced if semi-concurrent radiosonde density measurements are used to obtain the Rayleigh scattering extinction coefficient.

Variations in the relative density, which can be $\pm$ 10% relative to US1976 (Figure 2.3), will cause corresponding errors in measurements that are directly proportional to the total atmospheric density such as the molecular backscatter (1.5) and aerosol backscatter (1.18). Seasonal fluctuations produce an average deviation across all altitudes of about 5% relative to the annual model.

From the standard deviation of the summer profiles, there is a further 5-10% variability on a given night relative to the quarterly average. This 5-10% night-to-night error should be expected even when semi-concurrent density profiles from nearby radiosonde are used since regional climate differences may

be just as high. A measurement of ground pressure / temperature conditions would be adequate to reduce this error.

2.1.1 Transmission

The transmission of the atmosphere only plays a small role in aerosol measurements. The term does not factor directly into the aerosol extinction calculation (1.23) and appears only as a ratio of the transmissions at 532 nm and 607 nm (1.15). Since the latter will tend to be fairly close to one, only significant deviations from the assumed transmission functions will result in noticeable error in the aerosol backscatter. For the sake of other Lidar measurements, notably density and temperature retrievals, it is useful to characterize the variability in Rayleigh transmission. The quarterly transmission profiles can also be used as improved seasonal models over the annual US1976 model. The Rayleigh transmission profile for US1976 as well as each of the individual radiosonde measurements is calculated from the extinction coefficients:

$$\mathbf{T}_{\lambda}^{\text{ray}}(z) = \exp\left(-\int_0^z \alpha_{\lambda}^{\text{ray}}(z')dz'\right) \tag{2.2}$$

From the resulting transmission profiles (Figure 2.4) it is obvious that the atmospheric transmission due to Rayleigh scattering varies very little. This result is to be expected, given the stable structure of the Earth's atmosphere, and that the transmission functions are normalized at the ground. Most of the variations in density manifest throughout the vertical column. Thus, while the total column atmospheric mass and corresponding optical depth may fluctuate on the order of 5-10% (Figure 2.3), the relative transmission normalized to the ground is stable.

In winter, the mean fractional difference in the seasonal profile at 532 nm

from the annual model across all altitudes is $-0.084 \pm 0.003\%$, with a maximum difference of -0.2%. In summer the mean difference is $+0.025 \pm 0.003\%$ with a maximum difference of $+0.13\%$. The standard deviation of the profiles relative to the seasonal mean is consistently less than 0.2% at all altitudes. The use of an annual model produces very little systematic error in the transmission due to Rayleigh scattering.

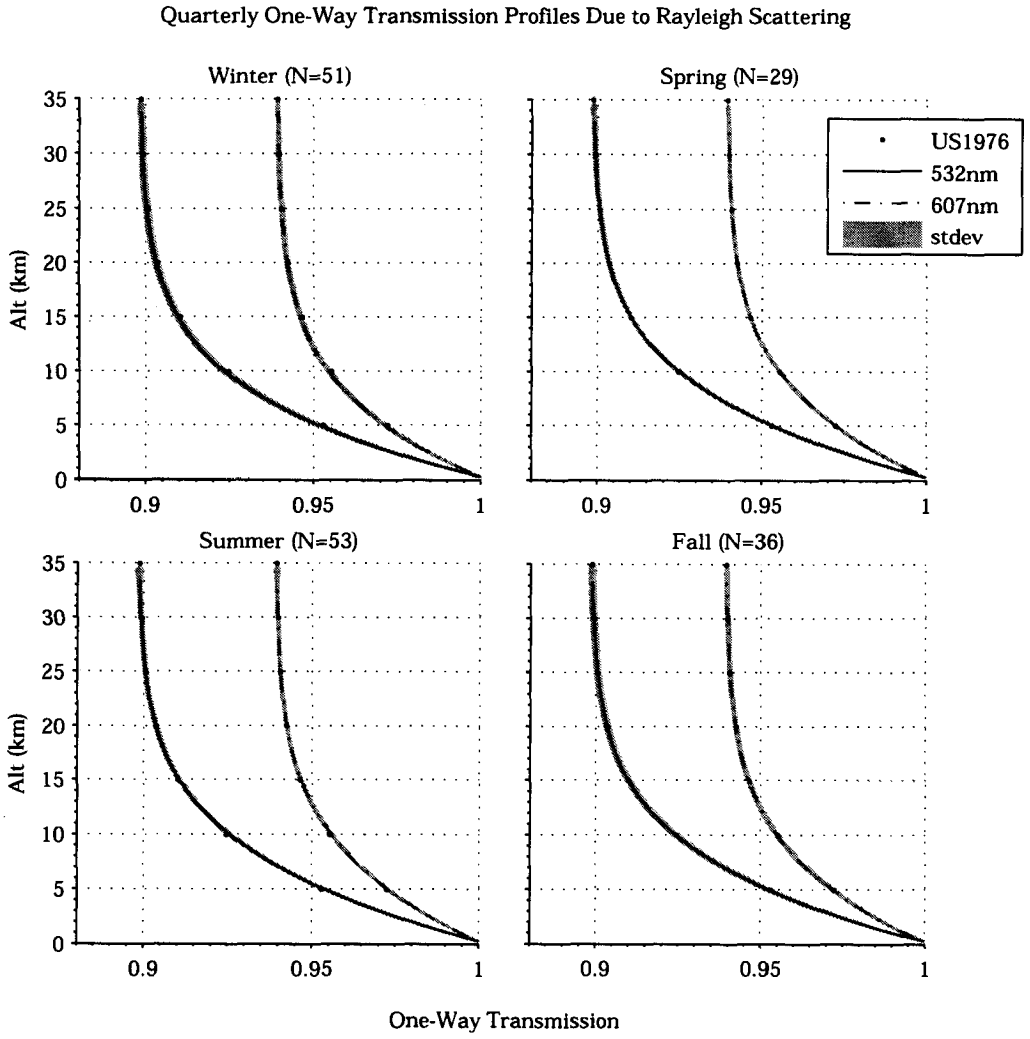

Figure 2.4: One-way Rayleigh scattering transmission normalized to 300 m. The difference with US1976 is extremely small.

In order to measure the effect of this assumption on measured quantities, such as density / temperature, it is instructive to look at the two-way transmission profile (Figure 2.5); this is the term that appears in the basic Lidar equations (1.3) and (1.4). This represents the decrease in signal power due to attenuation by Rayleigh scattering along both the upward and downward path of the beam. For the elastic Rayleigh signal and N_2-Raman signal, the two-way transmission is equal to:

$$\begin{aligned} \mathbf{T}^2_{\text{ray},\lambda_0} &= \mathbf{T}^{\text{ray}}_{\lambda_0}(z)\mathbf{T}^{\text{ray}}_{\lambda_0}(z) \\ \mathbf{T}^2_{\text{ray},\lambda_{N2}} &= \mathbf{T}^{\text{ray}}_{\lambda_0}(z)\mathbf{T}^{\text{ray}}_{\lambda_{N2}}(z) \end{aligned} \tag{2.3}$$

Many physical parameters, such as temperature, are prone to less variability at higher altitudes and can, therefore, be determined more accurately from models. For this reason many Lidar analysis schemes use an approach of downward integration of values and thus it is useful to normalize the two-way transmission functions at a high altitude, where attenuation is negligible (50 km).

The two-way Rayleigh transmission function at 10 km for 532 nm/532 nm is 6% higher than at 30 km. If no correction for Rayleigh transmission were made at all ($\mathbf{T}^2_{\text{ray},\lambda_0} = 1$), this would result in density measurements using the basic Lidar equation (1.3) at 10 km to be 6% above the proper value when the correction is made. This is clearly erroneous.

There is only a small difference between the use of seasonal and annual models. The peak difference in the average quarterly profile (occurring at 8 km) relative to US1976 (Figure 2.6) is -0.35%, while for summer the peak error is $+0.25\%$. This is a small error for most applications, but may be significant for climatology studies.

The peak variability of individual nights relative to the quarterly average is 0.30% in winter and 0.15% in summer.

The magnitude and variability of the two-way transmission for the N_2-Raman channel (signal traveling upward at 532 nm and returning downward 607 nm) are less due to the diminished effect of Rayleigh attenuation at the longer wavelength of 607 nm (Figures A.1 and A.2).

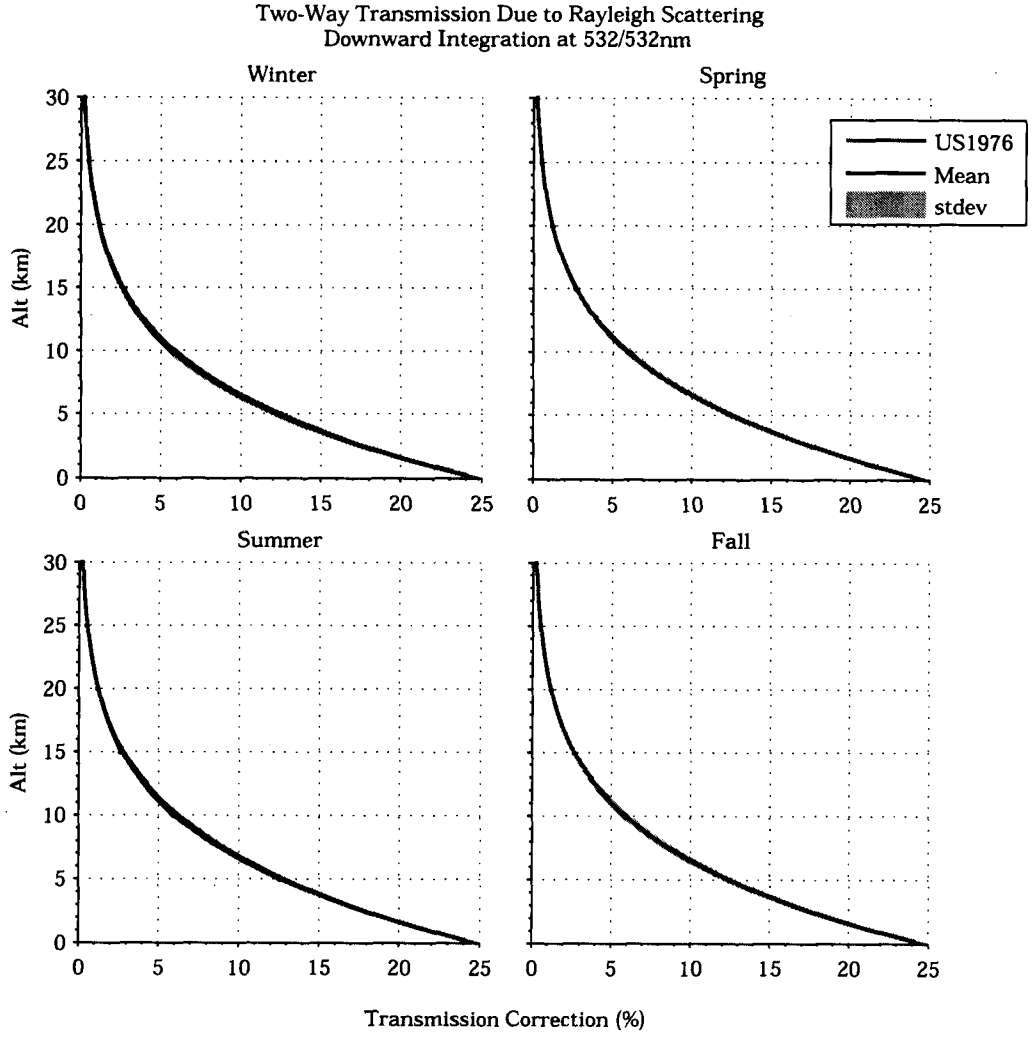

Figure 2.5: Two-way transmission profiles due to Rayleigh scattering at 532/532 nm. The profiles are normalized to 50 km and expressed as a relative percentage above 100%.

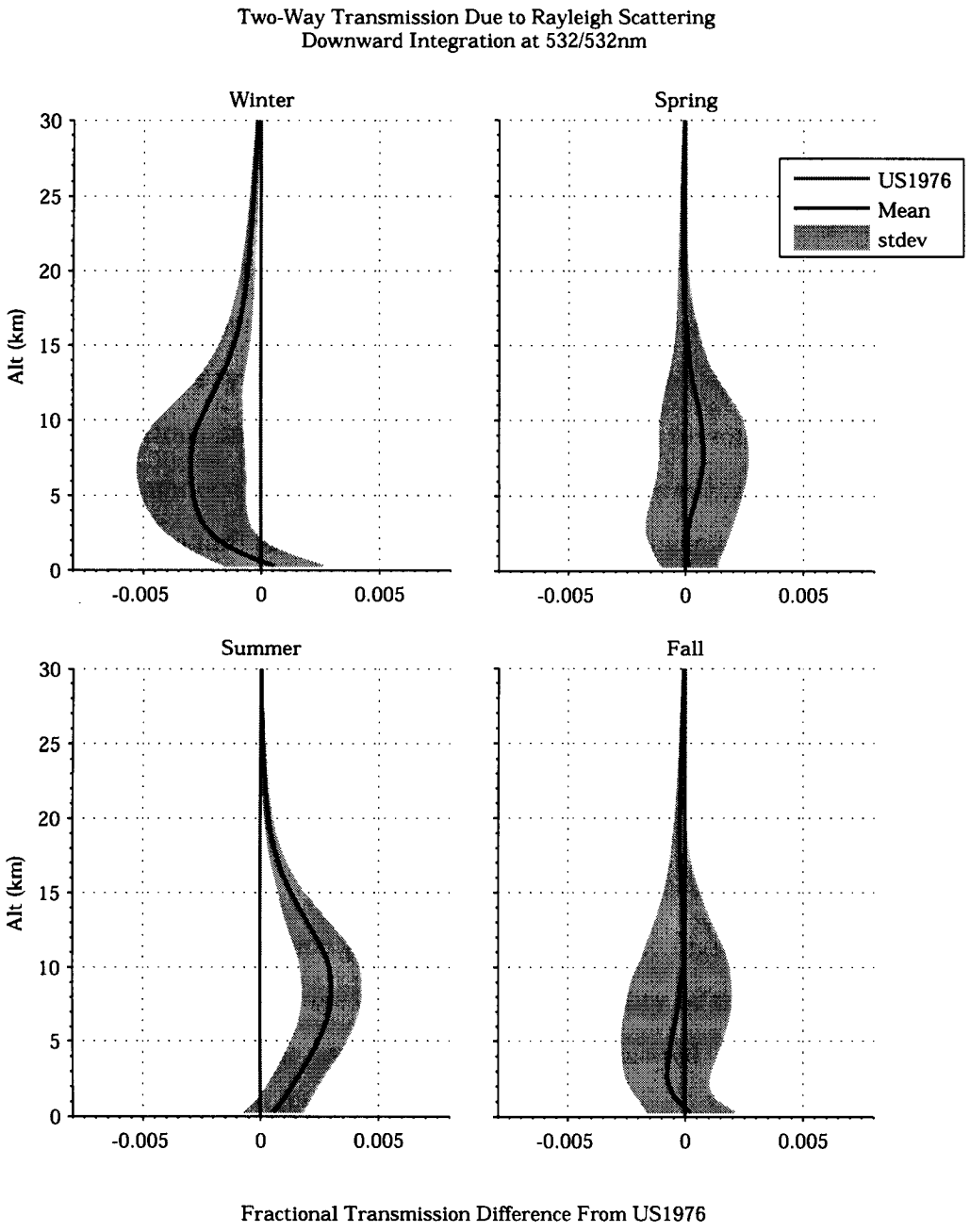

Figure 2.6: Two-way transmission profiles due to Rayleigh scattering at 532/532 nm expressed relative to US1976.

2.2 Ozone Extinction

The PCL source wavelength (532 nm) as well as the measured H_2O and N_2 Raman-shifted wavelengths (660.3 and 607.3 nm) all lie within the Chapuis band of ozone absorption, making ozone the most important gaseous species for non-Rayleigh signal extinction (Sica et al., 2001). The effects of ozone extinction are important from 0 to 45 km altitude and highly variable. They can seldom be ignored without introducing significant error. Detailed ozone measurements are typically unavailable for routine Lidar operations, requiring the use of various assumptions and models. For this reason it is particularly important to understand the potential error that these assumptions introduce.

The US Standard Atmosphere of 1976 includes a single annually-averaged ozone profile (the annual model) (Krueger and Minzner, 1976) representative of concentrations across the continental United States (Figure 2.7). Extinction coefficients are calculated as the molecular ozone density times the effective absorption cross section:

$$\alpha_\lambda^{O_3}(z) = \sigma_\lambda^{O_3}(z) N_{O_3}(z) \tag{2.4}$$

The ozone concentration profiles from ozonesonde flights (Section 2.1) are used to calculate the average as well as the variability of the ozone extinction profiles by quarter. The average of the four measured quarterly profiles is fairly close to the annual model profile (Figure 2.7).

Ozone cross-sections are obtained from Bogumil et al. (2003):

$$\sigma_{532}^{O_3} = 2.2 \times 10^{-25} \text{ m}^{-1} \text{ molecule}^{-1}$$
$$\sigma_{607}^{O_3} = 5.2 \times 10^{-25} \text{ m}^{-1} \text{ molecule}^{-1}$$

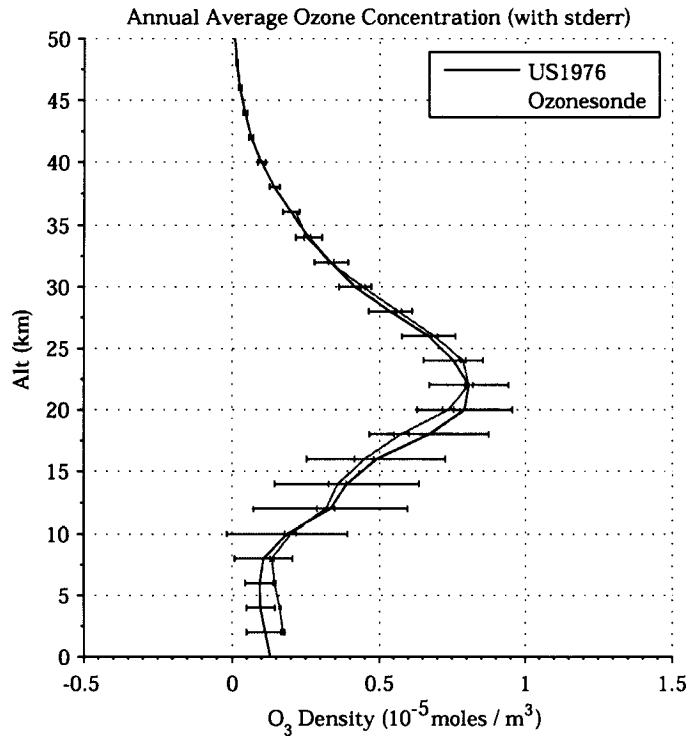

Figure 2.7: US1976 model and ozonesonde average ozone profile. The standard deviation of the model and standard error of the ozonesonde average are shown.

The average quarterly attenuation coefficient profiles (seasonal model) are shown along with the night-to-night variability, calculated as the standard deviation of the profiles (Figure 2.8). It is important to point out that this description assumes a Gaussuan distribution of measurements; however, in practice the distribution is highly variable and slightly skewed toward positive values, in part due to truncation at zero concentration. As a result, slightly more observations at higher concentrations are to be expected than is suggested.

Peak ozone attenuation occurs at 22 km with an annually-averaged magnitude of 1×10^{-3} km^{-1} at 532 nm (Figure 2.8). Due to a higher cross-section, attenuation at 607 nm is 2.4 times stronger than at 532 nm (Figure A.3). At

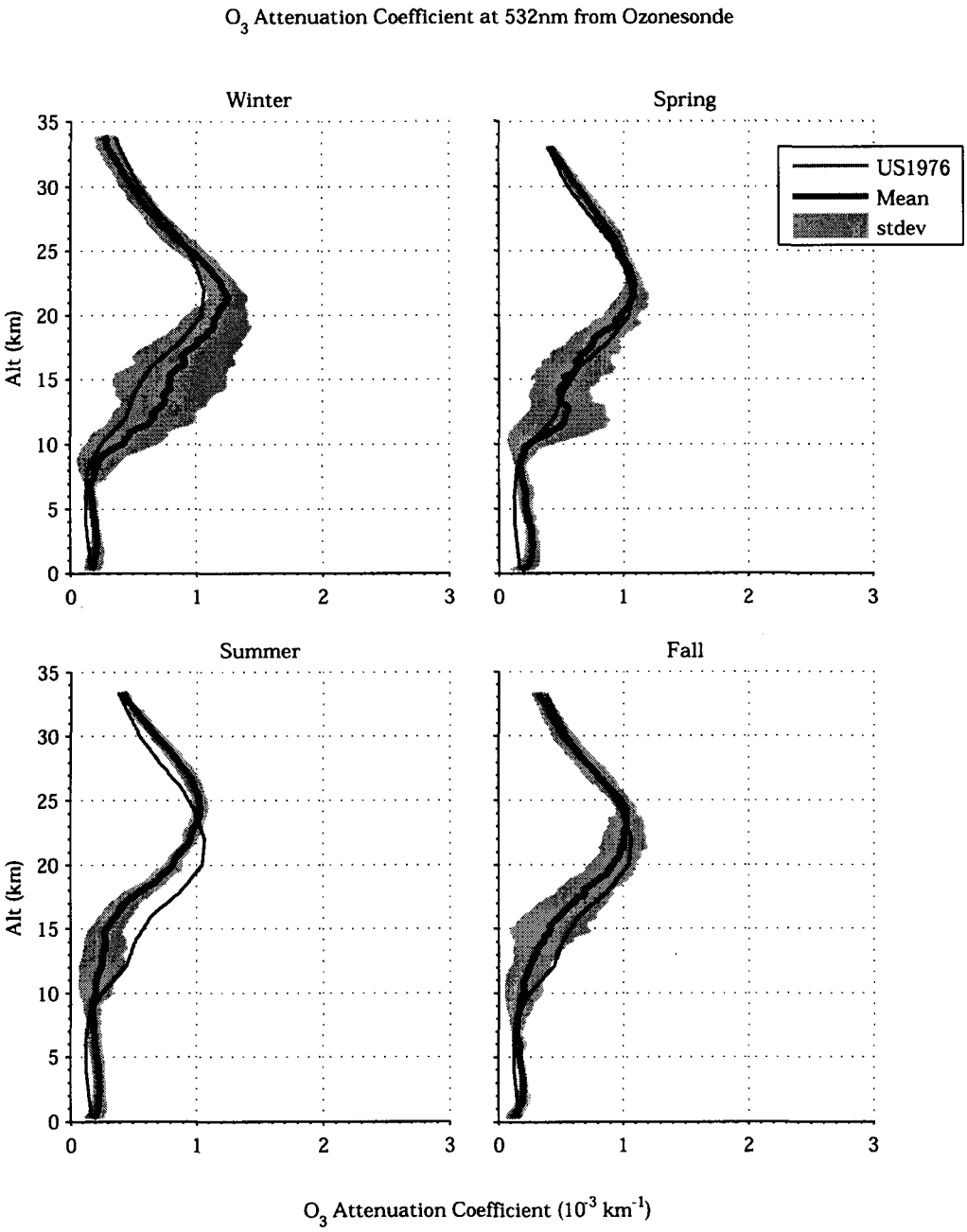

Figure 2.8: Quarterly ozone extinction coefficient profiles calculated at 532 nm using ozonesonde profiles. The standard deviation of the profiles is also shown.

15 km, the average attenuation at 532 nm is 0.6×10^{-3} km^{-1}. Below 8 km, the quarterly ozone measurements are all consistently higher than the US1976 model – likely due to strong local influences. Most of the variability in ozone occurs between 8 and 22 km. In this region, attenuation is stronger than US1976 in the Winter, nearly equal in Spring, and weaker in the Summer and Fall. The peak difference tends to occur near 15 km.

In Winter the maximum difference in the quarterly averages relative to US1976 is $+0.2 \times 10^{-3}$ km^{-1} while in Summer the maximum difference is -0.3×10^{-3} km^{-1} (Figure 2.9).

Expected differences for a single measurement relative to the quarterly average are also significant, due to high day-to-day variability. At 15 km, the standard deviation of the profiles is 0.5×10^{-3} km^{-1} in Winter and 0.2×10^{-3} km^{-1} in Summer.

The calculation of the aerosol extinction coefficient (1.22) is dependent on the sum of the ozone extinction coefficient at 532 and 607 nm. Since ozone attenuation at 607 nm is 2.4 times that at 532 nm (Figure A.3, A.4), the systematic error in the measured aerosol extinction coefficient associated with using the quarterly profiles instead of concurrent ozone measurements on a given night is typically $1 + 2.4 = 3.4$ times the standard deviation represented in Figure 2.9. At 15 km this is 1.7×10^{-3} km^{-1} in Winter and 0.68×10^{-3} km^{-1} in Summer.

The systematic error in the aerosol extinction coefficient due to the use of the seasonal model instead of concurrent ozone measurements is significant (error $> 5\%$) for aerosol extinction values less than 3.4×10^{-2} km^{-1} at 15 km. If an annually-averaged model is used instead, the threshold is even higher.

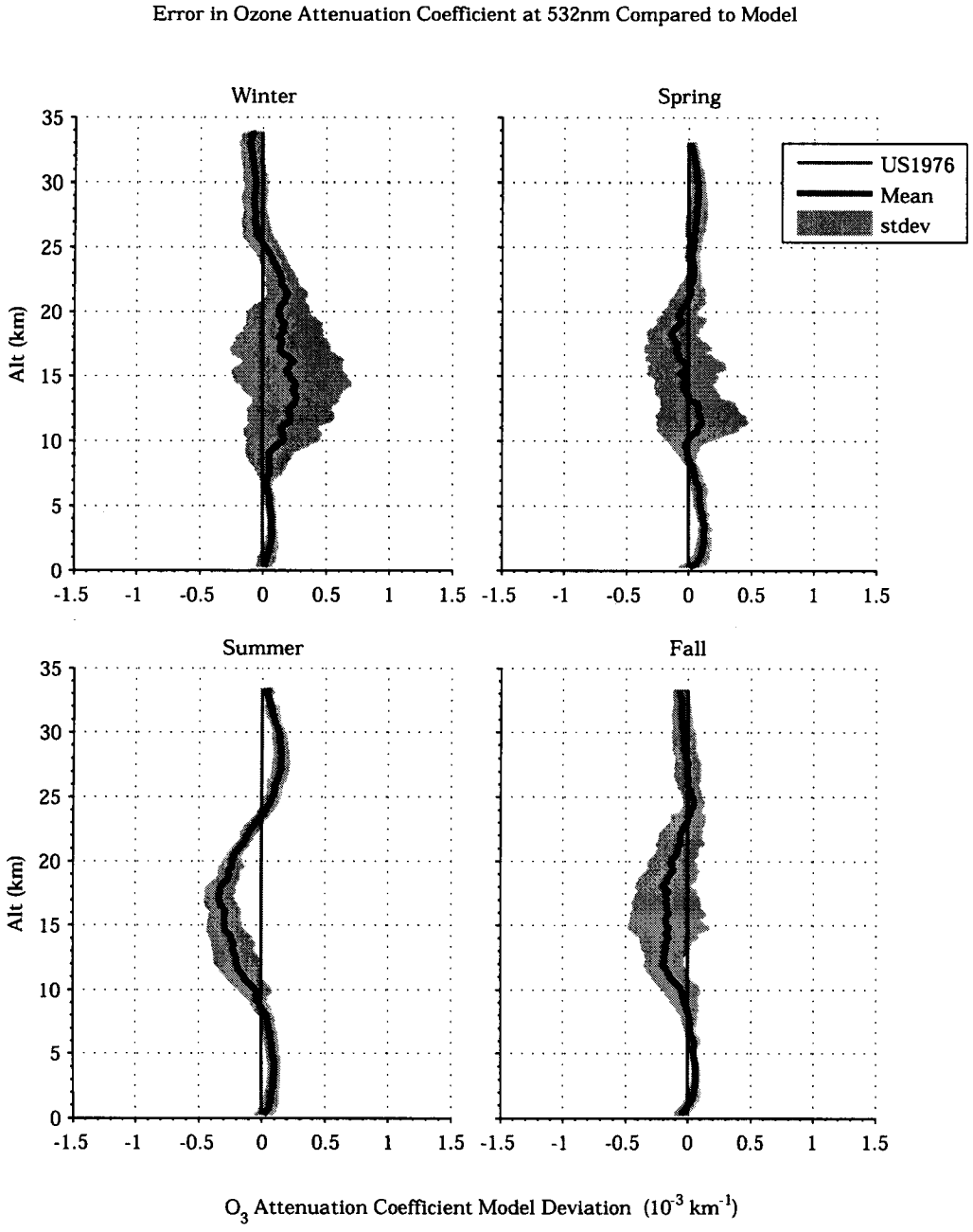

Figure 2.9: Difference in quarterly ozone extinction calculated using ozonesonde profiles from US1976 at 532 nm. The standard deviation of the profiles is also shown.

2.2.1 Transmission

In addition to the error in the ozone extinction at a given height associated with the difference between the assumed and actual ozone concentrations, there is also an error in the accumulated transmission profiles. Transmission profiles are calculated from each ozone attenuation profile:

$$\mathbf{T}_{\lambda}^{O_3}(z) = \exp\left(-\int_0^z \alpha_{\lambda}^{O_3}(z')dz'\right) \tag{2.5}$$

Ozone absorption results in an average reduction in signal power at 532 nm of 2% (Figure 2.10) from the ground to 50 km. At 607 nm this reduction is 5% (Figure A.5).

The error in the transmission determination has no effect on the aerosol extinction measurements (1.22) and only a very small relative effect on the aerosol backscatter (1.17), which is dependent on the differential absorption at 532 and 607 nm (the ratio of the transmissions). Due to the small difference in the transmissions at these two wavelengths and the low magnitude of the transmissions up to 15 km (less than a 1% effect on signal power), the effect of ozone transmission can typically be ignored in the measurement of aerosol backscatter – and is quite adequately accounted for through the use of a model profile.

The effect of error in the determination of ozone transmission profiles is much more significant for Raman density and temperature retrievals, which are dependent on the product of the transmissions at 532 and 607 nm (Figure 2.11). Rayleigh temperature retrievals in the troposphere and stratosphere are similarly affected by the two-way transmission at 532 nm (Figure A.6). The results for two-way transmission at 532 nm are comparable to previous work (Sica et al., 2001).

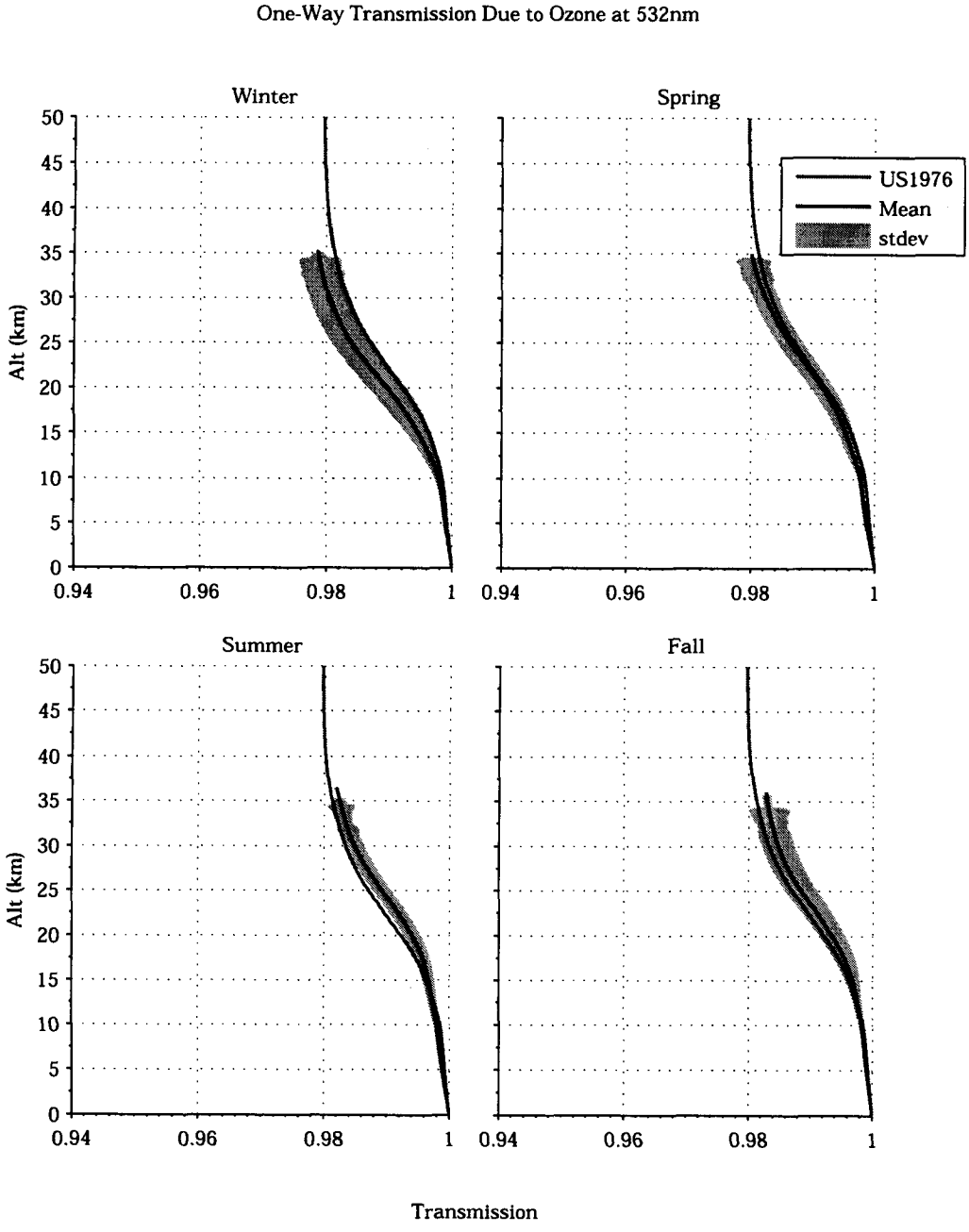

Figure 2.10: Transmission decrease due to ozone at 532 nm, normalized at 300 m.

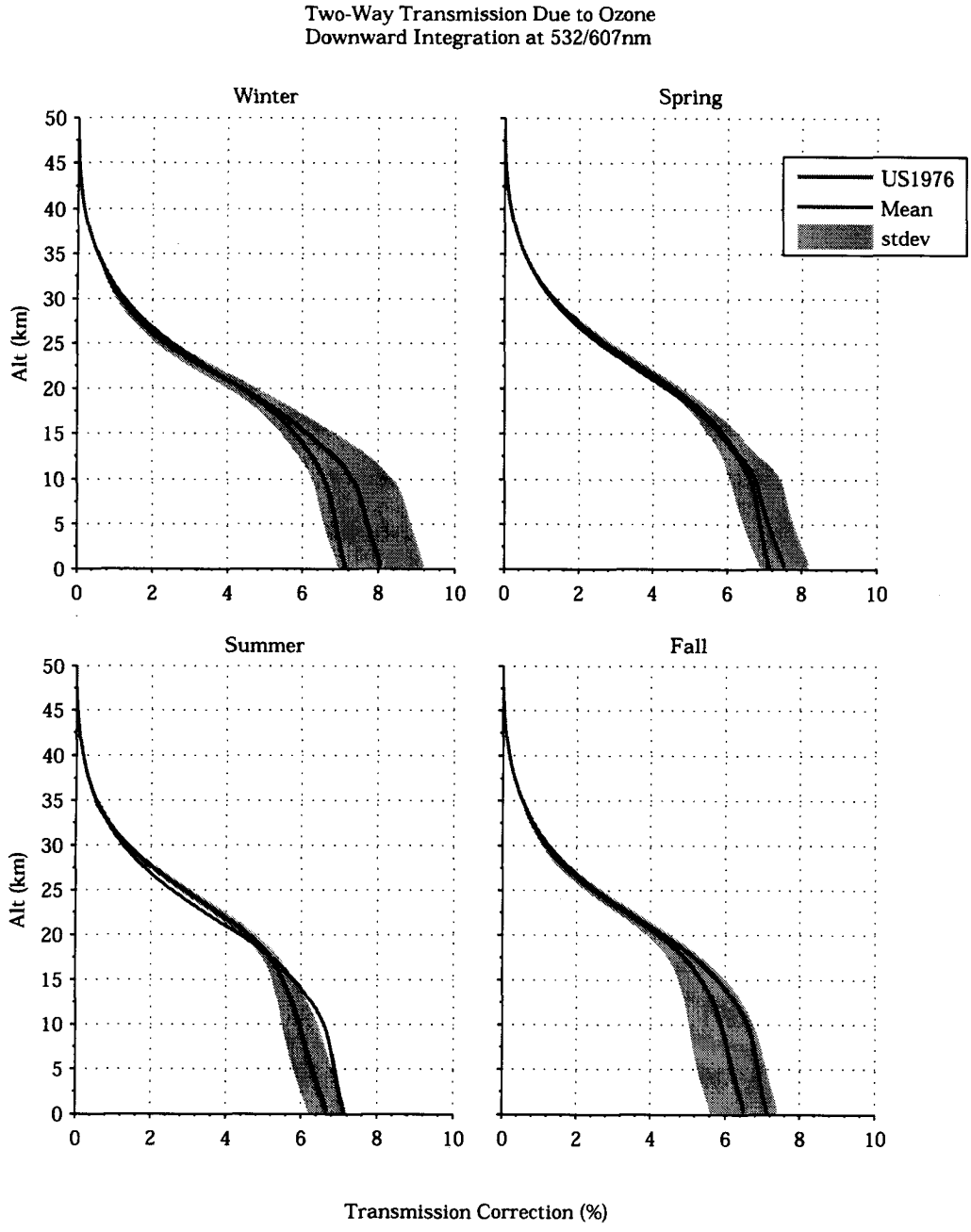

Figure 2.11: Raman Lidar two-way ozone transmission profile at 532 nm (up) and 607 nm (down), normalized at 50 km and expressed as a relative percentage above 100%.

If the transmission component due to ozone absorption is completely ignored, ($\mathbf{T}^{O_3}_{\lambda_0}(z) = \mathbf{T}^{O_3}_{\lambda_{N2}}(z) = 1$), there is a resulting 6.5% average error at 12 km (relative to normalization at 50 km) that propagates to a corresponding 6.5% over-estimation of the atmospheric density when using N_2-Raman Lidar retrieval.

The seasonal ozone transmission model is 0.6% higher at 12 km than US1976 in Winter and 0.5% lower in Summer. This has important implications for Lidar climatologies as it would translate into a perceived mean inter-seasonal fluctuation in atmospheric density (and corresponding pressure and temperature) of 1.1%, caused by ozone changes. These discrepencies get stronger with decreasing altitude.

Even if a quarterly ozone model was used, fluctuations in seasonal ozone concentrations year-over-year could conceivably be incorrectly registered as density and temperature changes by Lidar retrieval if not properly accounted for. As atmospheric conditions and ozone concentrations are certainly correlated, this could either exaggerate or mask attempts to measure small changes in atmospheric conditions (depending on the type of correlation).

The expected day-to-day variability of the two-way N_2-Raman transmission profiles is represented by the standard deviation of all the profiles within each quarter, which is 0.9% at 12 km in Winter and 0.4% in Summer. This is the resulting systematic error to be expected if averaged quarterly ozone profiles are used in place of concurrent measurements. All PCL density and temperature measurements on a given night (along with most other Lidar systems) will incurr this error (at minimum) in the absence of concurrent ozone measurements.

2.3 MODTRAN Model Aerosol Extinction

In many tropospheric and stratospheric Lidar applications where aerosol measurements are not available, it is necessary to use values from models. In the absence of significant aerosol loading (clouds or smoke), the error associated with this assumption is relatively low in applications that are dependent on the differential transmission (the ratio of transmissions) at two close wavelengths, such as Lidar water vapour retrievals. For other applications dependent on the product of the transmission(s), such as density and temperature retrieval, the magnitude and variability of the aerosol transmission is such that the associated error in using a model transmission is too large for most applications, except perhaps where significant averaging over many nights of observation is performed.

A common method for obtaining reference model transmission profiles is with MODTRAN. MODTRAN is a moderate-resolution computer program developed by the United States Air Force for calculating atmospheric transmittance with resolution in the visible region on the order of 0.08 nm (Berk et al., 1989).

MODTRAN has a limited choice of built-in density and background aerosol models. Version 3.5 of the MODTRAN software is used to obtain transmission profiles at 532 nm and 607 nm using the US1976 Standard Atmosphere with and without the built-in "rural aerosols with 23 km visibility" model. In order to obtain the signal transmission due to the aerosols themselves (without the effects of the atmosphere), the output transmission profile for the atmosphere with aerosols is divided by the profile without. A three-point, zero-centered derivative filter is then applied to the transmission profiles to obtain attenuation coefficients (Figure 2.12).

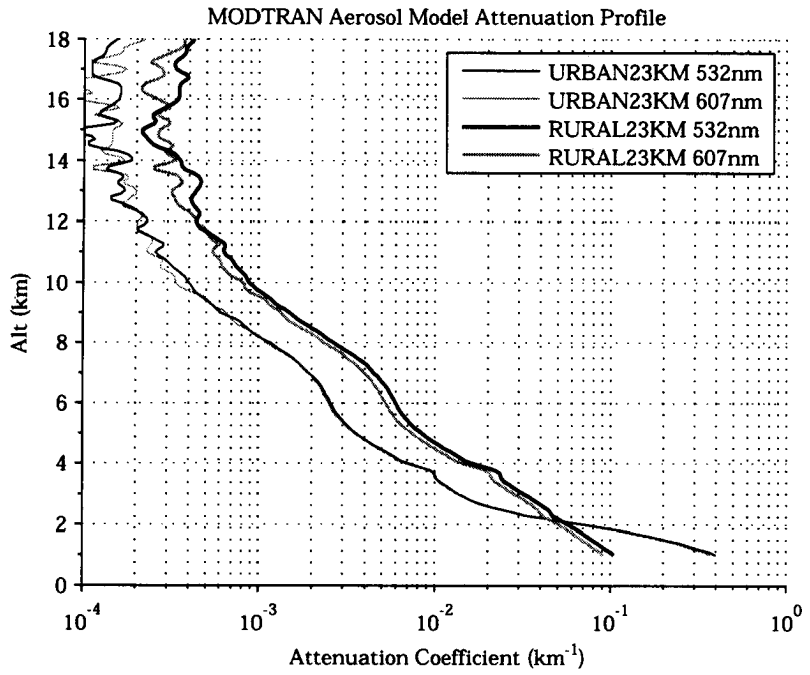

Figure 2.12: MODTRAN 3.5 output results: Aerosol attenuation profile for RURAL 23 km HAZE aerosol model at 532 nm and 607 nm.

In order to test the validity of some of the previous results, the MODTRAN attenuation profile for the aerosol-free US1976 atmosphere is compared to the combined Rayleigh scattering (Section 2.1) and ozone absorption (Section 2.2) attenuation profiles for US1976 from the previous sections (Figure 2.13). The agreement is good, except for slightly lower values in the MODTRAN profile for 607 nm between 8 and 40 km. This is likely due to the use of updated ozone cross-sections since the publication of the MODTRAN code.

By extracting the RURAL23KM aerosol model transmission profile from MODTRAN (Figure 2.14), a complete atmospheric model transmission profile can be obtained by combining the aerosol model with the ozonesonde-measured Rayleigh scattering and ozone absorption quarterly transmission profiles from the previous sections. This model, having been calculated from a relatively

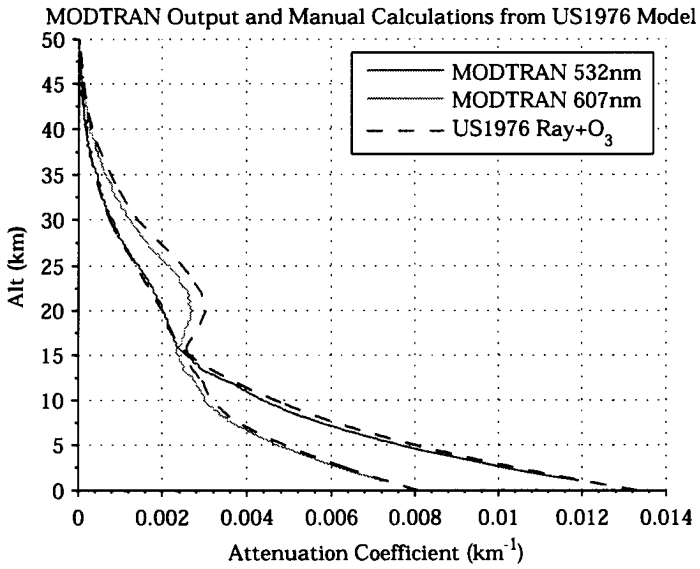

Figure 2.13: MODTRAN 3.5 output results: Total attenuation profile for aerosol-free atmosphere at 532 nm and 607 nm.

close, analogous site, offers some minor improvements over the generic model atmospheres used by MODTRAN. The aerosols, being the strongest and most variable source of attenuation at lower altitudes; however, remain the the largest source of uncertainty in this model.

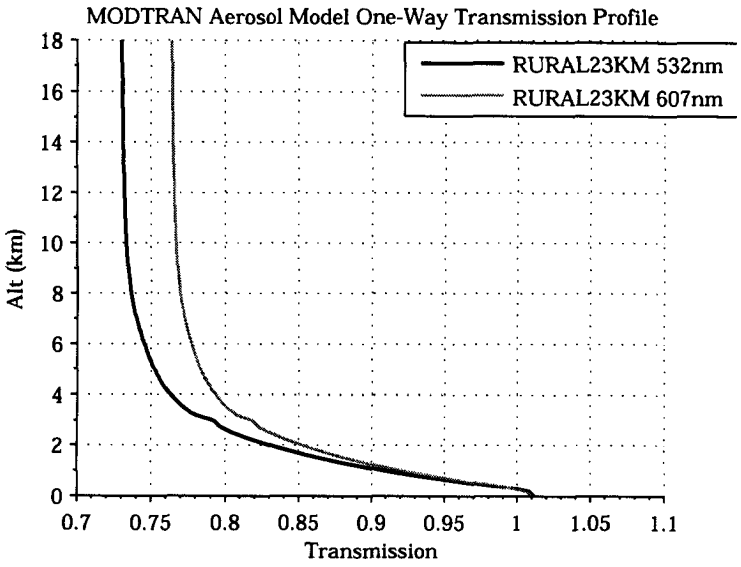

Figure 2.14: MODTRAN One-way aerosol transmission profiles.

Chapter 3

Measurement of the PCL Overlap Function

In order to obtain aerosol extinction measurements, it is necessary to know the overlap function of the PCL's receiver system (1.22). In practice this is difficult to determine analytically (Wandinger and Ansmann, 2002). It requires precise knowledge of the laser beam path, beam divergence and receiver optics. An experimental approach is therefore employed following the Raman-Lidar approach of Wandinger and Ansmann (2002). This approach is to re-arrange the basic Rayleigh and N_2-Raman scattering equations (1.3, 1.9) to obtain an analytic expression for the overlap function, $O(z)$.

$$\mathbf{P}_{\lambda_0}(z) = K_{\lambda_0}\frac{O(z)}{z^2}\left[\beta^{\text{ray}}_{\lambda_0}(z)+\beta^{\text{aer}}_{\lambda_0}(z)\right]\mathbf{T}^2_{\lambda_0}(z) \tag{1.3}$$

$$\mathbf{P}_{\lambda_{N2}}(z) = K'_{\lambda_{N2}}\frac{O(z)}{z^2}N_{\text{total}}(z)\mathbf{T}_{\lambda_0}(z)\mathbf{T}_{\lambda_{N2}}(z) \tag{1.9}$$

The optics inside the PCL detector system are arranged such that the focal lengths of the Rayleigh and N_2 Raman channels are the same, thus producing

the same field of view and corresponding overlap function. Equation (1.9) can be re-written to express $O(z)$ as (Wandinger and Ansmann, 2002):

$$O(z) = \frac{z^2 \mathbf{P}_{\lambda_R}(z)}{K'_{\lambda_R} N_{\text{total}}(z) \mathbf{T}_{\lambda_0}(z) \mathbf{T}_{\lambda_R}(z)} \tag{3.1}$$

To determine the overlap function requires knowledge of the measured laser power, molecular density and atmospheric transmission at the laser and N_2 Raman wavelength as a function of altitude as well as a system constant. A well-behaved overlap function for a properly aligned Lidar system should nominally converge to a value above a certain altitude, which is normalized to one ($O(z_0) = 1$ above some altitude, z_0). The constant in (3.1) can therefore be eliminated by dividing (3.1) by $O(z_0)$ and dropping the redundant term K'_{λ_R} appearing in the numerator and denominator:

$$\begin{aligned} O'(z) &= \frac{z^2 \mathbf{P}_{\lambda_R}(z)}{N_{\text{total}}(z) \mathbf{T}_{\lambda_0}(z) \mathbf{T}_{\lambda_R}(z)} \\ O(z) &= \frac{O'(z)}{O'(z_0)} \end{aligned} \tag{3.2}$$

A set of 15 summer nights, found to be cloudless and free of significant aerosol loading through examination of the raw Rayleigh photocount profiles for any sharp increases in photocount returns, was considered for calculation of a mean nightly overlap function (Table 3.1). The data collection for these dates, on average, started at 3:15UT and lasted 5 hours and 10 minutes.

To obtain atmospheric density profiles, $N_{\text{total}}(z)$, in-situ measurements are used from regular balloon-borne radiosonde flights by the National Oceanic and Atmospheric Administration (NOAA) at Detroit, MI (WMO 72632, 42.70N 83.47W - approximately 170km south-west of the PCL) (Schwartz and Govett, 1992). The flights are performed nightly at 0000UT and are taken to be a

2007-07-12
2007-07-31 *
2007-06-09
2007-06-10
2006-06-15
2006-06-11 *
2005-07-10 *
2005-07-31
2002-06-19 *
2002-05-19
2002-08-25 *
2000-07-24 *
2000-06-23 *
2000-06-19 *
2000-06-16
2000-05-26

Table 3.1: List of cloudless summer nights for which the overlap was calculated. Profiles that converge at high altitudes and that were used in the calculation of the mean overlap profile are marked with an asterix (*)

reasonable representation of the conditions at the PCL.

The atmospheric transmissions $\mathbf{T}_{\lambda_0}(z)$ and $\mathbf{T}_{\lambda_R}(z)$ are calculated as the product of the Rayleigh scattering seasonal model, ozone seasonal model, and the aerosol model from MODTRAN 3.5. It is assumed that this represents a suitable average for the atmospheric conditions across the nights in Table 3.1.

The overlap function is calculated using the N_2-Raman Lidar photocounts summed for the entire night, radiosonde densities measured earlier in the night, and model transmission values (Figure 3.1). These profiles are normalized between 15 and 18 km. About half of these nights are found not to converge (Figure 3.2). The normalization assures that the cause for this error must be one that varies with height. This is most likely an operator-dependent focusing, alignment or Lidar pointing problem on these nights. The overlap function is important for all altitudes below 12 km (at 12 km, the value is

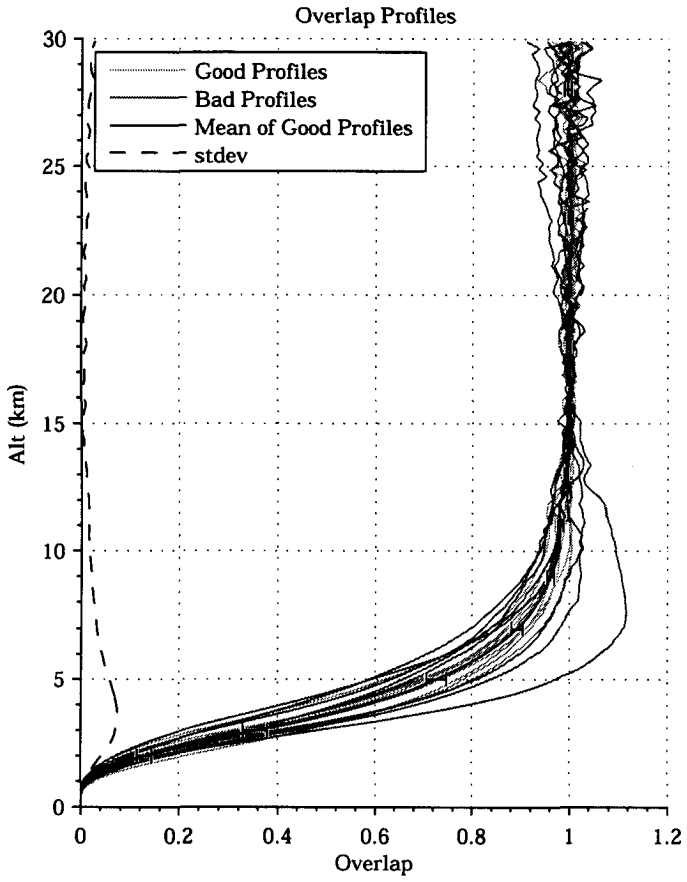

Figure 3.1: Mean mirror overlap function, with standard error. Standard deviation is also shown. The individual bad profiles are also plotted, as are the individual good profiles (light coloured, faintly visible under the other plots).

0.99).

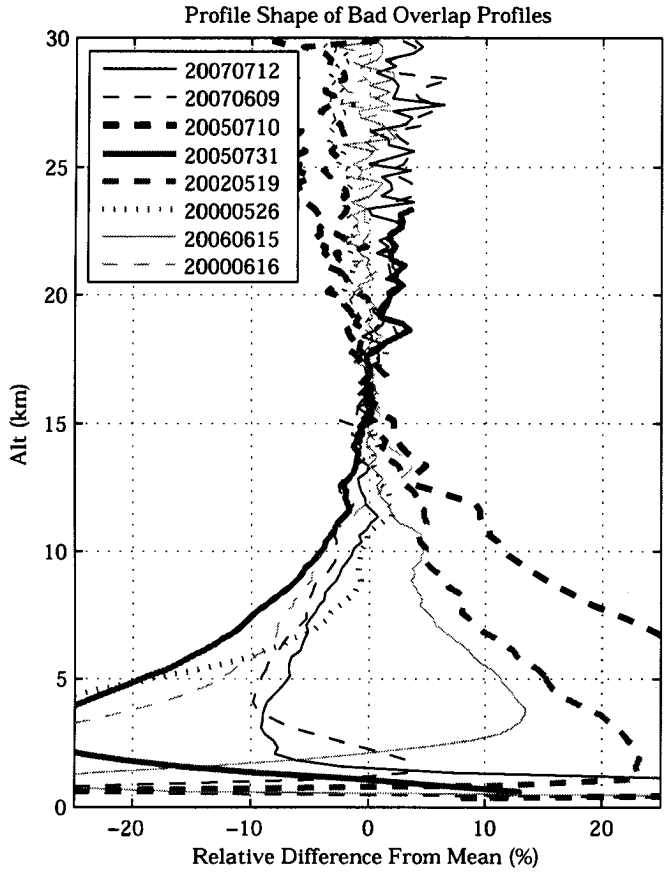

Figure 3.2: Individual bad overlap profiles, shown relative to the average of the good overlap profiles. Likely due to bad focusing.

Discrepancies in the tropopause height between the Detroit radiosonde measurements and the actual conditions at the PCL during data collection can produce "bumps" in the derived overlap profile at the tropopause height. This is due to the drop in the density that occurs at the tropopause.

By its nature, the overlap function changes slowly and smoothly with altitude. Because derivatives are to be used (1.22) it is important to remove some

of the noise, which is an artifact of the data measurements. A 2 km moving average smoothing filter is applied to mitigate some of the high-frequency changes in the data. Complete convergence is forced by multiplying all values above 15 km by a rapidly decaying exponential function.

The true overlap profile is not constant. It is influenced particularly by the rotating liquid-mirror design of the PCL due to factors such as the rotational speed (affecting the focal length) and the environmental temperature (affecting the thermal expansion of the tripod legs and the focus of the mirror on the detector). Some of these factors will vary within a given night of observations, while others change from day-to-day. They are not fully random and contain definite biases due to the seasons, and the chosen operational parameters in place during observations.

The standard deviation gives a measure of the variability of the profiles about the mean value. This variability is primarily due to variations in the conditions for each night (mirror speed, aerosol loading) as opposed to random photocount error. The standard deviation of the overlap data describes the average systematic error introduced by using the mean value to replace the measurement for each night. There are several caveats with extending this average profile to be a universal overlap function for the PCL for all nights (both cloudy and not). Due to availability of suitably clear and consistent nights, a very small sampling of 8 good nights was used, all occurring in warmer months. Also, as the mean overlap profile was calculated from the summed photocounts for each night, the variability of the overlap throughout the night is obviously greater.

In order to use the calculated mean PCL overlap function for a given night, there is an implicit assumption that the conditions of the data collection are suitably close to those represented by the 8 nights used to derive the average.

Due to the small sample size, however, it is difficult at present to isolate the effect of each these conditions (mirror speed, temperature, etc.).

The overlap function is important specifically to the measurement of aerosols due to the appearance of the term $\frac{O'(z)}{O(z)}$ in the extinction coefficient calculation (1.23). The variability in this term is found simply by calculating its value for each of the clear nights, then determining the standard deviation of all the resulting profiles.

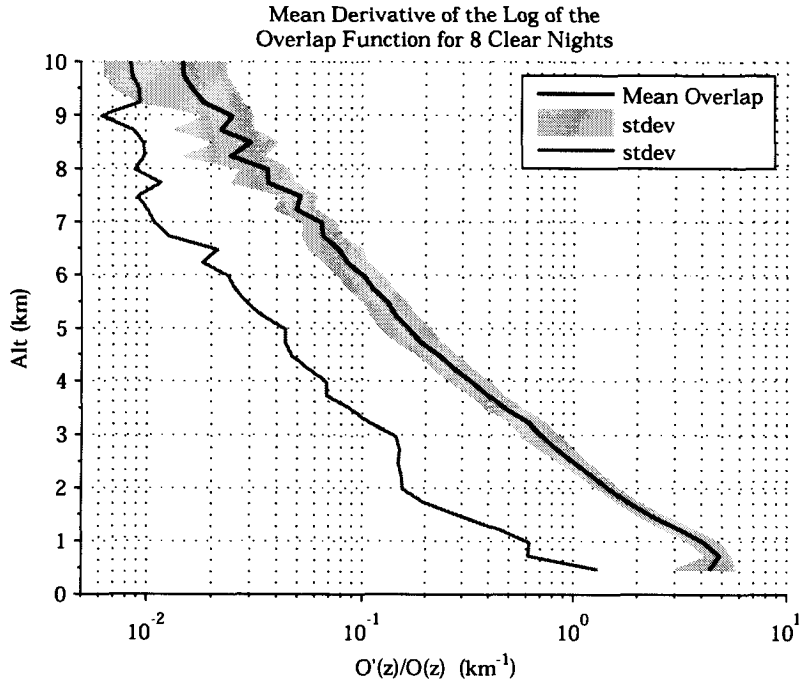

Figure 3.3: Error in aerosol extinction coefficient due to variability in overlap term.

It is not until 8 km that the error in the extinction coefficient due to the variability in the mirror overlap is reduced below 0.01 km^{-1} (Figure 3.3). Since this variability was calculated from good, stable overlap nights (all of which are in Summer), it is likely a lower-bound to the actual mirror variability across all nights. Many nights will no doubt exhibit much more variable behaviour.

Until the mirror overlap behaviour can be determined more accurately, or made to be more consistent, reliable extinction measurements are only taken above 8 km.

Chapter 4

Measurement of the PCL Shutter Function

The Rayleigh channel on the Purple Crow Lidar is designed for high-sensitivity measurements in the middle-upper atmosphere. A rotating mechanical shutter-chopper, synchronized to the laser pulses, is set up to block all light from entering the detector at lower altitudes. In practice, the blades of the shutter take a finite amount of time to cut through the signal, resulting in a smooth transition between the open and closed states. The average photocount profile for a clear night is shown in Figure 4.1.

The altitude at which the shutter aperture is fully open, referred to as the shutter height, is controlled by an adjustable setting and is typically set to 28-30 km. It was believed that the shutter was fully closed at around 12 km, since the photocounts start to increase rapidly at this height; however, a signal is clearly seen to persist in the 0-12 km range. This "leaked" signal, while weak, has been used to locate strongly-scattering clouds and other aerosols as coherent increases in the photocount over the relative background. This

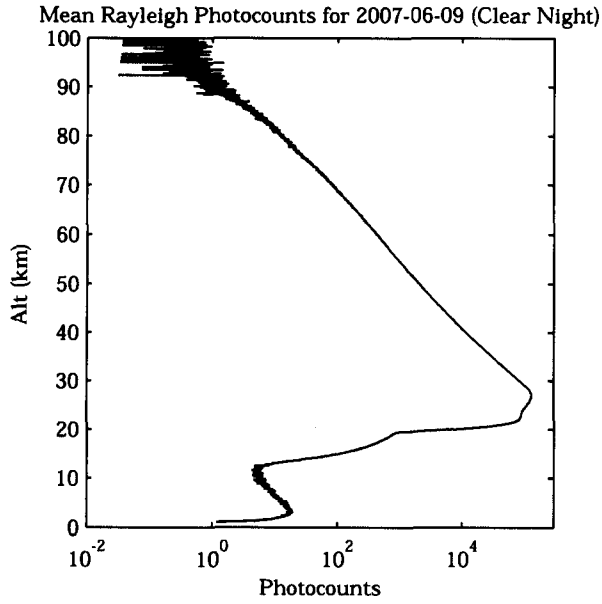

Figure 4.1: Average, normalized raw counts for 2007-06-09, a cloudless night.

method is particularly effective when the counts are plotted as a grid plot in dimensions of both time and altitude (Figure 4.2), which internally were given the name Cloud Plots. While these plots are useful in observing the presence of aerosols, they do not provide much in the way of physical measurements.

It was originally thought that the leaked signal had a constant effect, reducing the incoming signal by a fixed amount once the shutter was in a "closed" position, for all altitudes below 12 km. Initial attempts to calculate the aerosol scattering ratio for a cloudless night (the relative increase of total backscatter with aerosols over Rayleigh backscatter background) using (1.17) produced a consistent function varying with altitude, rather than a constant value as would be expected (Figure 4.3).

Since the Rayleigh and Raman detector optics are configured to have the same optical arrangement and therefore the same overlap function, $O(z)$, it was thought that this behaviour must be due to a continuous shutter effect

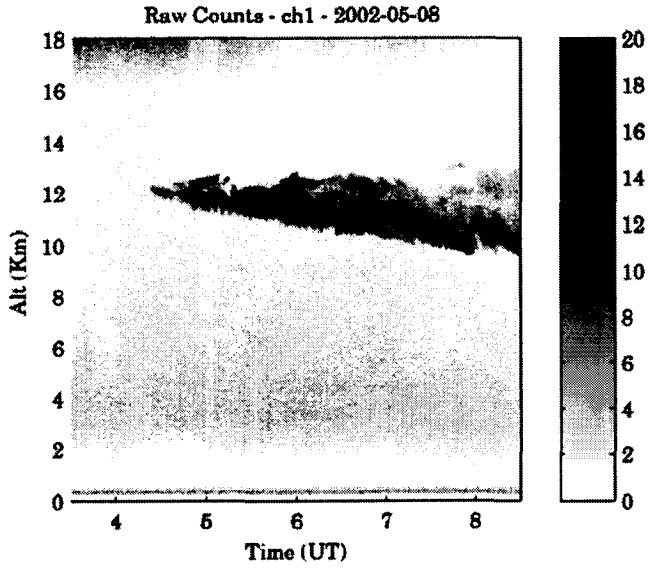

Figure 4.2: Old PCL "Cloud Plot" - Raw Rayleigh counts for 2002-05-08. A cirrostratus-like cloud is clearly visible.

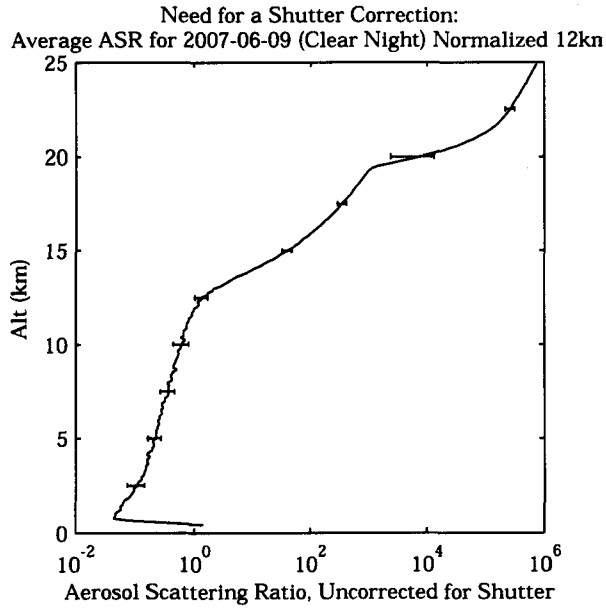

Figure 4.3: Average aerosol scattering ratio calculated as per (1.17) for 2007-06-09, a predominantly clear night. The ASR is calculated using MODTRAN transmission profiles and normalized to 12 km. The fact that the result is not close to one indicates an additional height-dependent effect not accounted for in the Lidar equation (1.1). The standard deviation of the data is shown.

– that the shutter effectively never fully "closes". A special operation of the PCL with the shutter effectively turned off confirmed this hypothesis, as the identical calculation of the aerosol scattering ratio using (1.17) yielded sensible results (and some aerosol features), without the modulating function.

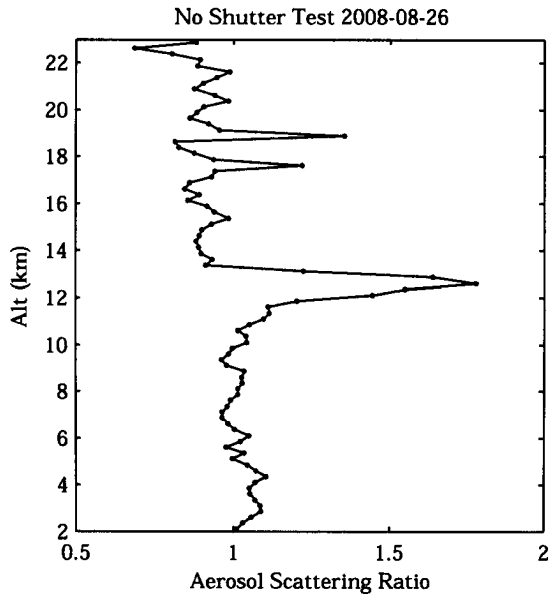

Figure 4.4: Average aerosol scattering ratio calculated as per (1.17) for 2008-08-26, with no shutter. The same strong height-dependent effect in 4.3 is not present. Several aerosol features are suspected at 12, 17 and 19 km.

Since the rotation of the shutter is synchronized with laser shots, the time-dependent effect of the shutter can be translated into a repeating altitude-dependent effect on the photocounts (so long as the set open-shutter altitude is constant, and the optical configuration inside the detector box unchanged). An additional term, the **shutter function** $S(z)$, is introduced to the elastic Lidar equation (1.3) to encompass the effect of the shutter.

$$\mathbf{P}_{\lambda_0}(z) = K_{\lambda_0} S(z) \frac{O(z)}{z^2} \left[\beta^{\text{ray}}_{\lambda_0}(z) + \beta^{\text{aer}}_{\lambda_0}(z)\right] \mathbf{T}^2_{\lambda_0}(z) \tag{4.1}$$

This form of the Rayleigh Lidar equation need only be used for analysis below the shutter height (30 km), as $S(z)$ is defined to be otherwise equal to one above this regime. The Raman channels, as they are not chopped, remain unchanged. Using this modified Lidar equation, the equation for the aerosol scattering ratio (1.17) becomes

$$\begin{aligned} R'(z) &= \frac{1}{S(z)} \frac{\mathbf{P}_{\lambda_0}(z)}{\mathbf{P}_{\lambda_{N2}}(z)} \frac{\mathbf{T}_{\lambda_{N2}}(z)}{\mathbf{T}_{\lambda_0}(z)} \\ R(z) &= \frac{R'(z)}{R'(z_0)} \end{aligned} \tag{4.2}$$

In the absence of aerosols, $R(z) = 1$. For these regions, where the transmission is known, it is possible to deduce the form of $S(z)$:

$$S(z) = \frac{\mathbf{P}_{\lambda_0}(z)}{\mathbf{P}_{\lambda_{N2}}(z)} \frac{\mathbf{T}_{\lambda_{N2}}(z)}{\mathbf{T}_{\lambda_0}(z)} \tag{4.3}$$

It is important to note that the near-field overlap $O(z)$ does not appear in the calculation of $S(z)$. The shutter function is also not affected by optical focusing or alignment problems that affect both the elastic and the N_2-Raman detection channels equally. It is assumed that there are no differential optical issues in the data across those detection channels, although this possibility warrants investigation.

The first approach to determine $S(z)$ was to use measurements of the aerosol extinction coefficient, which are not affected by the shutter, to determine regions containing aerosols for a given night. Equation (4.3) could then be applied to the aerosol-free regions, with interpolation of values through the aerosol-laden regions.

This approach was useful, but suffered from a number of important drawbacks. Measurements containing aerosols not detected from the extinction

values (false negatives) significantly alter the resulting shutter function. Additionally, the interpolation of values can introduce significant error particularly within thick aerosol layers and where the shutter function changes rapidly with height. Since these interpolated regions are precisely where an accurate shutter function profile is sought in order to measure these aerosols, this method was abandoned in favour of a different approach.

The average nightly shutter function was calculated for 9 cloudless nights with good optical alignment (Table 3.1). The resulting profiles show three general groupings (Figure 4.5). All nights tend to show a marked increased in the shutter function around either 12, 15 or 16 km. The 12 km profiles all used shutter heights of 28 km, while the 15 and 16 km profiles (occurring in 2000 and 2002, respectively) all used a setting of 30 km. The reason for the difference in the 2000 and 2002 functions is not clear, but it is likely due to a mechanical or optical change made sometime in between these periods.

The average of the clear-night shutter functions are calculated for each of the three groups, corresponding to shutter settings of 28 km, 30 km and 30 km-2002. These averaged shutter functions are then used as references for other nights. There aren't many nights of measurement in the calculation of each of the reference functions, but they do appear to behave consistently in the 5 to 18 km range where aerosol measurements are sought (Figure 4.5).

The basic approach to determining the shutter function for a given night is to assume that the Lidar was operated under the same optical and mechanical conditions as one of the three reference profiles. The most suitable reference profile is selected by comparing the three to the shutter function calculated using (4.3) for the night in question without any correction for aerosols. The aerosol-free altitude ranges of the calculated shutter function are examined to determine the most suitable reference profile. A small ad-hoc adjustment

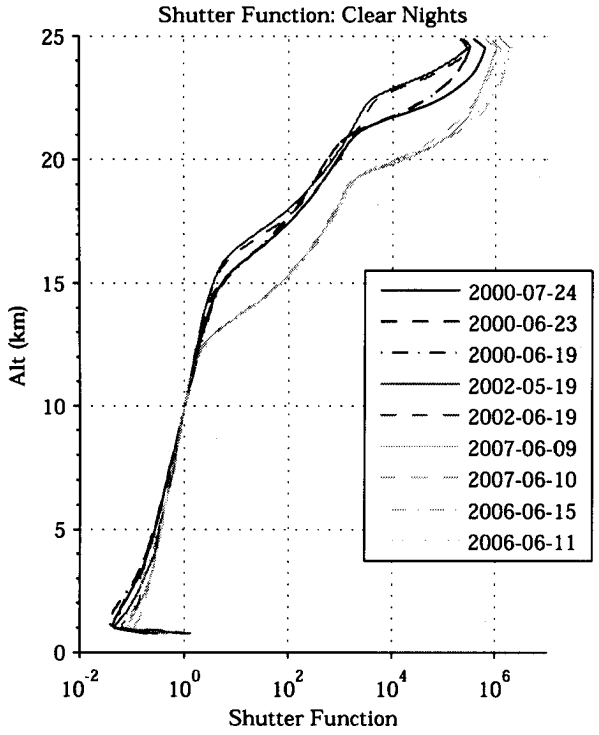

Figure 4.5: Shutter function (4.3) calculated using the average Rayleigh and N_2-Raman profiles for 9 clear nights.

by vertically shifting and scaling of the reference profile is also allowed to improve the fit with the calculated profile, so long as the general shape of the profiles is initially similar. This fit is done visually with the assistance of a custom graphical user interface (GUI) tool written specifically for this purpose (Figure 4.6). Once a suitable shutter correction is found, the aerosol backscatter can then be calculated (4.2).

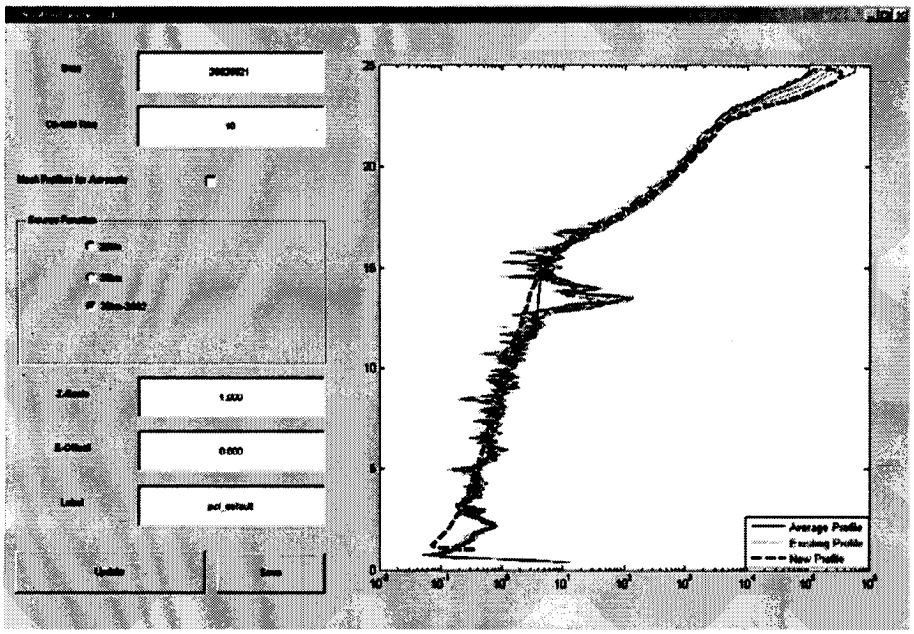

Figure 4.6: Screen capture of the shutter function GUI tool. Data for 2002-06-21 is shown. The 30 km-2002 profile is shown as the thick, dashed line, and is compared to ensure agreement with the average shutter function profiles calculated every 10 minutes throughout the night. Aerosols are present between 12 and 15 km.

Despite the selection of cloud-free nights for the calculation of the reference shutter functions, the troposphere is still loaded with an unknown profile of highly-variable background aerosols. The likely deviation with respect to the assumed model aerosol distribution on these nights (Figure 2.12) – particularly given the low number of nights averaged – gives rise to appreciable error in

the resulting shutter functions at these lower altitudes. The error in the assumed shutter behaviour increases with distance from the altitude of clear-sky normalization, which is generally taken to be in the upper troposphere.

For these reasons, the interpretation of aerosol backscatter measurements is generally restricted to the regime above 8 km, near the clear-sky normalization altitude. This still allows for reliable determination of backscatter for many high-altitude aerosol events, beyond the range of many other aerosol Lidar systems.

Chapter 5

Results

In the previous sections, equations were derived for the aerosol backscatter coefficient, $\beta_{\lambda_0}^{\text{aer}}(z)$, the aerosol extinction coefficient, $\alpha_{\lambda_0}^{\text{aer}}(z)$, and the extinction-to-backscatter or Lidar ratio, γ:

$$\begin{aligned} R'(z) &= \frac{1}{S(z)} \frac{\mathbf{P}_{\lambda_0}(z)}{\mathbf{P}_{\lambda_{\text{N2}}}(z)} \frac{\mathbf{T}_{\lambda_{\text{N2}}}(z)}{\mathbf{T}_{\lambda_0}(z)} \\ R(z) &= \frac{R'(z)}{R'(z_0)} \qquad (4.2) \\ \beta_{\lambda_0}^{\text{aer}}(z) &= \beta_{\lambda_0}^{\text{ray}}(z)(R(z)-1) \qquad (1.18) \end{aligned}$$

$$\alpha_{\lambda_0}^{\text{aer}}(z) = \frac{\left[\frac{O'(z)}{O(z)} + \frac{N'_{\text{total}}(z)}{N_{\text{total}}(z)} - \frac{2}{z} - \frac{\mathbf{P'}_{\lambda_{\text{N2}}}(z)}{\mathbf{P}_{\lambda_{\text{N2}}}(z)}\right] - \alpha_i}{1 + \left(\frac{\lambda_{\lambda_0}}{\lambda_{\lambda_{\text{N2}}}}\right)^k} \qquad (1.23)$$

$$\gamma = \frac{\alpha_{\lambda_0}^{\text{aer}}}{\beta_{\lambda_0}^{\text{aer}}} \qquad (1.24)$$

Having measured the unknown system parameters and defined the expected error with the necessary assumptions, it is now fairly straightforward to cal-

culate the aerosol measurements.

Determination of the aerosol extinction is performed with Lidar photocount data, $\mathbf{P}(z)$, combined with radiosonde measurements by NOAA at Detroit, MI (WMO 72632, 42.70N 83.47W) (Schwartz and Govett, 1992) to obtain the density $N_{\text{total}}(z)$ and Rayleigh extinction coefficient $\alpha_{\lambda}^{\text{ray}}(z)$. The overlap function calculated in Section 3 is used as is the seasonal ozone extinction model profile $\alpha_{\lambda}^{O_3}(z)$ in Section 2.2. A value of k = 1 is assumed, since this is the norm and the potential error associated with this assumption is small (Ansmann et al., 1990).

Aerosol backscatter is found using the PCL photocount data $\mathbf{P}(z)$, shutter function $S(z)$ (Section 4), seasonal model transmissions Rayleigh (Section 2.1) and Ozone (Section 2.2) transmissions along with the MODTRAN-derived aerosol model $\mathbf{T}(z)$ and radiosonde density to obtain $\beta_{\lambda_0}^{\text{ray}}(z)$.

Since the use of the transmission profiles in the aerosol scattering ratio (4.2) involves a ratio at two relatively close wavelengths, the error associated with the use of model atmospheres is significantly reduced – for the ozone and Rayleigh transmission components this error is negligible. Variability in the transmission profiles is primarily due to the presence of aerosols.

One of the benefits of the dual Rayleigh-Raman aerosol Lidar setup is that the independent aerosol extinction measurements can be used to determine the aerosol component of the transmission profile, which can then be used to improve backscatter measurements. This correction is applied for nights with broad aerosol features. For relatively thin features of little attenuation where the backscatter is normalized to a clear region close to the feature – no attenuation correction is made, so as not to introduce additional error from the attenuation determination.

The presence of attenuating aerosols increases the relative term $\frac{T_{\lambda_{N2}}(z)}{T_{\lambda_0}(z)}$ in the aerosol scattering ratio (4.2) since aerosols attenuate more (and therefore have lower transmission values) at the shorter wavelength λ_0. When measuring broad aerosol features, if no correction is made for the attenuation of the feature itself, this causes upper regions of the feature to be measured as having weaker backscatter than if the attenuation is properly corrected.

The Rayleigh extinction coefficient can be determined directly from the atmospheric density (2.1). Since routine Radiosonde data from Detroit is readily available from NOAA and reasonably considered to be a better approximation than a generic model, it is used to calculate Rayleigh extinction coefficients.

Having accurate density measurements is highly desirable for accurate aerosol backscatter measurements. It is assumed that the use of in-situ radiosonde measurements from Detroit provides a more accurate representation of conditions at the PCL site than seasonal averages due to the general eastward circulation; however, no analysis has been made to compare the two sites.

For long-term, routine measurements it may be desirable to use a model atmosphere for consistency in the measurements. This potentially avoids complication in also interpreting variability or error in the radiosonde measurements in addition to the PCL measurements. For instance, the change in density at the tropopause has a notable impact on extinction (1.23) values. This can result in systematic error in the extinction profile at the altitude of the actual tropopause above the PCL and at that measured by the radiosonde over Detroit when these two differ. It may be preferable to use a constant density model to keep the assumed tropopause altitude fixed.

The addition of a pair of suitable detection channel wavelengths to the PCL

for measurement of Ozone concentrations through the differential absorption (DIAL) technique would provide some benefits to aerosol measurements – although these would primarily be in improved accuracy of the transmission profiles, thereby allowing for better calibration parameters, such as the overlap function.

For the measurement of aerosol features, it is generally desirable to retain as much range resolution as possible. Due to the large bin size of the N_2-Raman channel (250 m), a three-point difference filter is used in the calculation of the derivative in the aerosol extinction coefficient (1.23). While noisy, this approach retains most of the definition in rapidly-varying aerosol features. Gains in signal-to-noise are attained mainly through temporal summing of photocounts, typically into bins of around 5 minutes for creating two-dimensional grid plots in altitude and time. Further refinements are likely possible through the use of more sophisticated, edge-preserving filters.

The bulk of the systematic error in the measurement of aerosol extinction (1.23) in the 8-15 km range arises from differences in the actual conditions at the PCL site reflected in $\frac{\mathbf{P}'_{\lambda_{N2}}(z)}{\mathbf{P}_{\lambda_{N2}}(z)}$ and the assumed density profile measured by Detroit radiosonde in the term $\frac{N'_{\text{total}}(z)}{N_{\text{total}}(z)}$. This error is particularly strong in the vicinity of temperature inversions.

Temperature inversions tend to have higher rates of density decrease with altitude. A temperature inversion in the radiosonde profile will lower the resulting extinction attributed to aerosols while a temperature inversion at the PCL site causes an increase in aerosol extinction (due to the effect on $\frac{\mathbf{P}'_{\lambda_{N2}}(z)}{\mathbf{P}_{\lambda_{N2}}(z)}$). When there is a discrepancy in the altitude of a temperature inversion (notably, at the tropopause), this often results in a spike in the aerosol extinction in either positive or negative direction, followed immediately by a spike in the opposite direction (an error-rebound effect). These deviations must be

quantified in order to validate interpretations of relatively weak extinction measurements.

Aerosol extinction values were calculated for the 16 nominally aerosol-free nights (Table 3.1) used in the determination of the overlap function. The free troposphere and lower stratosphere on these nights was assumed to be free of aerosols (8-20 km). The deviation from the assumed null result, which was greater than the photocount error, was taken to represent error in the assumed concurrency of the radiosonde density measurements with the Lidar observations (Figure 5.1). The standard deviation across all altitudes was found to be approximately 0.008 km^{-1}, with a maximum deviation of 0.03 km^{-1}. The extinction values varied rapidly with altitude. Except for the error-rebound effect due to temperature inversions, the systematic error due to the use of radiosonde density profiles can be characterized as pseudo-random with a standard deviation of 0.008 km^{-1}.

The error due to temperature inversions in the troposphere was found by Ansmann et al. (1990) to be 0.015 to 0.025 km^{-1} for inversions of 0 to 3 K/100m.

5.1 Error Calculations

The PCL aerosol coefficients, like most Lidar measurements, are prone to random error associated with discreet photon counting by the detectors. This error is well-defined by Poisson statistics (Johnson et al., 2005).

$$\sigma_P = \sqrt{P} \tag{5.1}$$

The random error in the aerosol backscatter (1.18) and extinction (1.23)

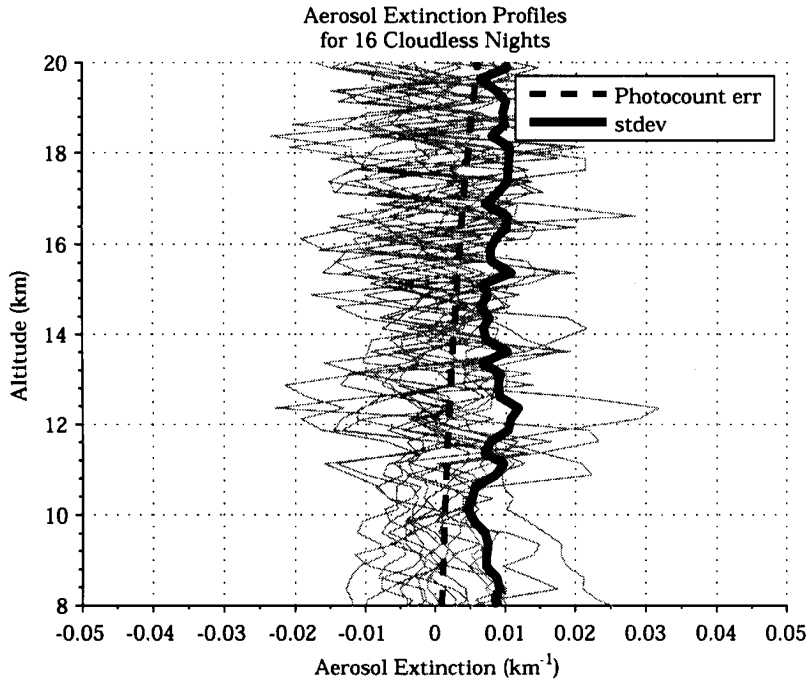

Figure 5.1: Aerosol extinction measurements for 16 "clear" nights. The variability is due to the use of radiosonde density profiles in the extinction calculation, which serves to quantify the systematic error associated with this assumption.

resulting from photocount error is straight-forward to determine from simple error propagation.

The resulting error in the intermediate quantity $R'(z)$ (1.17) is calculated as standard multiplicative error propagation of random, uncorrelated quantities P_{λ_0} and $P_{\lambda_{N2}}$. The transmission functions are assumed models obtained from seasonal averages and MODTRAN, and while they potentially contain appreciable deviation from actual conditions, this error is entirely systematic – the random error is taken to be zero.

$$\begin{aligned}\left(\frac{\sigma_{R'}}{R'}\right)^2 &= \left(\frac{\sigma_{P_{\lambda_0}}}{P_{\lambda_0}}\right)^2 + \left(\frac{\sigma_{P_{\lambda_{N2}}}}{P_{\lambda_{N2}}}\right)^2 \\ \left(\frac{\sigma_{R'}}{R'}\right)^2 &= \frac{1}{P_{\lambda_0}} + \frac{1}{P_{\lambda_{N2}}}\end{aligned} \tag{5.2}$$

By including the error in the normalization factor at z_0 (typically small, since z_0 is averaged over a range of altitudes), an expression is obtained for the photocount error in the aerosol scattering ratio, σ_R:

$$\begin{aligned}\left(\frac{\sigma_R}{R}\right)^2 &= \left(\frac{\sigma_{R'(z)}}{R'(z)}\right)^2 + \left(\frac{\sigma_{R'(z_0)}}{R'(z_0)}\right)^2 \\ \left(\frac{\sigma_R}{R}\right)^2 &= \frac{1}{P_{\lambda_0}(z)} + \frac{1}{P_{\lambda_{N2}}(z)} + \frac{1}{P_{\lambda_0}(z_0)} + \frac{1}{P_{\lambda_{N2}}(z_0)}\end{aligned} \tag{5.3}$$

The molecular backscatter coefficient $\beta^{\text{ray}}_{\lambda_0}(z)$ is obtained from in-situ radiosonde measurements, whose relative precision is taken to be much greater than the relative Lidar photocount error ($\sigma_{\beta^{\text{ray}}_{\lambda_0}} \ll \sigma_{\beta^{\text{aer}}_{\lambda_0}}$). While a systematic error is introduced by taking the Detroit radiosonde measurements to be the continuous conditions at the Lidar site over the course of the night, the random error is taken to be zero.

$$\sigma_{\beta_{\lambda_0}^{\text{aer}}} = R(z)\,\beta^{\text{ray}}(z)\sqrt{\frac{1}{P_{\lambda_0}(z)}+\frac{1}{P_{\lambda_{\text{N2}}}(z)}+\frac{1}{P_{\lambda_0}(z_0)}+\frac{1}{P_{\lambda_{\text{N2}}}(z_0)}} \tag{5.4}$$

The aerosol extinction coefficient (1.23) is conveniently separable as a sum of contributions. The photocount term appears as:

$$\begin{aligned} f &= \frac{1}{a}\frac{P'(z)}{P(z)} \\ \text{where } a &= -\left(1+\left(\frac{\lambda_{\lambda_0}}{\lambda_{\lambda_{\text{N2}}}}\right)^{k}\right) \end{aligned} \tag{5.5}$$

The derivative $P'(z)$ is calculated using a three-point, zero-centered difference filter, which is divided by the change in altitude. For a given measurement, $P(z)$, the point immediately preceding, P_{-1}, and following, P_{+1}, are used.

$$\begin{aligned} P' &= \frac{dP}{dz} = \frac{\Delta P}{\Delta z} = \frac{P_{+1}-P_{-1}}{z_{+1}-z_{-1}} \\ \sigma_{P'}^2 &= \left(P'\frac{\sigma_{\Delta P}}{\Delta P}\right)^2 + \left(P'\frac{\sigma_{\Delta z}}{\Delta z}\right)^2 \\ \sigma_z &\approx 0 \\ \sigma_{\Delta P}^2 &= \sigma_{P_{-1}}^2 + \sigma_{P_{+1}}^2 \\ \sigma_{P'}^2 &= \left(P'\frac{\sqrt{\sigma_{P_{-1}}^2+\sigma_{P_{+1}}^2}}{\Delta P}\right)^2 = \left(\frac{\Delta P}{\Delta z}\frac{\sqrt{\sigma_{P_{-1}}^2+\sigma_{P_{+1}}^2}}{\Delta P}\right)^2 \\ \sigma_{P'}^2 &= \left(\frac{\sqrt{\sigma_{P_{-1}}^2+\sigma_{P_{+1}}^2}}{\Delta z}\right)^2 \end{aligned}$$

$$\sigma^2_{P'} = \left(\frac{\sqrt{P_{-1}+P_{+1}}}{\Delta z}\right)^2 \tag{5.6}$$

The numerator and denominator terms in (5.5) each rely on measurements at different altitudes, and therefore can be viewed as separate quantities since the photocount error at each altitude is (in principle) uncorrelated. The use of the simple formula for multiplicative error propagation is therefore appropriate to determine the contribution of photocount error to the extinction coefficient:

$$\begin{aligned}
\sigma^2_f &= f^2\left[\left(\frac{\sigma_{P'}}{P'}\right)^2 + \left(\frac{\sigma_P}{P}\right)^2\right] \\
\sigma^2_f &= f^2\left[\left(\frac{\frac{\sqrt{P_{-1}+P_{+1}}}{\Delta z}}{\frac{\Delta P}{\Delta z}}\right)^2 + \left(\frac{\sqrt{P}}{P}\right)^2\right] \\
\sigma^2_f &= f^2\left[\frac{P_{-1}+P_{+1}}{(P_{+1}-P_{-1})^2} + \frac{1}{P}\right]
\end{aligned} \tag{5.7}$$

The determination of the error in the extinction-to-backscatter ratio (1.24) from the extinction and backscatter quantities, whose error is now defined, is straightforward:

$$\sigma^2_\gamma = \left(\frac{\sigma^2_\alpha}{\alpha^2} + \frac{\sigma^2_\beta}{\beta^2}\right) \tag{5.8}$$

5.2 First PCL Aerosol Results

Several nights exhibiting interesting aerosol features, with a focus on high-altitude "layers", were selected and processed to extract aerosol measurements. These layers are thin, fairly uniform distributions of aerosols potentially comprised of smoke and soot from biomass burning, volcanic debris (primarily

sulfates), or cirrus clouds.

Grid plots (also referred to as colour or checkerboard plots) were created to display two-dimensional representations of the aerosol scattering, extinction and ratio measurements in both altitude and time. Averaged vertical profiles of scattering and extinction measurements, with the corresponding photocount error, were also created from photocount profiles summed in time.

The same scale is used for the colour plots as well as the mean profiles, in order to better compare results from different nights. The colour scale of the extinction plots is set to be 40 times that of the backscatter plots to allow easy comparison of the relative strength of the two. Clouds, with a typical extinction-to-backscatter around 20 sr (steradians) will appear higher on the colour scale in the backscatter plots, while smoke should appear stronger in the extinction plots (Winker, 2008).

A narrow value range is used to increase contrast and highlite some of the fine detail structure that is visible from the PCL measurements. The drawback to this is that some clipping does occur, mainly at the lower (dark blue) end of the colour scale. Faint aerosol signatures may be hidden in some of these dark blue regions.

In several of the colour plots there appear to be enhanced or depressed aerosol extinction-to-backscatter values along the upper and lower boundary of aerosol features. This is most likely an edge effect due to the manner in which backscatter and extinction measurements are gridded onto a common mesh in order to calculate the ratio, however particular care was exercised in handling this calculation. Due to the coarse 250 m Raman resolution, this can present problems for comparing the extinction to backscatter measurements for very thin aerosol features. This behaviour has been noted in other extinction-to-backscatter ratio measurements (Ansmann et al., 1992).

The first measurements, for the night of 2002-05-08 (Figure 5.2) are of an easily-recognized cloud feature. The mean value of all the extinction-to-backscatter ratio measurements is 25.7 ± 0.5 sr, with a standard deviation of 15 sr. There is notable structure in the ratio measurements, likely due to changes in the ice-water phase, particle size, shape and/or orientation. This represents a considerable deviation from the assumption of a single uniform extinction-to-backscatter ratio that is quite often assumed for continuous aerosol features and underscores the potential error with this approach. This same inner-cloud structure has been observed in previous Raman-Lidar aerosol studies (Ansmann et al., 1992).

As the cloud passes by, the Lidar takes vertical measurements through the cloud. By plotting these measurements side-by-side in time and altitude and assuming the cloud's speed of passage to be constant, the plot can be taken to represent a long, vertical slice through the cloud (Figure 5.2). For this reason, many clouds show aerosol features in the data that closely resemble visually-observed cloud shapes and structures (Figure 5.2).

The backscatter plots for the next night, 2000-08-17, depict (Figure 5.4) what very much appears to be a diffuse smoky layer at 8 km with small clouds above it. The extinction-to-backscatter ratio supports this hypothesis with striking contrast. The smoke region is measured to have a mean extinction-to-backscatter ratio of 64 ± 2 sr, significantly above the range observed for cirrus clouds (Chen et al., 2002). The cloud region has a ratio of 18.2 ± 0.5 sr, which is typical of clouds (Table 1.1).

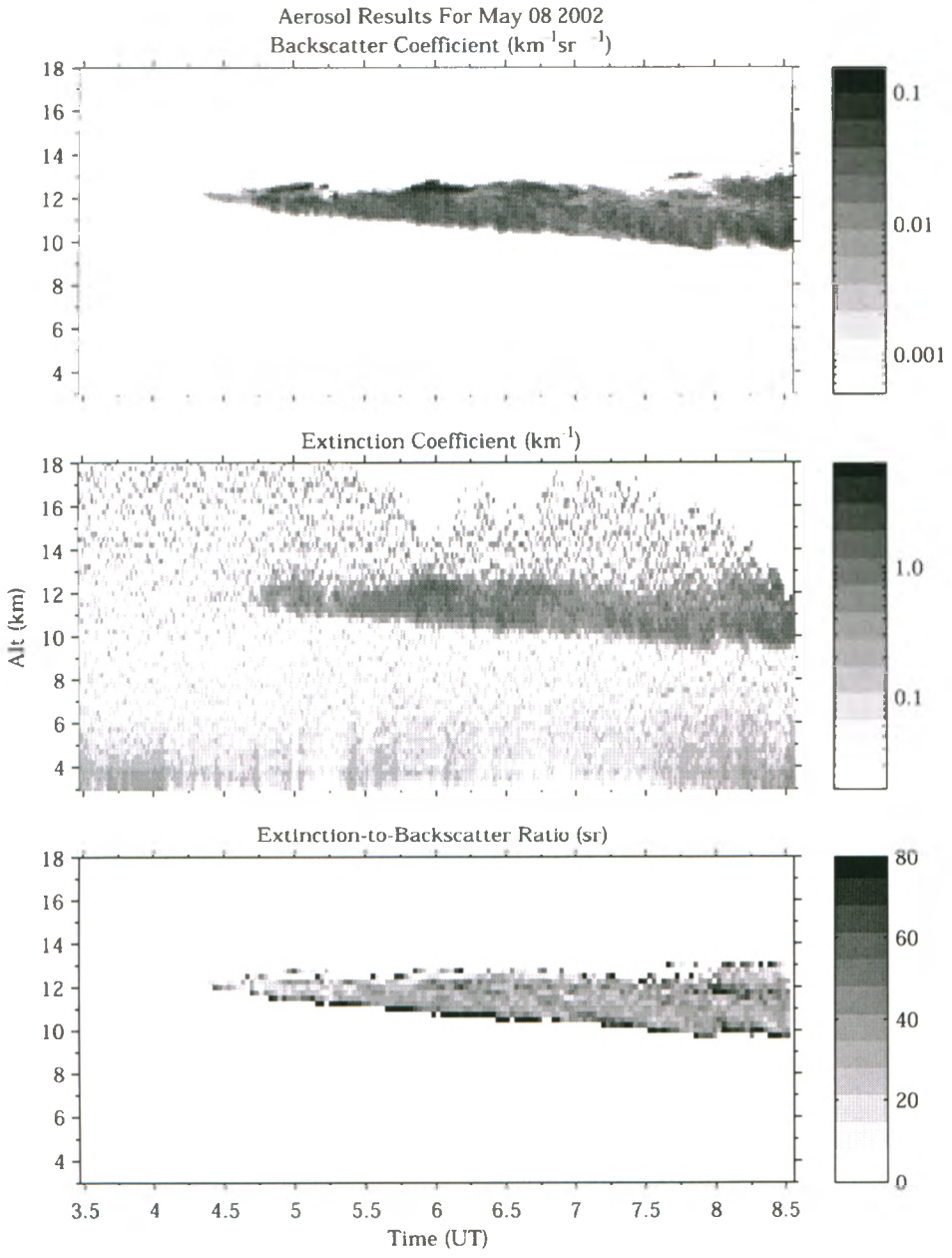

Figure 5.2: From top to bottom: grid plot of the aerosol backscatter, extinction and E-to-B ratio. A broad, 4 km-thick, Cirrostratus-like cloud is visible at 13 km. Ratio indicative of structure in different particle properties. A colour version available in Appendix B.

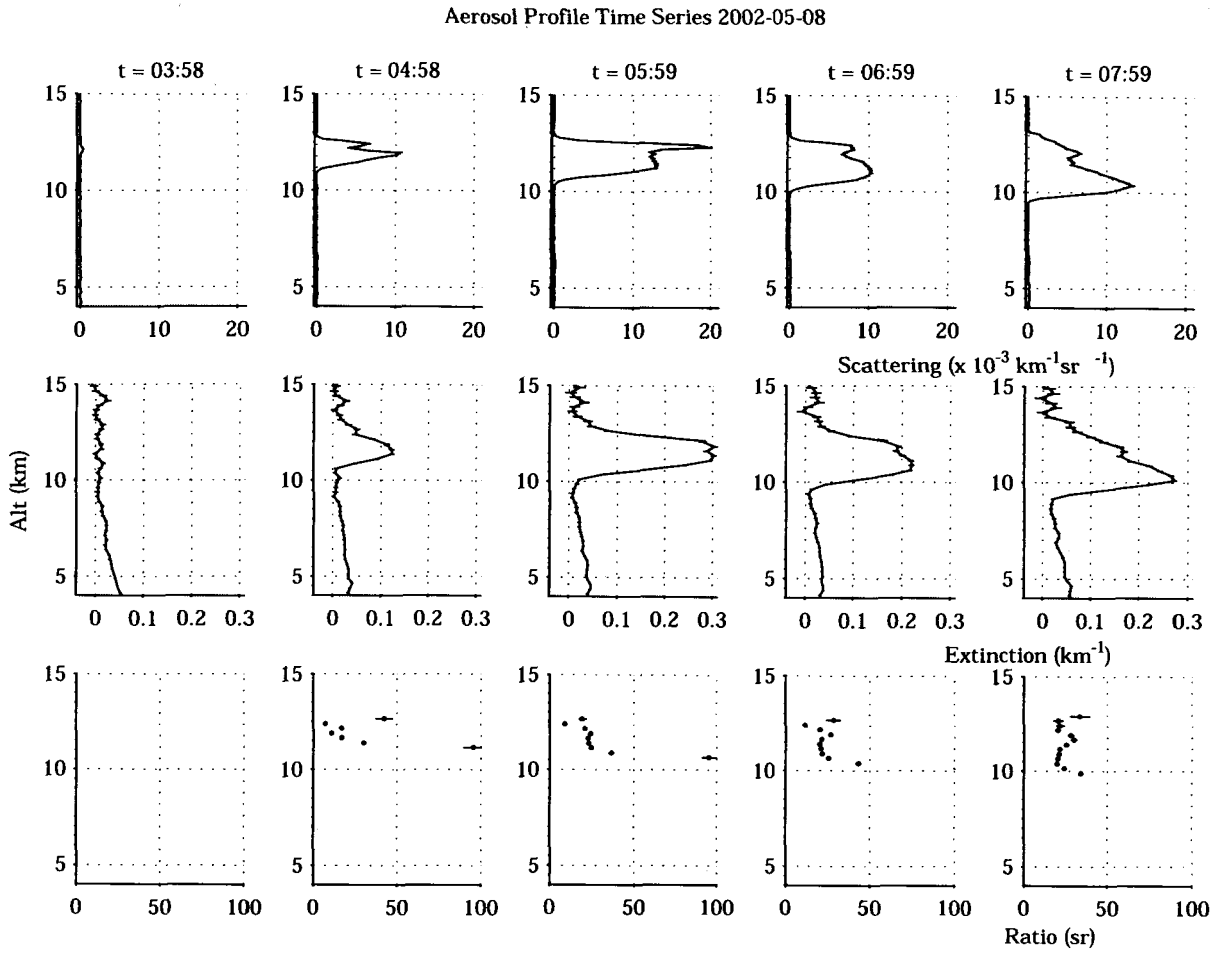

Figure 5.3: Multiple snapshots showing the evolution of aerosol measurements in time for an encroaching cloud. Averaged photocount profiles every hour (centered at indicated time) are used to calculate the aerosol backscatter (1.18) and extinction (1.23). The extinction-to-backscatter ratio, an intrinsic quantity sensitive to aerosol characteristics, is found by dividing the aerosol extinction by the backscatter. Decreased extinction-to-backscatter ratio values at $t = 4:58$ of around 12 sr suggest different particle properties in the cloud tip compared with the rest of the cloud (around 22 sr). Outliers present due to edge effects in ratio calculation

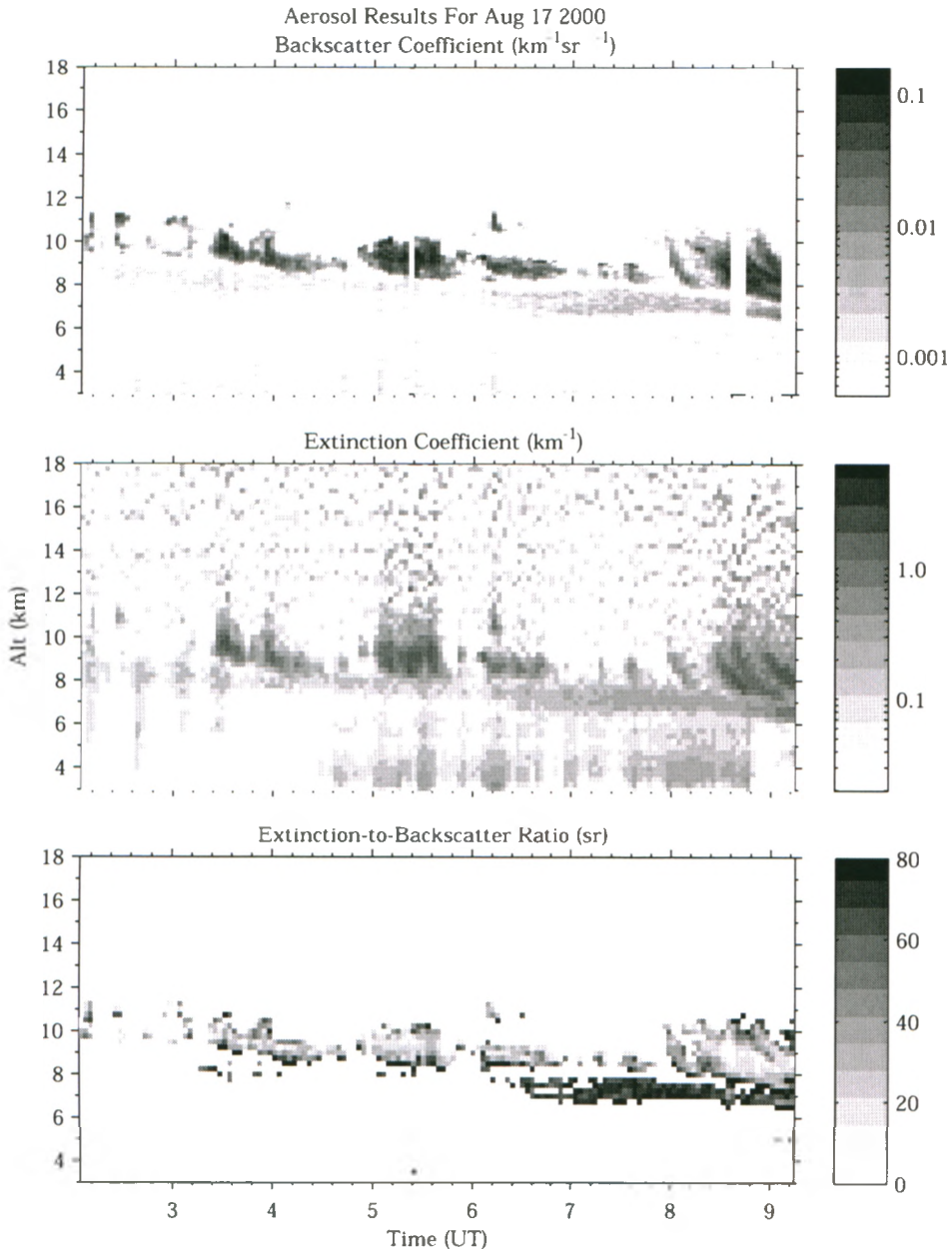

Figure 5.4: Small, puffy clouds above distinct, diffuse smoke layer. Ability of E-to-B ratio to disambiguate smoke ($\bar{\mu} = 64 \pm 2$ sr, $\sigma = 18$ sr) and clouds ($\bar{\mu} = 18.2 \pm 0.5$ sr $\sigma = 9$ sr) is demonstrated. A colour version of this figure is available in Appendix B.

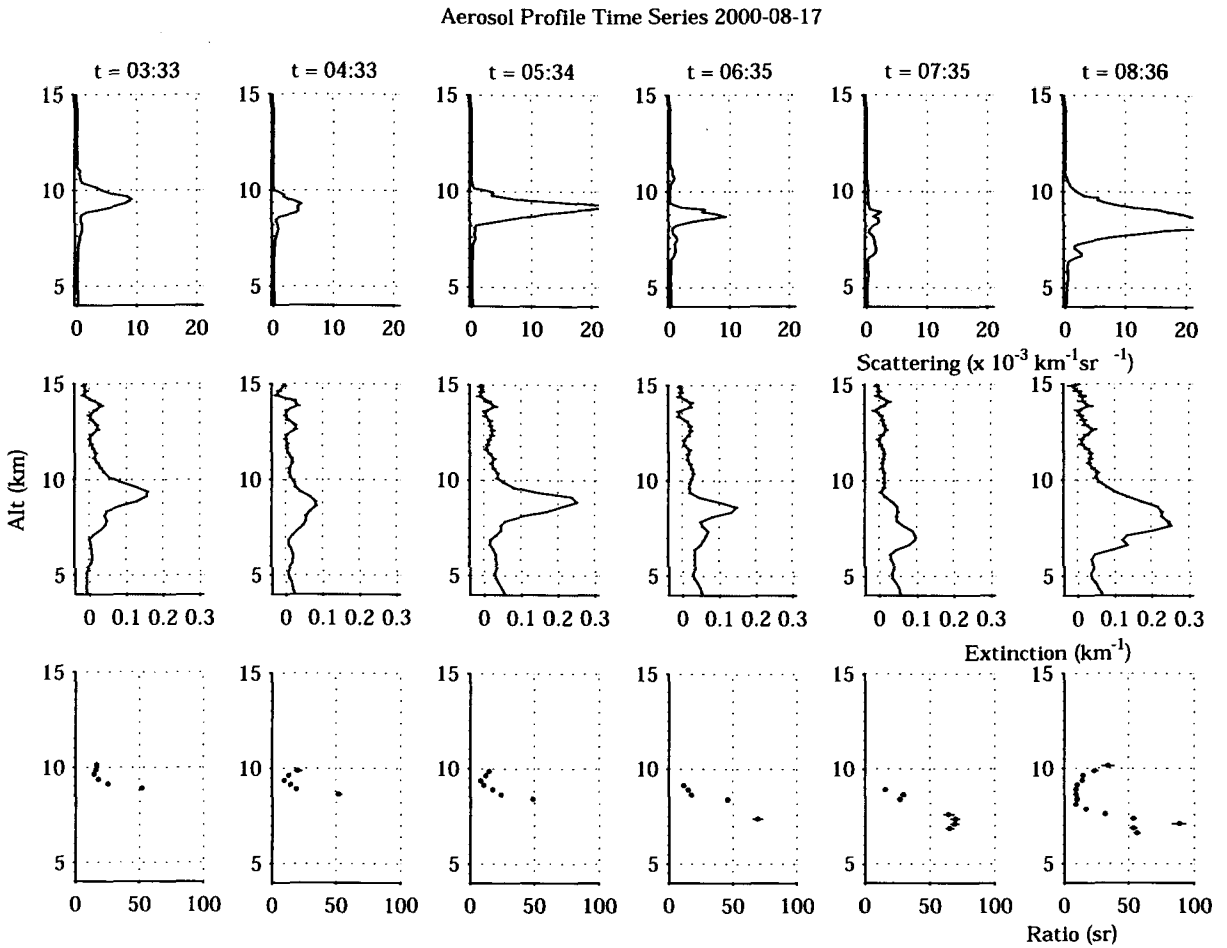

Figure 5.5: Hourly plots showing sparse clouds above descending smoke layer. Distinct aerosol regions are much easier to identify in colour plot than in these one-dimensional time slices

5.3 Summer of Fire

The summer of 2002 was a particularly virulent season for forest fires, a number of which were observed to blow up into violent pyro-cumulonimbus (PyroCB) events (Knapp et al., 2005), (Jost et al., 2004). Features were also observed in the raw photocount data that looked suspiciously like smoke layers almost continuously every night in June and July. Several of these features appeared at high altitudes: approaching and possibly penetrating the stratosphere. These nights were processed for aerosols (Figures 5.6 to 5.13). Colour versions of these plots are provided in Appendix B.

The first of these high-altitude smoke layer candidates, from the night of 2002-06-21 (Figure 5.6) shows particularly interesting behaviour. A thin region of strongly-scattering aerosols (backscatter above 0.1 km^{-1} sr^{-1}) at 13.5 km lies embedded within a diffuse layer. From the grid plot, the extinction-to-backscatter ratio in the bright inner region can be seen to be around 20 sr. The outside region appears to have an enhanced extinction-to-backscatter ratio, however it is difficult to get an accurate reading due to probable edge effects.

There is a faint aerosol signature between 11.5 and 13 km visible in the mean profile (Figure 5.7), followed by an abrupt increase at 12.81 km in the scattering data and at 12.62 km in the extinction data. This is taken to be an interface dividing two distinct upper and lower regions in the feature. The extinction-to-backscatter ratio is estimated by taking the total amount of extinction in the feature in each portion of the feature and dividing it by the total amount of scattering. This produces values of 38 ± 5 in the upper region and 75 ± 30 below, suggesting distinctive compositions.

Based on the extinction-to-backscatter ratio values, the lower region is consistent with a small quantity of dry smoke, while the upper region is in-

terpreted to be a smoky region with entrained water/ice. This water/ice may have originated from the origin site of the smoke, or resulted from nucleation of surrounding environment.

Further dry, smoky layers are apparent for 2002-06-29 (Figure 5.8) and 2002-06-30 (Figure 5.10) – as suspected by the diffuse shape of the backscatter returns, and supported strongly by the high extinction-to-backscatter ratio of 84 ± 5 sr (Figure 5.9) and 66 ± 5 sr (Figure 5.11).

Very faint traces of a thin backscatter features are present on 2002-07-03 (Figure 5.12) and 2002-07-05 (Figure 5.13). The mean backscatter profiles for these nights peak at just 4×10^{-4} km^{-1} sr $^{-1}$ and 1×10^{-4} km^{-1} sr $^{-1}$, respectively, and extend across 14.08-14.32 km and 14.8-14.92 km. Backward trajectory analysis traces the air parcels from these nights to different suspected PyroCB events, however it is not possible at present to characterize the aerosols beyond their thin, faint appearance due to the weak extinction below the detection threshold. No high-altitude aerosols were observed on 2002-07-04.

A comparison of the maximum altitude of the measured aerosols with the tropopause height measured by Detroit radiosonde shows these aerosol features to be near or above the tropopause (Figure 5.14).

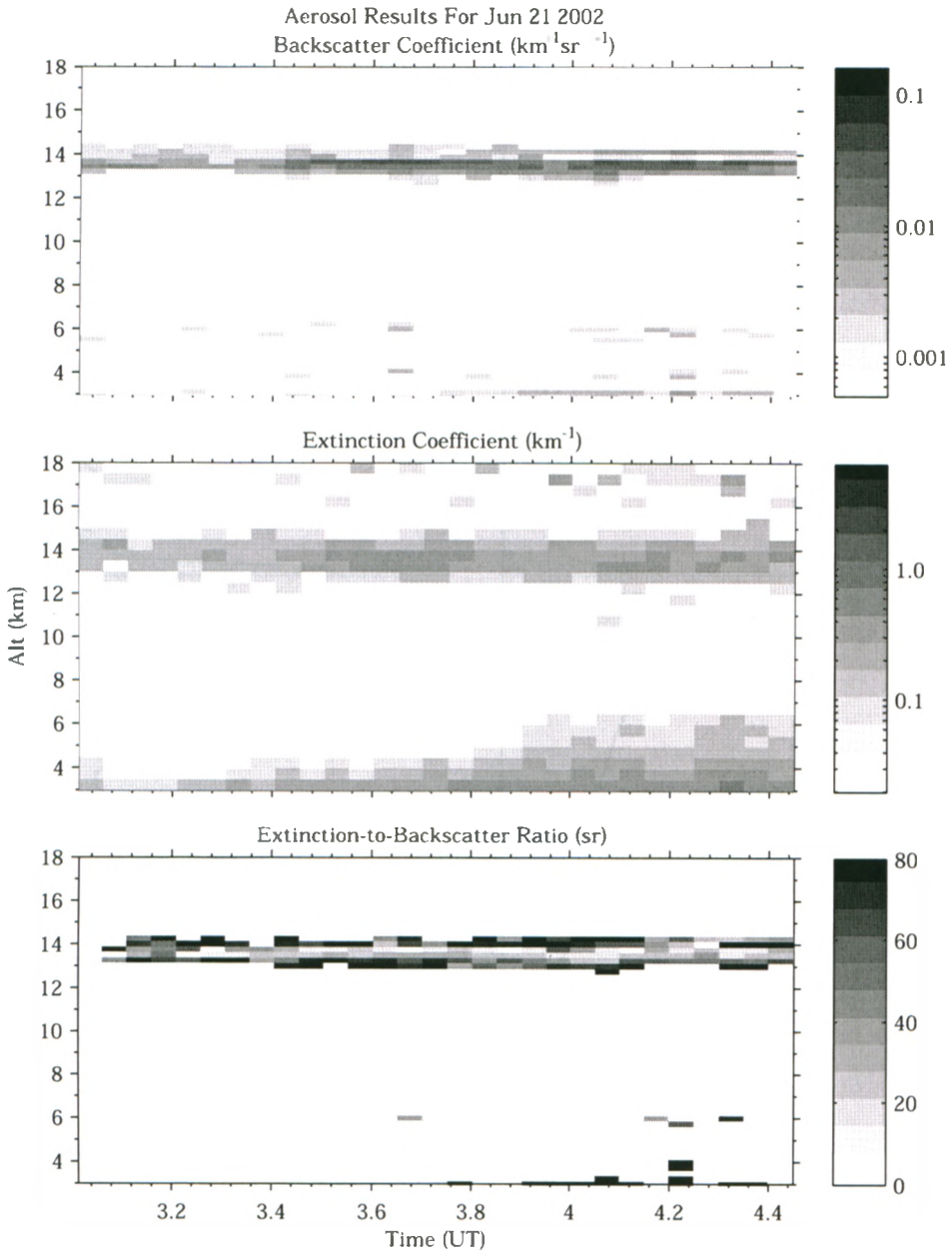

Figure 5.6: Layer feature of high E-to-B ratio with strongly scattering region embedded inside. Interpreted as smoke with entrained water/ice. Some noisy but detectable measurements are present below the colour range of the plots (refer to mean profile plot).

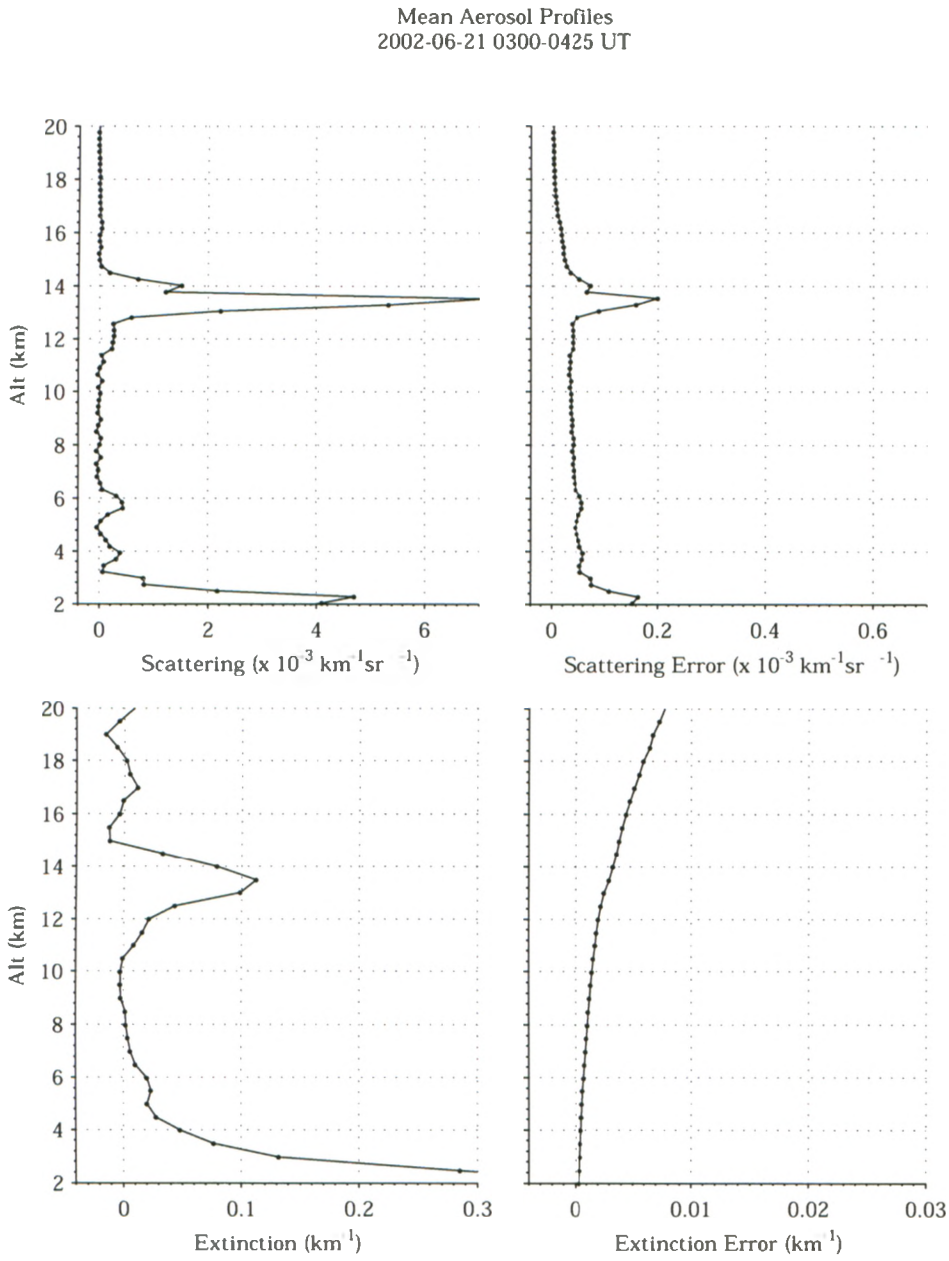

Figure 5.7: A strongly-scattering layer at 13 km above a faint but distinct region at 12 km. Ratio between 13 and 14.5 km is 38 ± 5 sr (dirty cloud), 12 and 13 km 75 ± 30 sr (smoke). The error shown is from Poisson photocount statistics (Section 5.1).

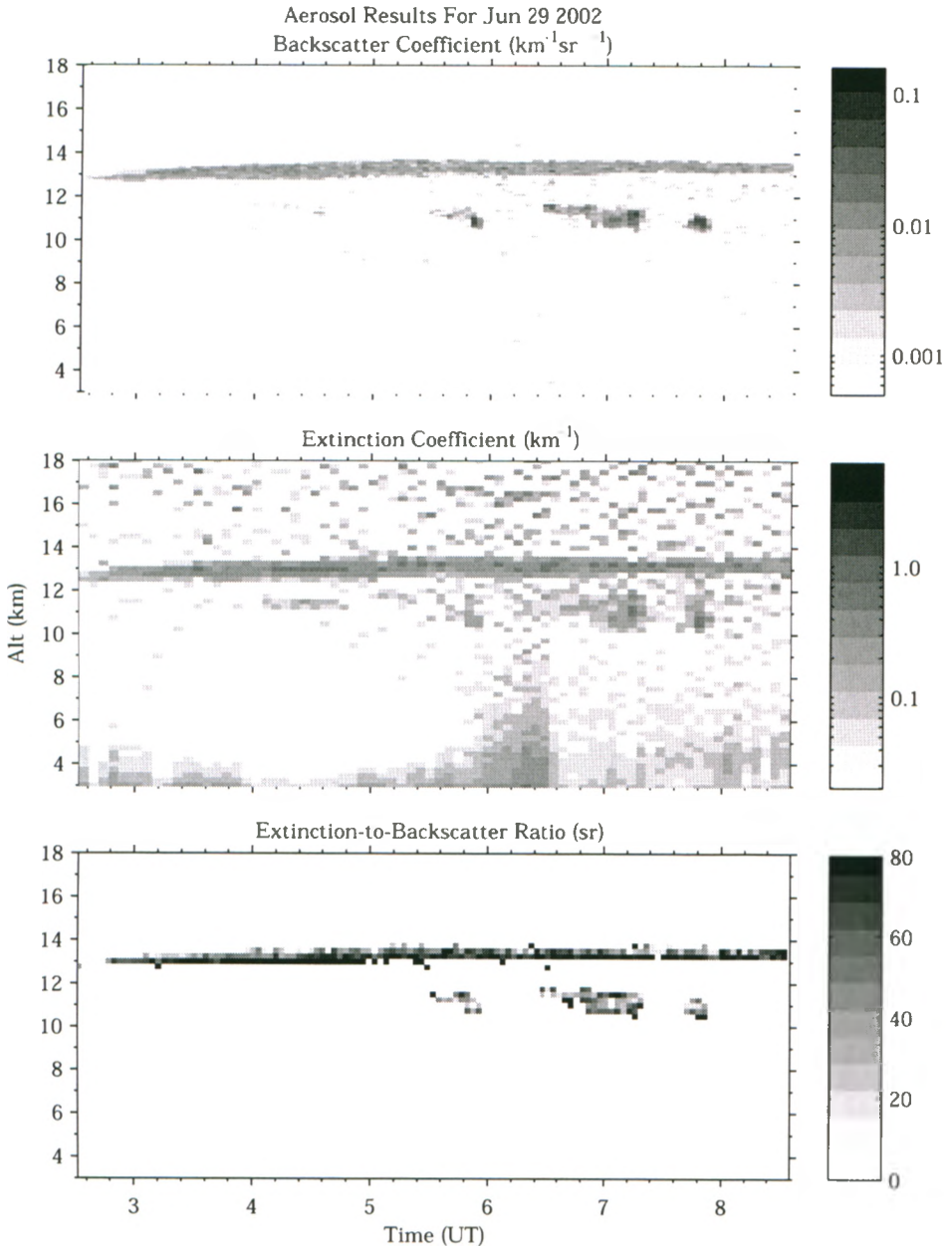

Figure 5.8: Prominent layer feature topping at 13.5 km. Fairly diffuse with relatively strong extinction. Ratio is high, but calculation at edges is inconsistent – problematic due to narrow extent.

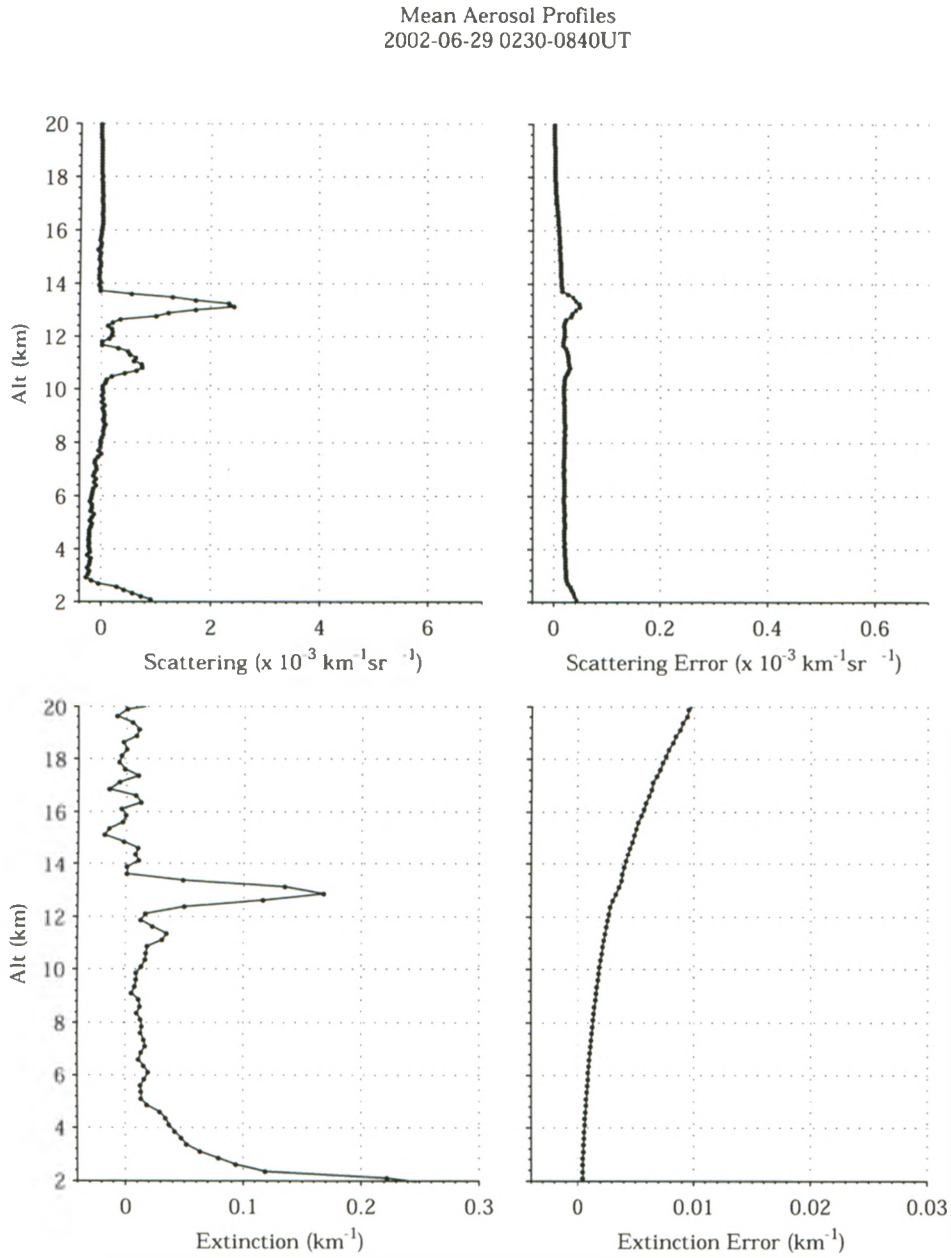

Figure 5.9: Shutter error below 8 km in backscatter data. There are aerosols below 5 km, but the readings are not very reliable due to variation in the overlap function. Average Ratio of the layer between 12 and 14 km is 84 ± 5 sr (smoke).

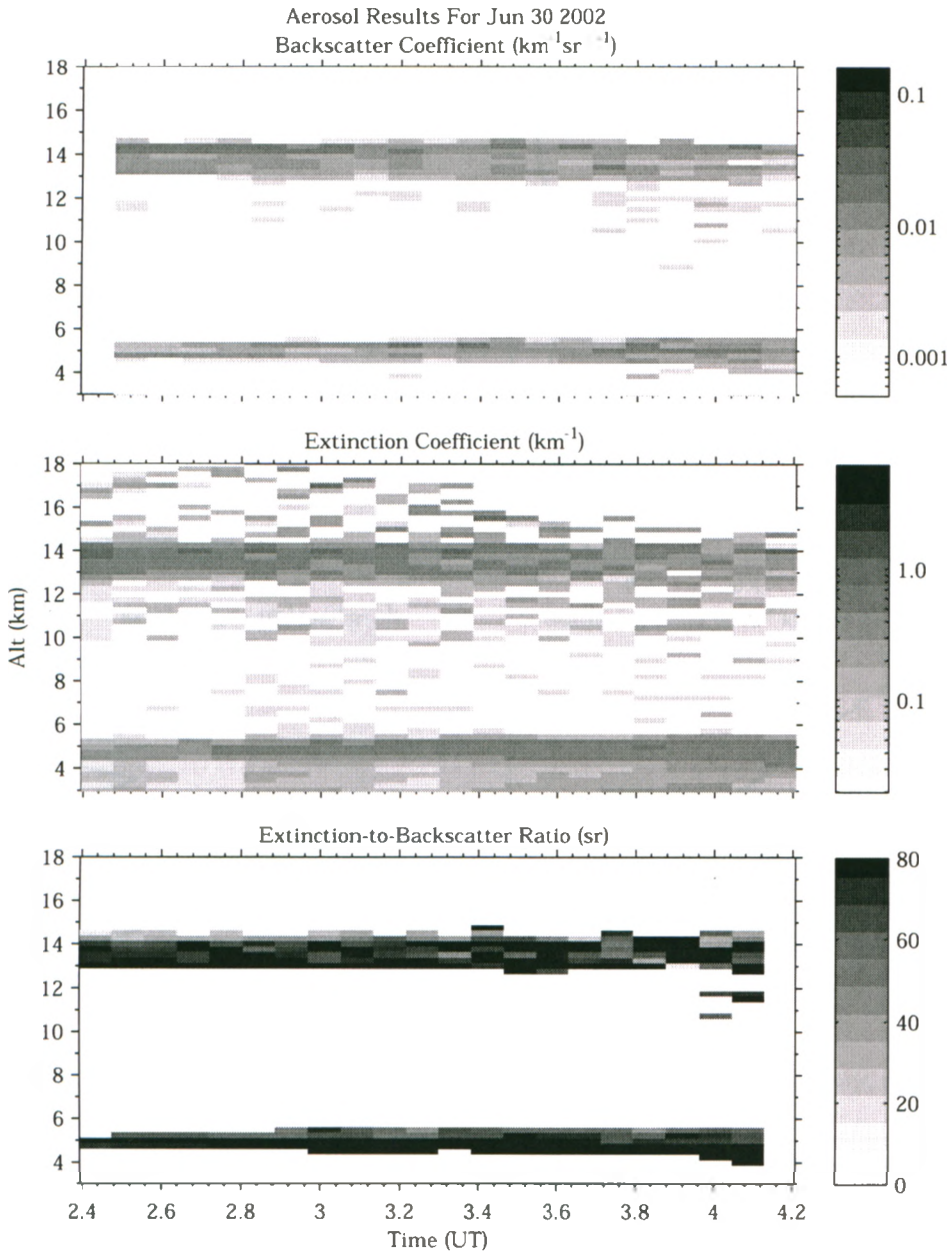

Figure 5.10: Fairly bright layer feature with even stronger extinction. Almost certainly smoke. Distinct bright upper portion above dimmer lower section, with sharp boundary at 12.5 km.

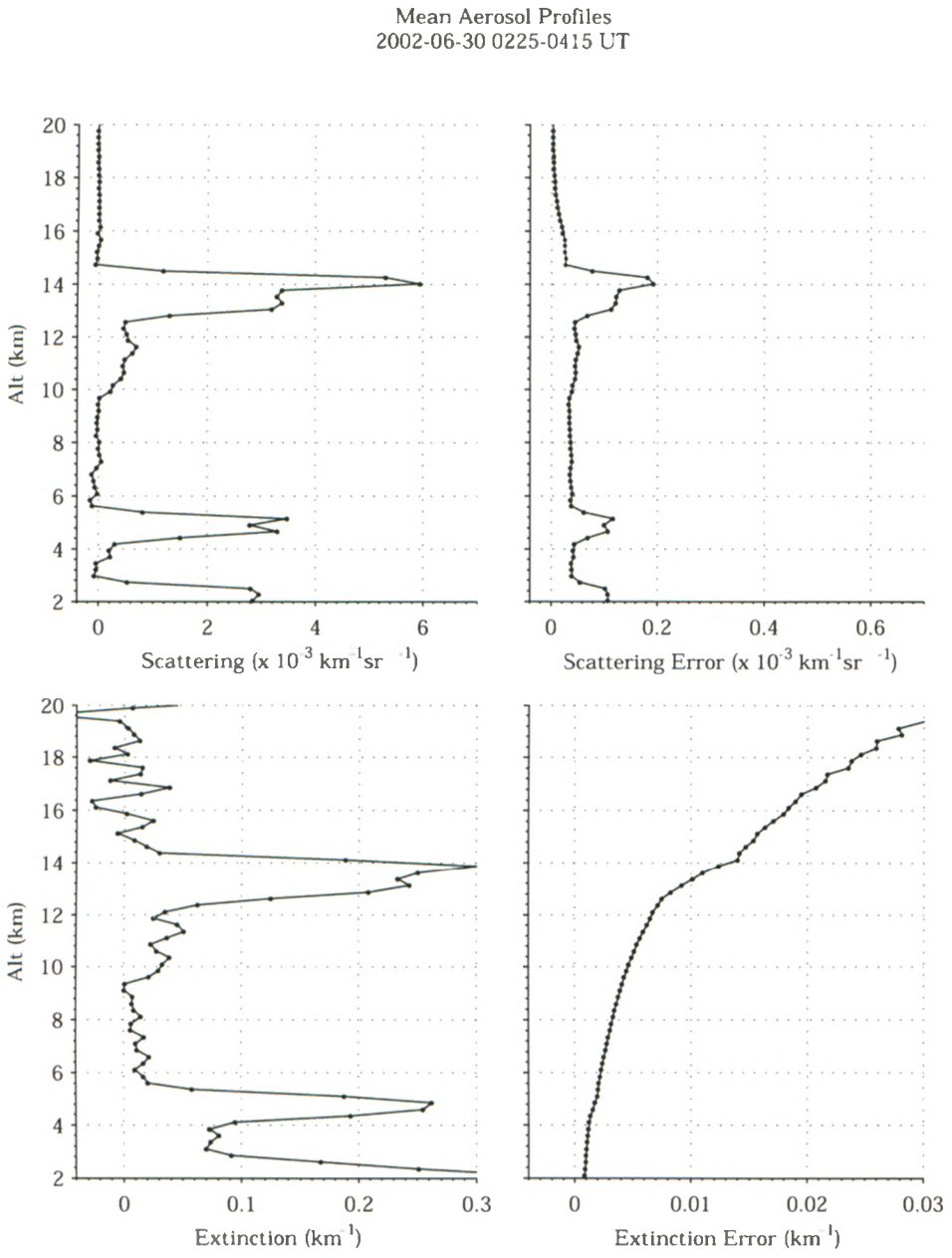

Figure 5.11: Two distinct, fairly uniform lower (10-12.5 km) and upper (12.5-14.5 km) sections comprising layer. Optical properties similar – lower section ratio: 77 ± 15 sr, upper: 66 ± 5 sr – suggesting the same smoky material in both regions, but occurring with different concentrations.

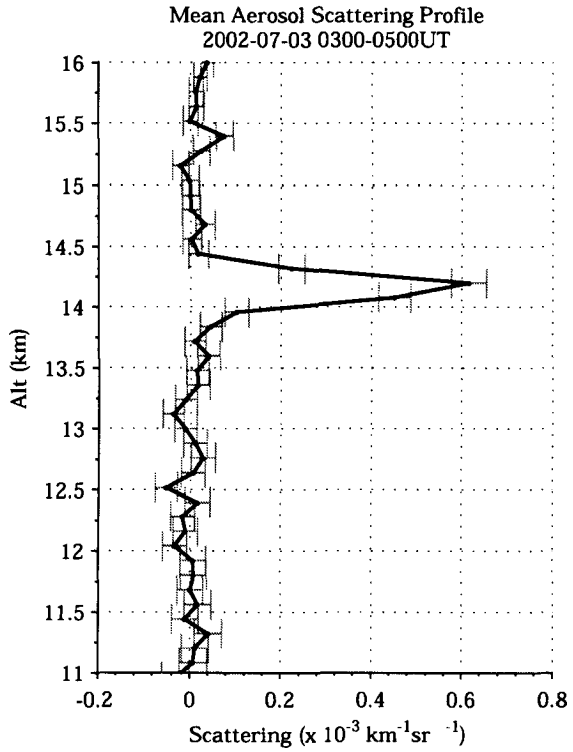

Figure 5.12: Faint backscatter signal measured at 14.25 km on 2002-07-03.

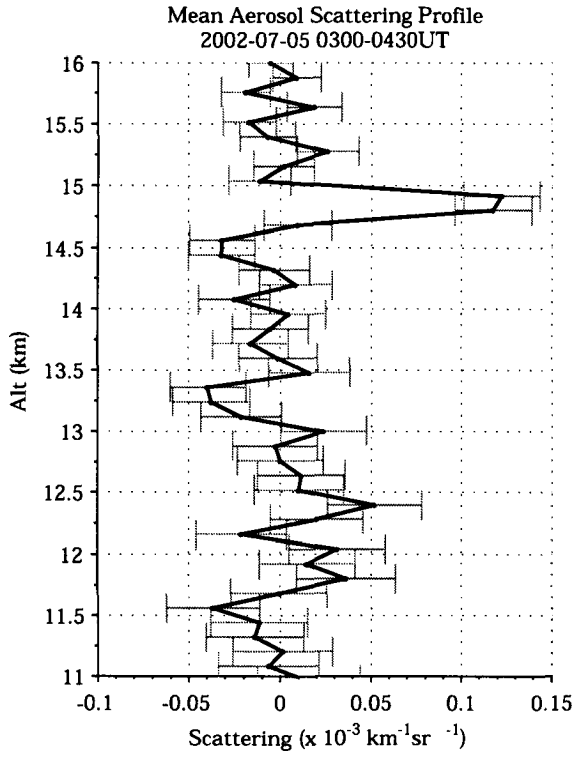

Figure 5.13: Faint backscatter signal measured at 14.75 km on 2002-07-05.

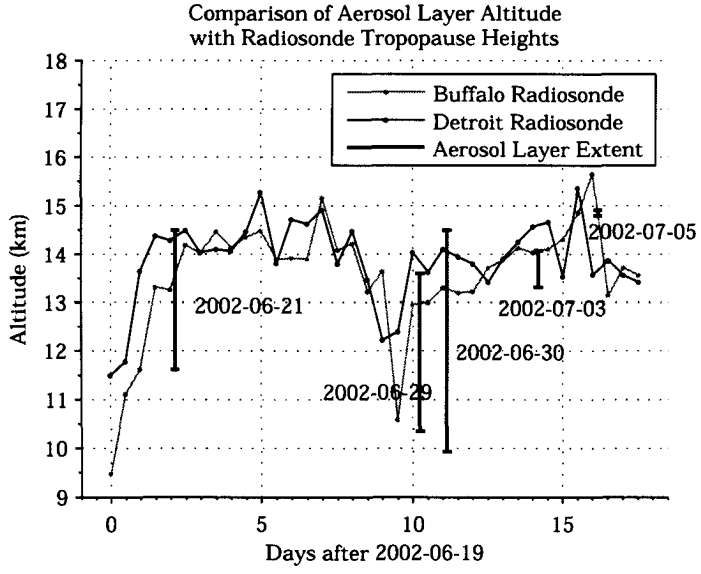

Figure 5.14: Comparison of PCL aerosol extents and tropopause heights measured by radiosonde.

5.4 Negative Smoke Results

Like many of the observations consistent with lofted smoke (Figure 5.6 to Figure 5.10), the night of 2007-05-23 has a broad, diffuse feature present in the aerosol backscatter (Figure 5.15). When the raw, uncalibrated elastic backscatter signals were first examined, this night was believed to be a strong candidate for a smoke layer.

Once the PCL aerosol calibration and measurement technique was applied to this night, however, the aerosol extinction was found to be relatively weak (Figure 5.16). The resulting extinction-to-backscatter ratio was $15 \pm 1 (\sigma = 5)$ sr, which is typical of cloud. This is slightly lower than the Calipso reference value for ice clouds (22 sr), probably due to an error from the tropopause height in the radiosonde density used.

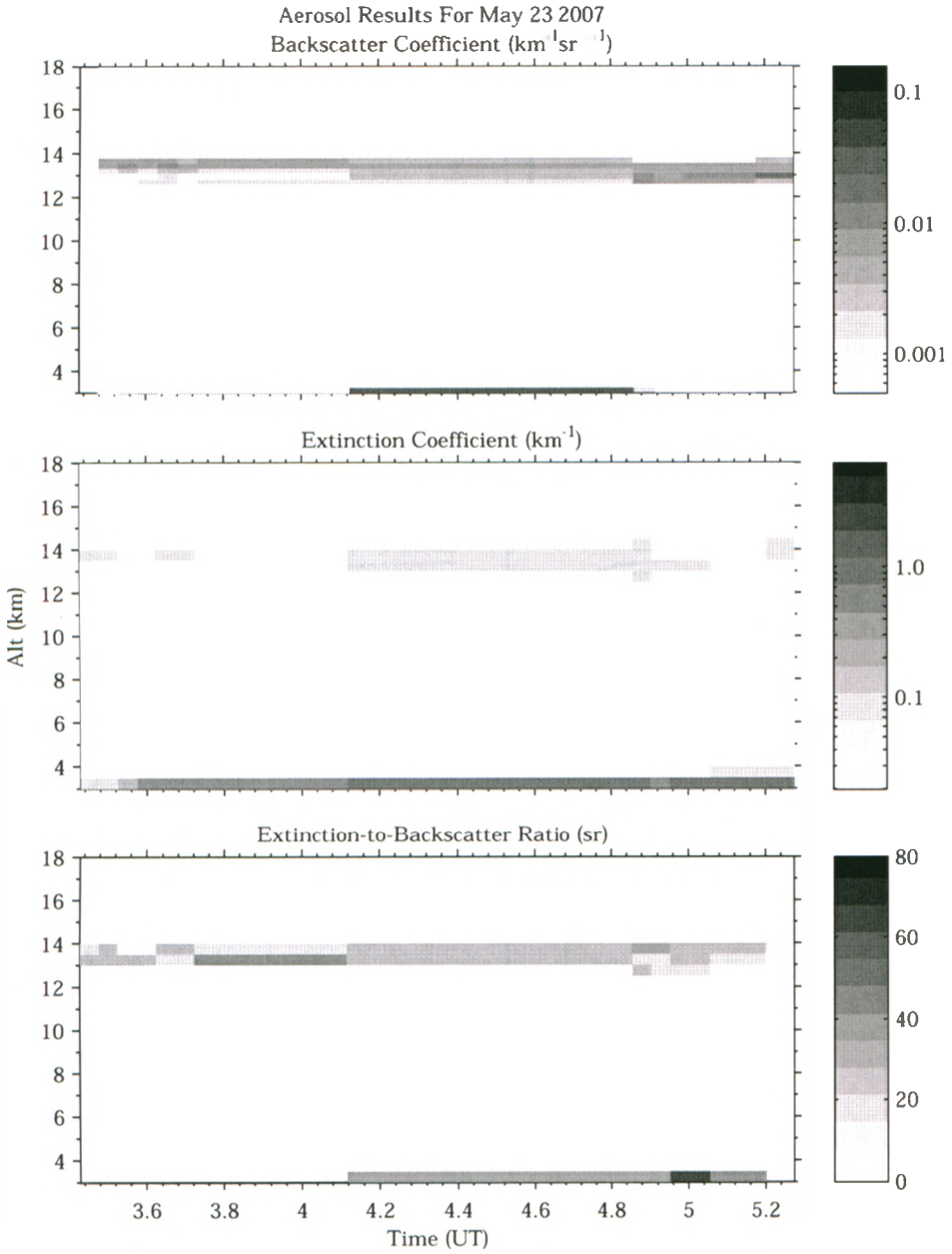

Figure 5.15: Thin, extended, diffuse, high-altitude layer that was a strong candidate for smoke based on the backscatter data. Low extinction measurements and corresponding ratio, however, successfully resolved this as a thin cirrus cloud.

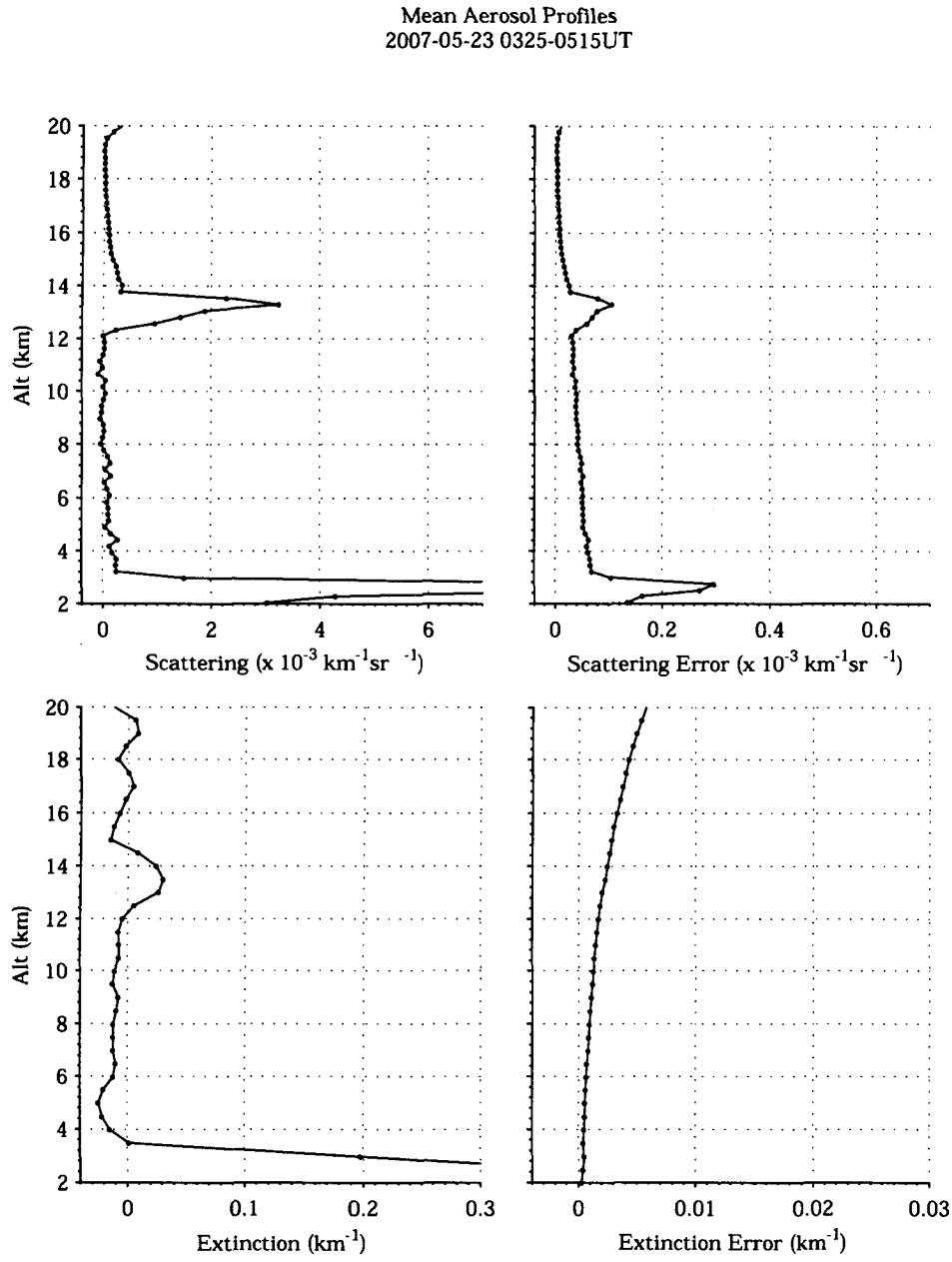

Figure 5.16: Cloud. Mirror-overlap behaviour slightly different from reference nights, resulting in extinction error (negative values) toward lower altitudes. Ratio measured to be 17 ± 2 sr, which may be slightly underestimated (ice clouds are typically closer to 25 sr).

5.5 Kasatochi Volcanic Eruption, August 2007

On August 7th 2007, the volcano Kasatochi (52.18 deg N, 175.51 deg W) erupted with considerable force, ejecting debris high into the air (Fromm et al., 2008), (Westphal et al., 2008). Nearly three weeks later, during system testing of the Purple Crow Lidar on the night of August 26th, distinct aerosol signatures were observed at 17.5 and 19 km, well into the stratosphere (Figure 5.17). On this day, the Lidar was operated in a non-standard mode. The results in Figure 5.17 were collected without the use of the shutter (it was set to 1 km) over a mere 15 minutes. The laser power was lowered to compensate for the lack of shutter so as not to saturate the elastic signal detectors (the fainter Raman channel measurements were collected over a slightly longer 30 minute period after the shutter was re-activated and the laser power increased). The peak backscatter signals at 19 km and 17.5 km were $(1.5 \pm 0.2) \times 10^{-4}$ km^{-1} sr $^{-1}$ and $(0.8 \pm 0.1) \times 10^{-4}$ km^{-1} sr $^{-1}$, respectively.

The calibrated aerosol measurements demonstrate the capability of the PCL to make detailed aerosol measurements at high altitude with high resolution compared with other Lidar systems, due to its high power-aperture product. Extinction measurements are unfortunately unavailable due to the limited amount of data collected, and the very low peak laser power available at the time due to Lidar repairs. While stratospheric aerosols are well known to result from volcanic activity, detailed extinction measurements would permit useful optical characterization of the volcanic smoke, ash and/or sulphate products, potentially measuring the evolution of these aerosols over multiple nights.

Many commercial aircraft pilot reports were made of high-altitude ash over North America in the coming weeks and stratospheric aerosol enhancement was

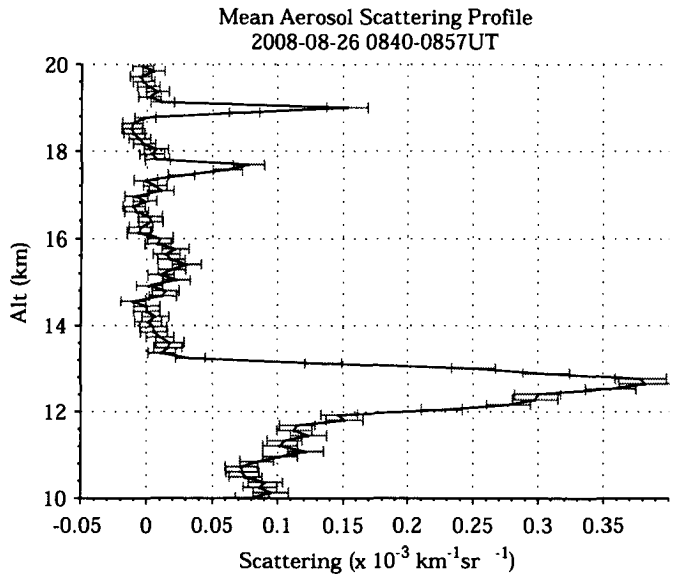

Figure 5.17: PCL measurements of aerosols well within the stratosphere at 17.5 and 19 km following the Kasatochi volcanic eruption. These measurements were taken during special operations of the Lidar without the shutter over a 15 minute window.

visible by the Calipso Lidar for a month following the eruption (Fromm et al., 2008).

The closest Calipso measurements to the PCL readings occurred a day later several hundred kilometers west of the PCL (Figure 5.18). The altitude of the aerosols are in agreement but the strength of the backscatter measured by Calipso is an order of magnitude higher than PCL. This is likely due to differences in the time and space of the data collection as well as the the brevity of the PCL measurements.

5.6 Coincident PCL-Calipso Measurements

The night of 2007-05-05 saw a very fortuitous overpass of Calipso satellite. At 7:35UT, the Calipso measurement track came within 2 km of the PCL (Figure 5.20), while the PCL was in operation. That night, the PCL took

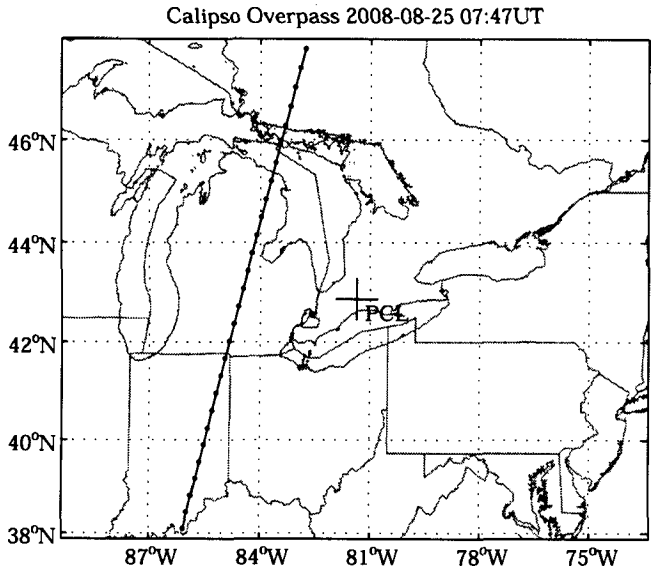

Figure 5.18: Map showing location of Calipso measurements in the vicinity of the PCL.

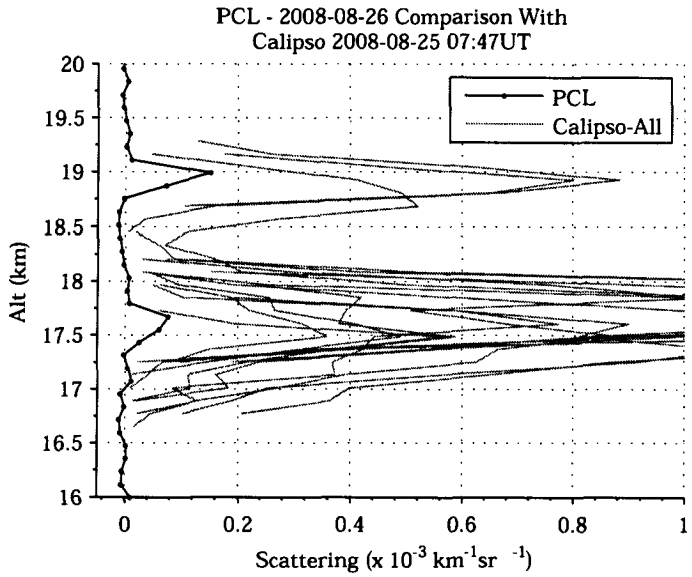

Figure 5.19: Comparison of PCL and Calipso measurements. Calipso data are from previous day. While matching in altitude, the PCL measurements are nearly an order of magnitude below Calipso.

measurements between 0700 and 0930UT, and saw fairly consistent backscatter from a faint, uniform cloud layer over the two and a half hours of data collection. On the basis of the consistent observations, the Calipso measurements are taken to be reasonable comparisons despite the slightly different locations.

PCL backscatter measurements were calculated between 7:25UT and 7:45UT and compared with the average aerosol backscatter measured by Calipso within 9 arc minutes of latitude and longitude from the PCL site (Figure 5.21). The result shows a very good agreement between the two measurements.

The Calipso data are excellent means of validating the PCL backscatter measurements, since they are made using the same 532 nm Lidar approach, as opposed to having to be derived from some other type of instrument with a priori assumptions. The only drawback is, of course, the lack of exact spatial concurrency in the measurements compared with co-located instruments.

It is fairly typical for Calipso to pass within a few hundred kilometers of the PCL, often allowing comparison with PCL results on a descriptive level, however this is the only night where the measurements are sufficiently close and the conditions uniform enough that the measurements can be taken to be nearly coincidental.

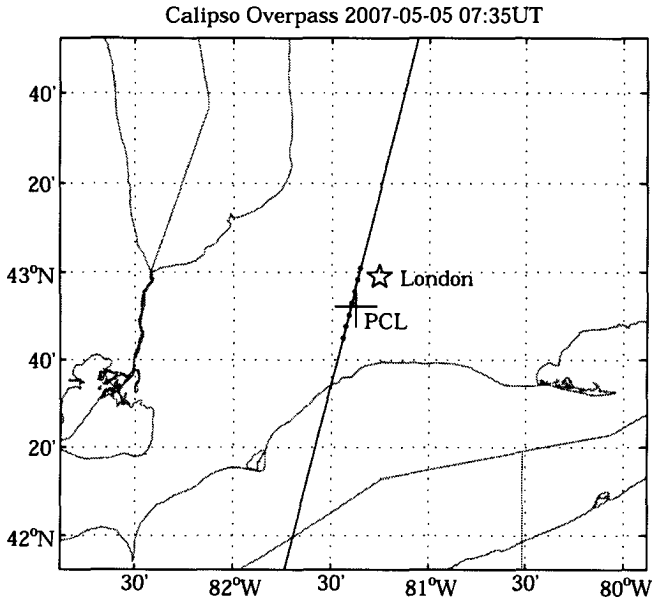

Figure 5.20: Map of 7 averaged Calipso measurements used for PCL comparison taken at 2007-05-05 7:35UT. The nearest point is 2 km from the PCL site.

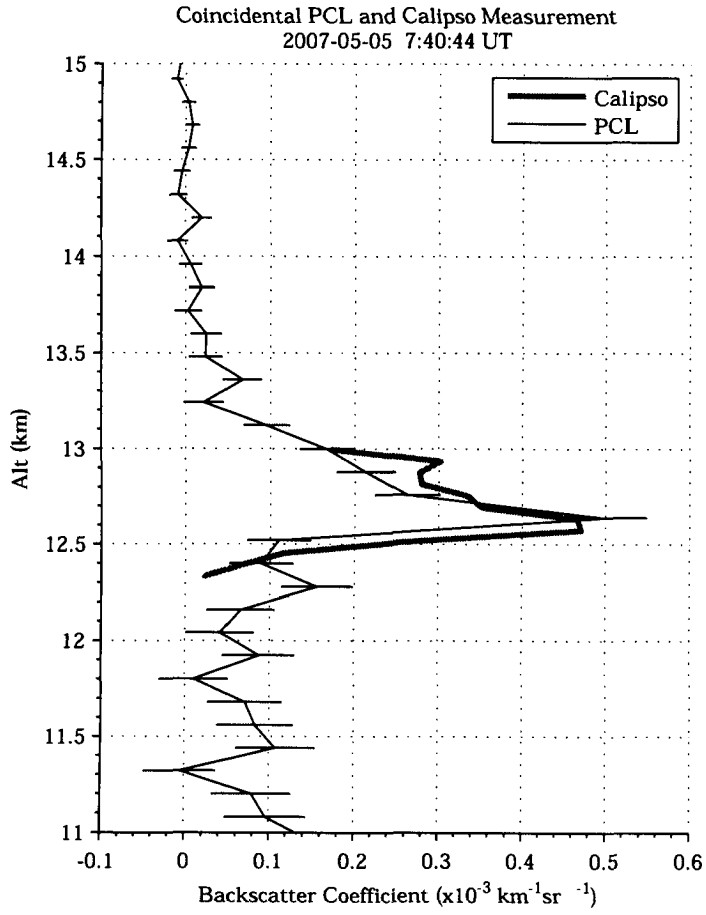

Figure 5.21: Comparison of coincidental PCL and Calipso measurements. The agreement in the measured backscatter is very good.

Chapter 6

Conclusions

A complete method has been developed and applied for extracting aerosol backscatter and extinction measurements from the existing PCL data set. This included measuring the overlap function as well as measuring the behaviour of the low-altitude shutter.

It was initially believed that up to 7 out of 300 nights of usable PCL data might contain smoke features near the tropopause. This was derived from qualitative examination of the raw, uncorrected, shutter-influenced elastic backscatter signal plotted as two-dimensional grid plots in altitude and time (Cloud plots) for diffuse, uniform signals above 12.5 km Section 4. Using the aerosol technique and by examining the extinction-to-backscatter ratio, two were found to be clouds – 2007-05-23 and 2002-07-05. Three nights were consistent with higher extinction-to-backscatter ratios (and therefore likely smoke) – 2002-06-21, 2002-06-29, 2002-06-30. The features in the remaining two nights weren't strong enough to extract aerosol extinction measurements – 2002-07-03 and 2002-07-05.

The extinction measurements are influenced significantly by the overlap

function below around 8 km. The error in the measured overlap profile due to background aerosols, as well as the variability of the liquid mirror rotation speed (gradually over time and also during the course of a given night) leads to considerable uncertainty in the extinction, so measurements below 8 km must be carefully interpreted.

The scatter measurements are sensitive to the shutter function, making accurate determination essential. There is a significant change in the slope of the shutter function that occurs around 12 km, so a miscalculation can result in a large error in the backscatter values in this region. The key to accurate measurements here is to obtain accurate reference shutter profiles, which are a direct function of the set full-aperture shutter altitude setting (and possibly affected by other alterations inside the detector box), and to properly match up the shutter behaviour on the night under consideration to one of the reference profiles.

For ongoing Lidar observations, accurate aerosol measurements are contingent on the following practices:

1. Proper vertical laser alignment
2. Consistent mirror speed and optical alignment
3. Accurate characterization of system overlap and shutter behaviour that matches a known reference profile

There are significant new avenues for research now possible with these new aerosol measurements. Detailed analysis of some case studies of cirrus cloud structures and the inferred physical properties can now be performed with close comparison with laboratory studies. This would provide a useful starting point as these results can be compared to similar studies (Ansmann

et al., 1992). This can then be extended to a micro-physical study of the high-altitude smoke layers, based largely on the aerosol ratio measurements, as such an analysis of smoke based on Raman-Lidar observations is believed not to exist.

Another extremely promising application of these aerosol measurements is toward correcting transmission profiles during aerosol-laden nights and permitting accurate temperature and water vapour retrievals around and within clouds and other aerosols. This would greatly expand the conditions under which the Lidar could be usefully operated – which at present is more or less limited to clear conditions.

There are many ways in which to expand and improve upon the aerosol measurements. Some of these can be accomplished through further analysis of the existing data, while the greatest improvements can be made through additions to the Lidar system

1. Improved calculation of overlap function with aerosol data, possibly by using a borrowed co-located Lidar system with well-known near-field behaviour.

2. Measuring and modeling overlap as a function of mirror period.

3. More sophisticated data filtering / smoothing

4. Application of multiple scattering correction to permit accurate measurements in strongly-scattering clouds.

5. Addition of Rayleigh detection channel with no shutter (may require several to account for dynamic signal range). This is an extremely important addition to improving the quality of the backscatter measurements in order to remove the variability of the shutter.

6. Addition of second Rayleigh wavelength to improve aerosol characterization (355 nm or possibly 1064 nm would probably be the easiest to implement). This would allow for determination of the Angstrom Coefficient - the wavelength dependency of the extinction coefficient.

7. Addition of ground pressure sensor to improve determination of atmospheric density. This would reduce systematic error in aerosol backscatter measurements at all altitudes, and aerosol extinction measurements close to the ground.

8. Addition of a second co-located fixed-mirror Rayleigh-Lidar system (possibly an "off the shelf" model) to improve near-field retrievals by the liquid-mirror telescope system. This would greatly enhance the quality of the aerosol measurements at lower altitudes by removing the variability of the mirror focus.

As a result of this work, the Purple Crow Lidar is able to make consistent measurements of aerosols in the upper troposphere in much higher resolution than most other aerosol Lidars. Through further work and possible upgrades, the capabilities of the PCL can be extended to lower altitudes and fainter aerosols while still leveraging the high power of the rotating liquid mercury telescope.

Appendix A

Additional Figures

Several additional figures have been included in this section for completeness. These have been placed here rather than in the body of this text to increase legibility due to the large number of figures used.

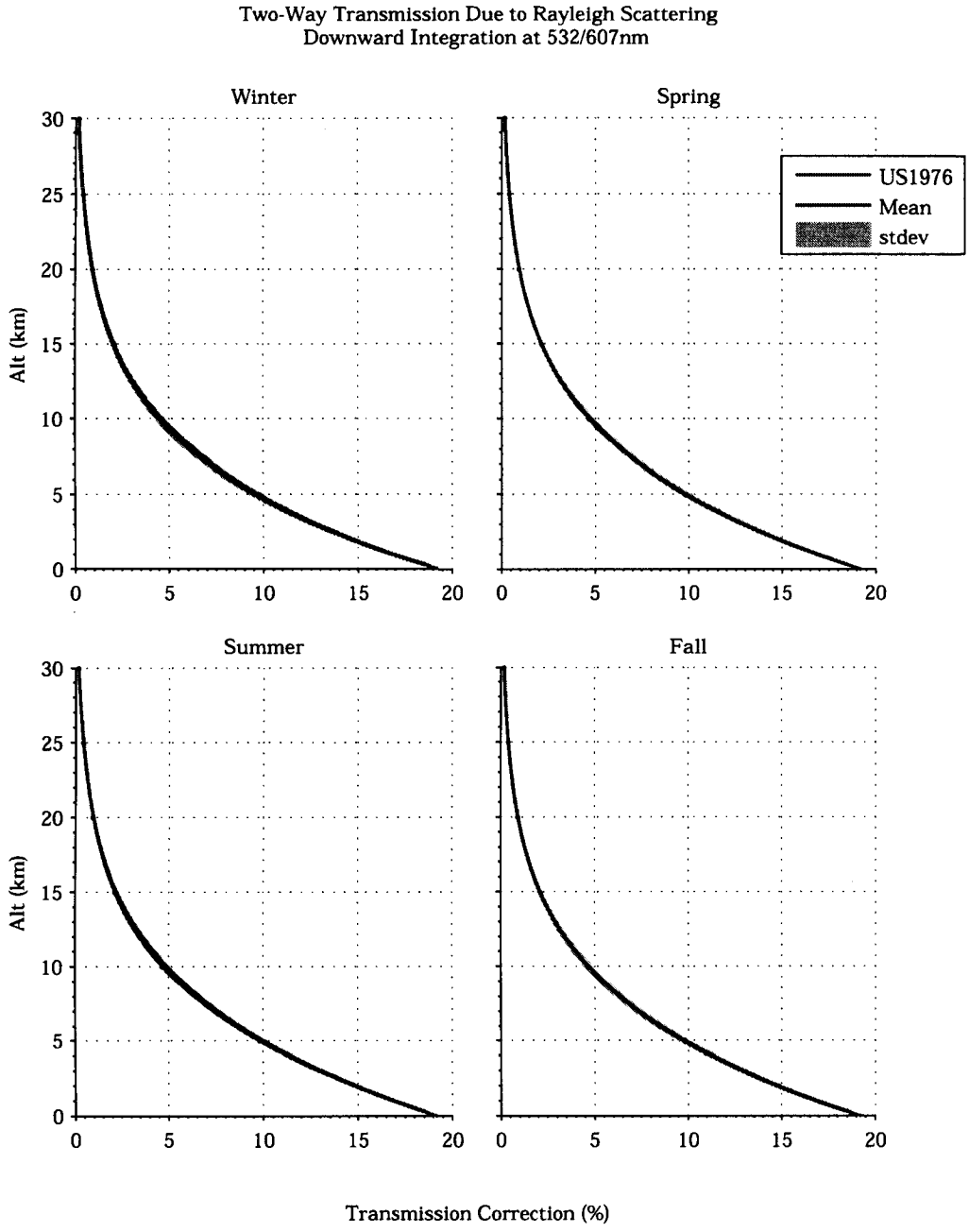

Figure A.1: Two-way transmission profiles due to Rayleigh scattering at 532/532 nm. The profiles are normalized to 50 km and expressed as a difference of percentage (relative to 100% at 50 km).

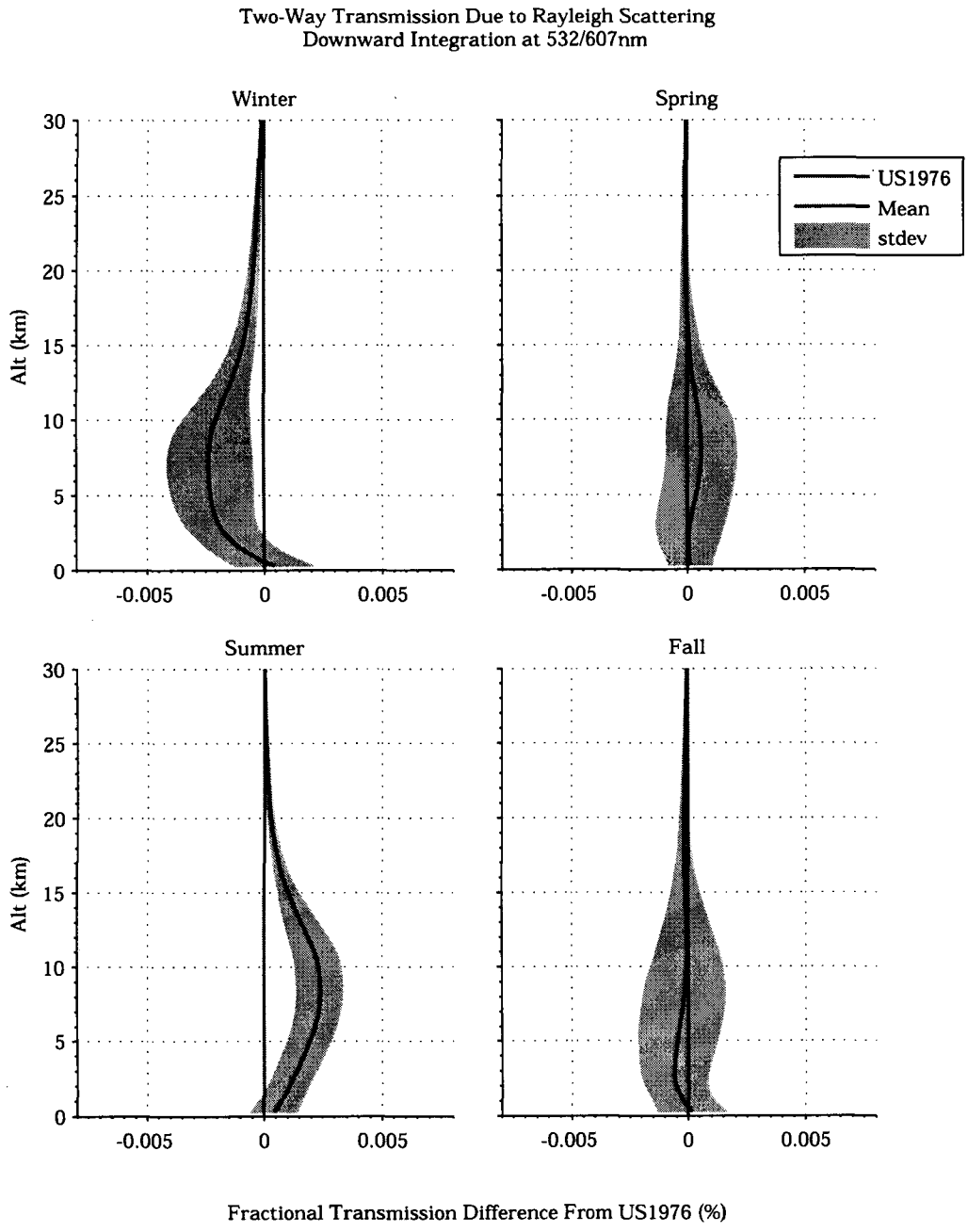

Figure A.2: Two-way transmission profiles due to Rayleigh scattering at 532/607 nm based on quarterly-averaged radiosonde measurements expressed relative to US1976.

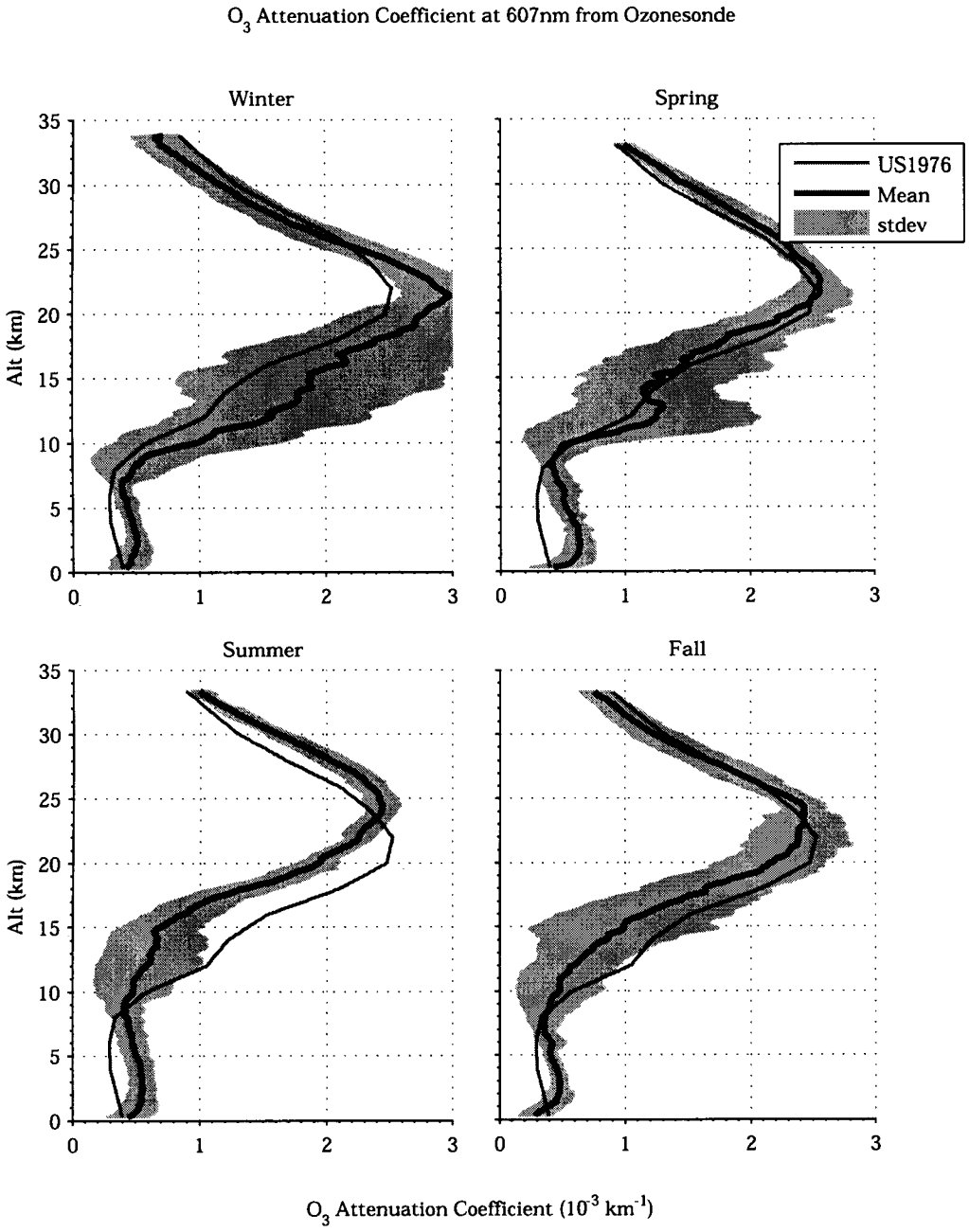

Figure A.3: Quarterly ozone extinction coefficient profiles calculated at 607 nm using ozonesonde profiles. The standard deviation of the profiles is also shown.

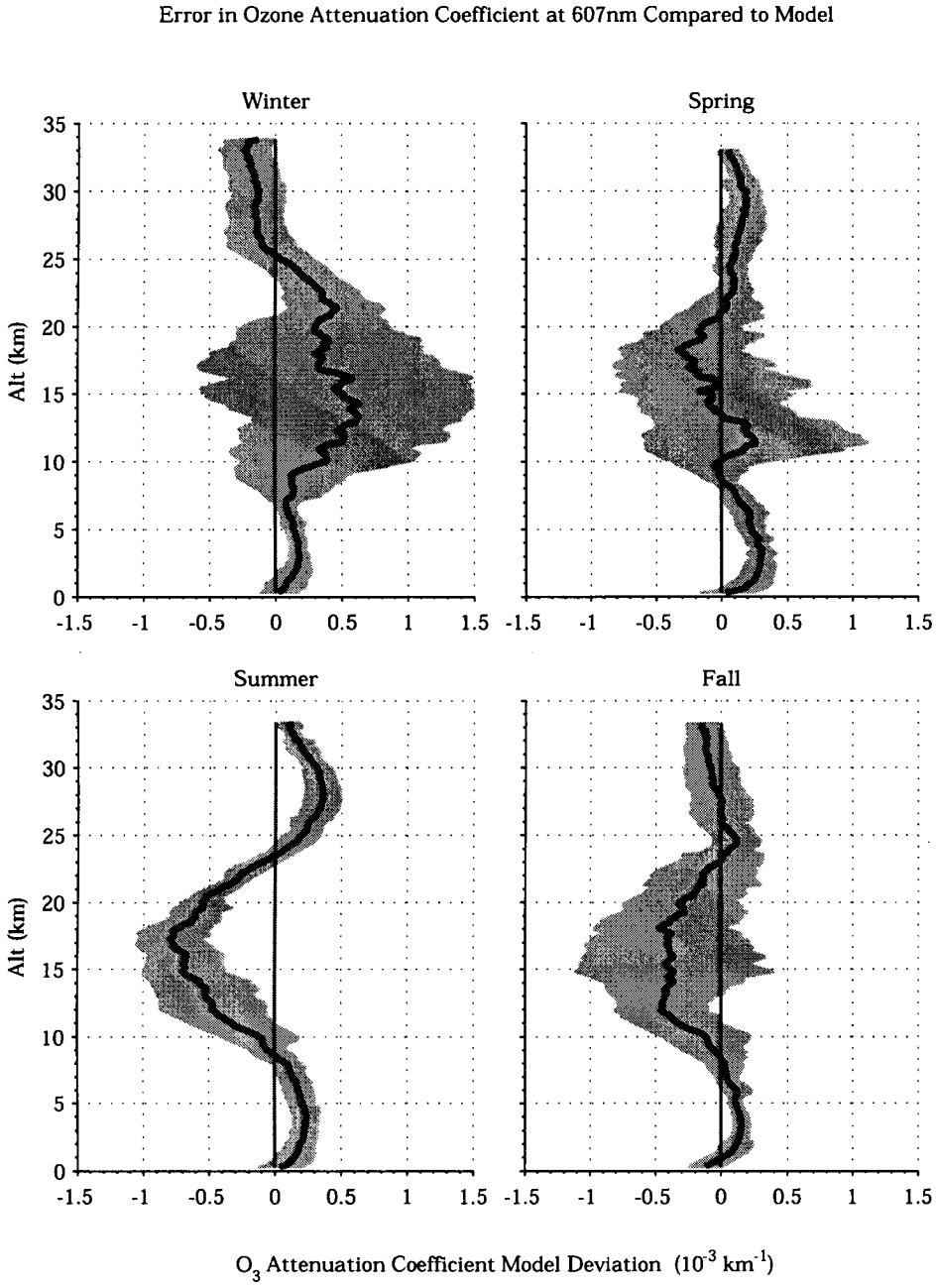

Figure A.4: Difference in quarterly ozone extinction calculated using ozonesonde profiles from US1976 at 607 nm. Standard deviation of the profiles in each quarter is also shown.

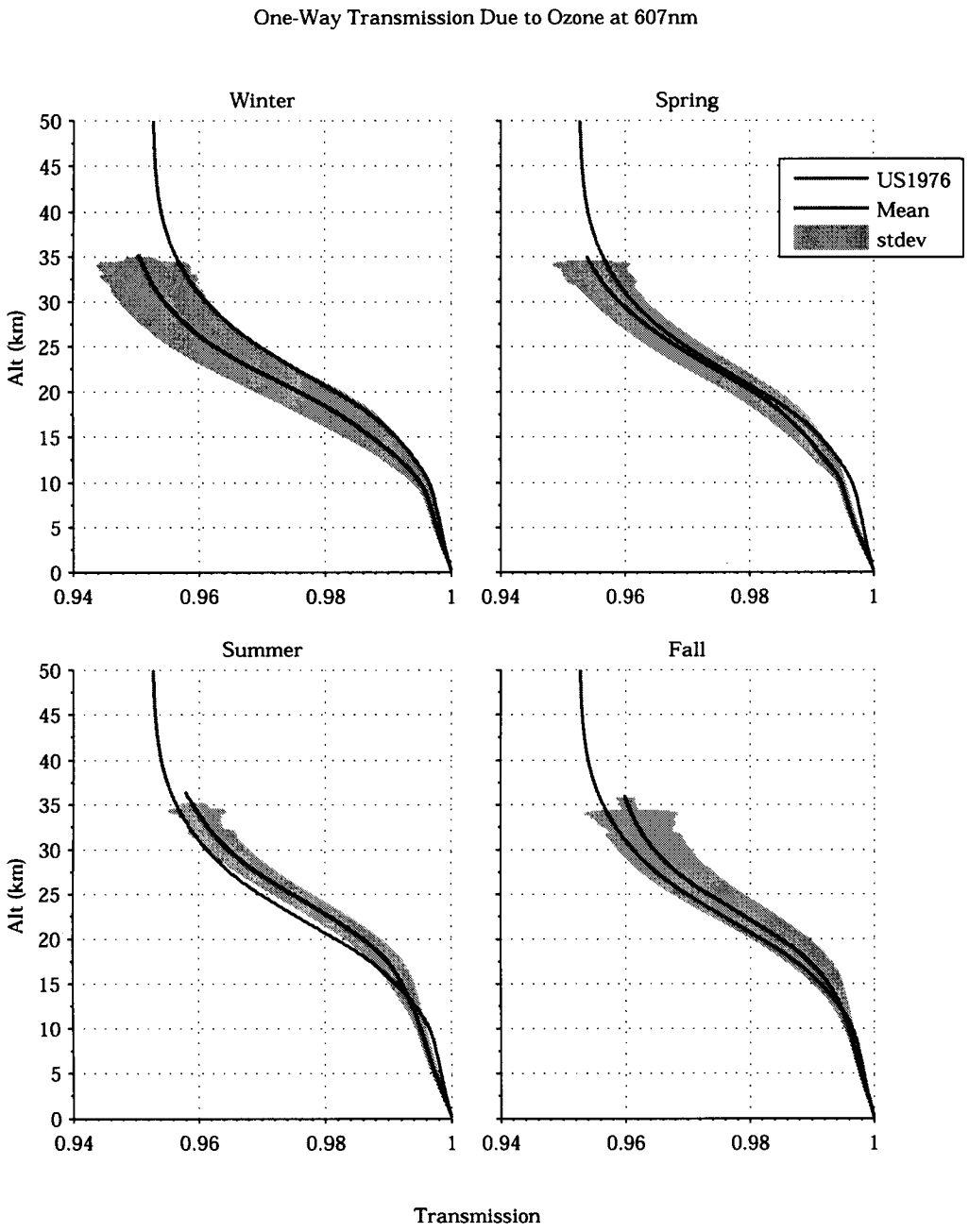

Figure A.5: Transmission decrease due to ozone at 607 nm, normalized at 300 m.

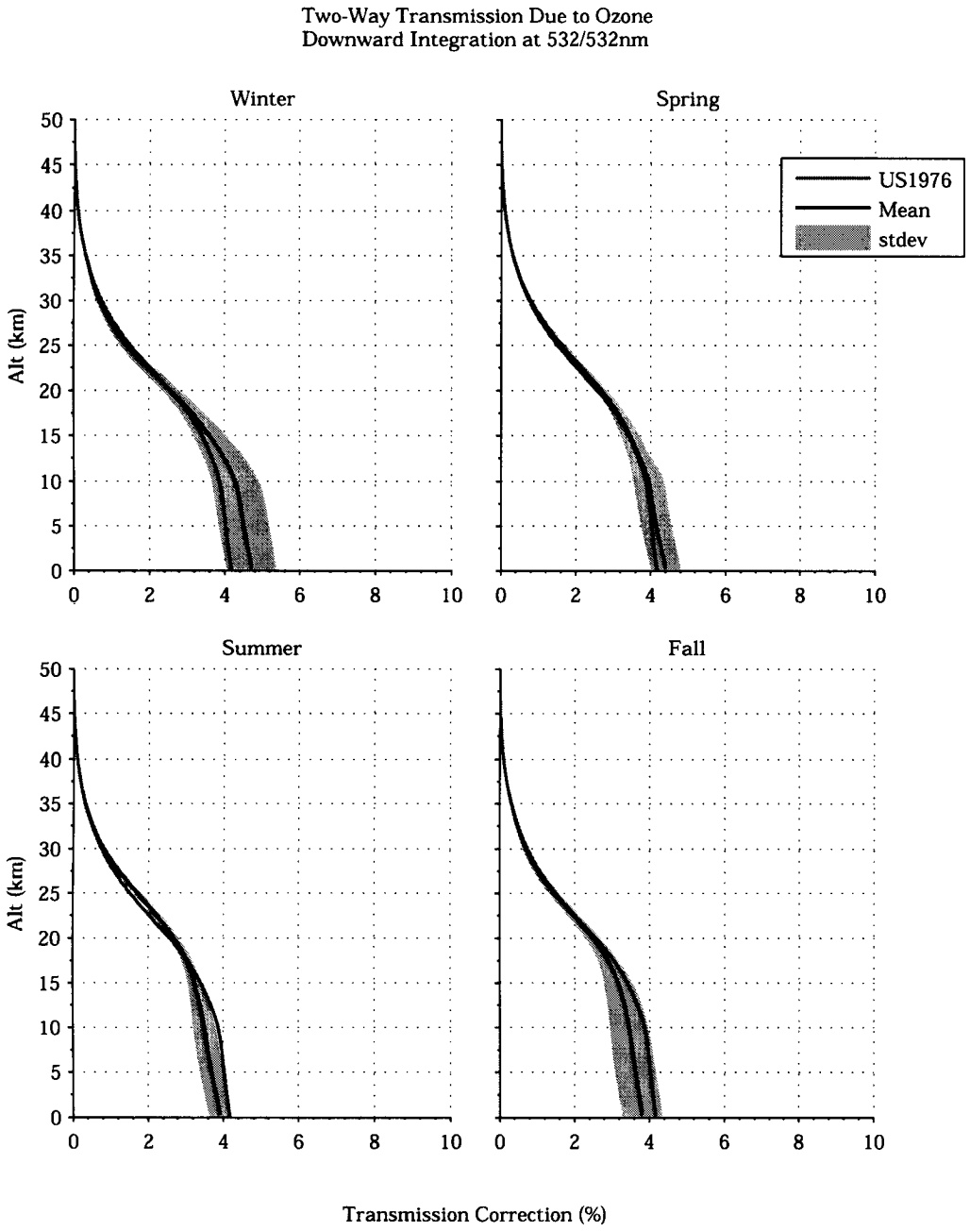

Figure A.6: Rayleigh Lidar two-way ozone transmission normalized at 50 km and expressed as a relative percentage above 100%.

Appendix B

Colour Plots

Colour versions of some figures, mainly the surface plots of the measured aerosol properties, are included here.

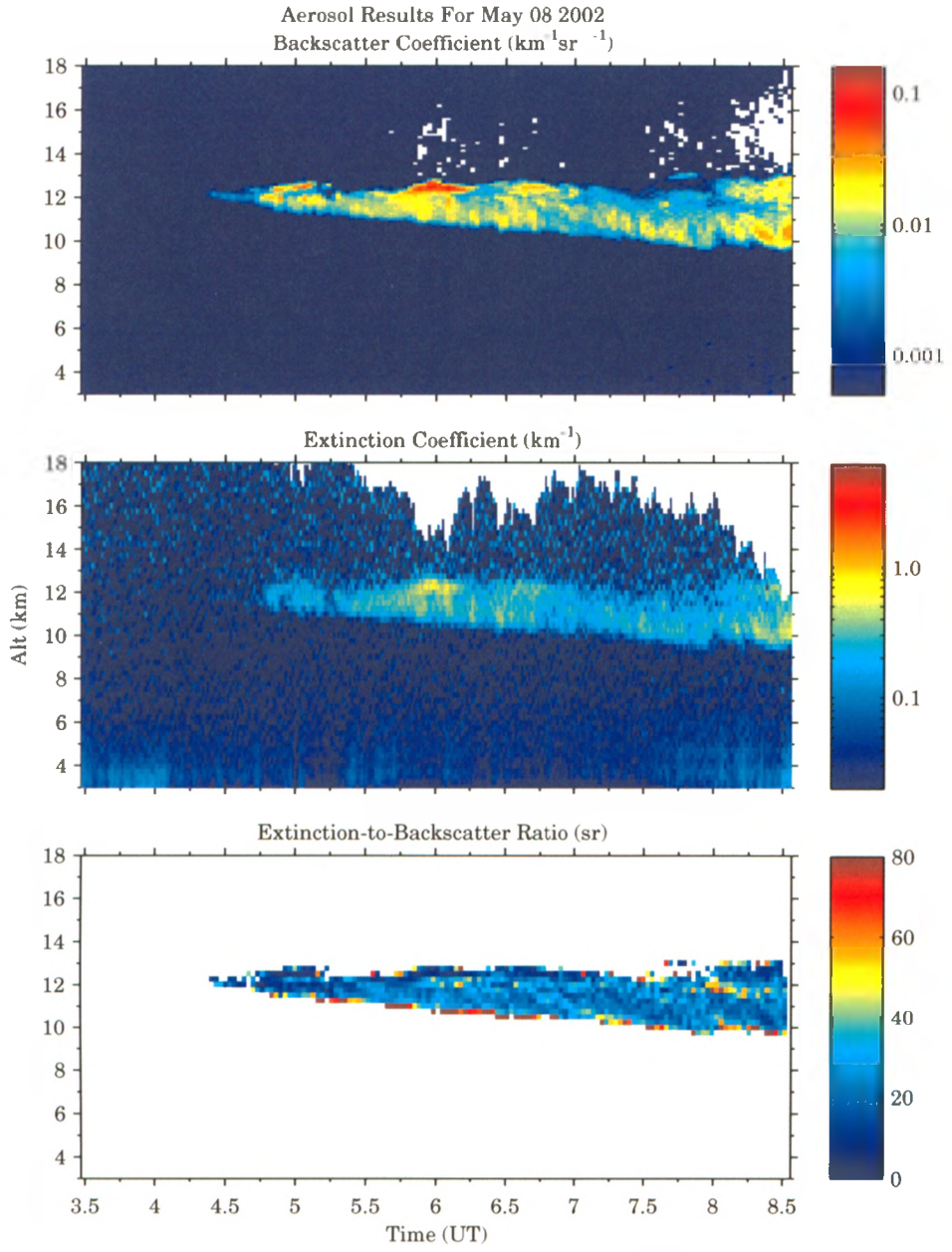

Figure B.1: Broad, 4 km-thick, Cirrostratus-like cloud at 13 km. Ratio measurements possibly indicative of structure in different particle properties.

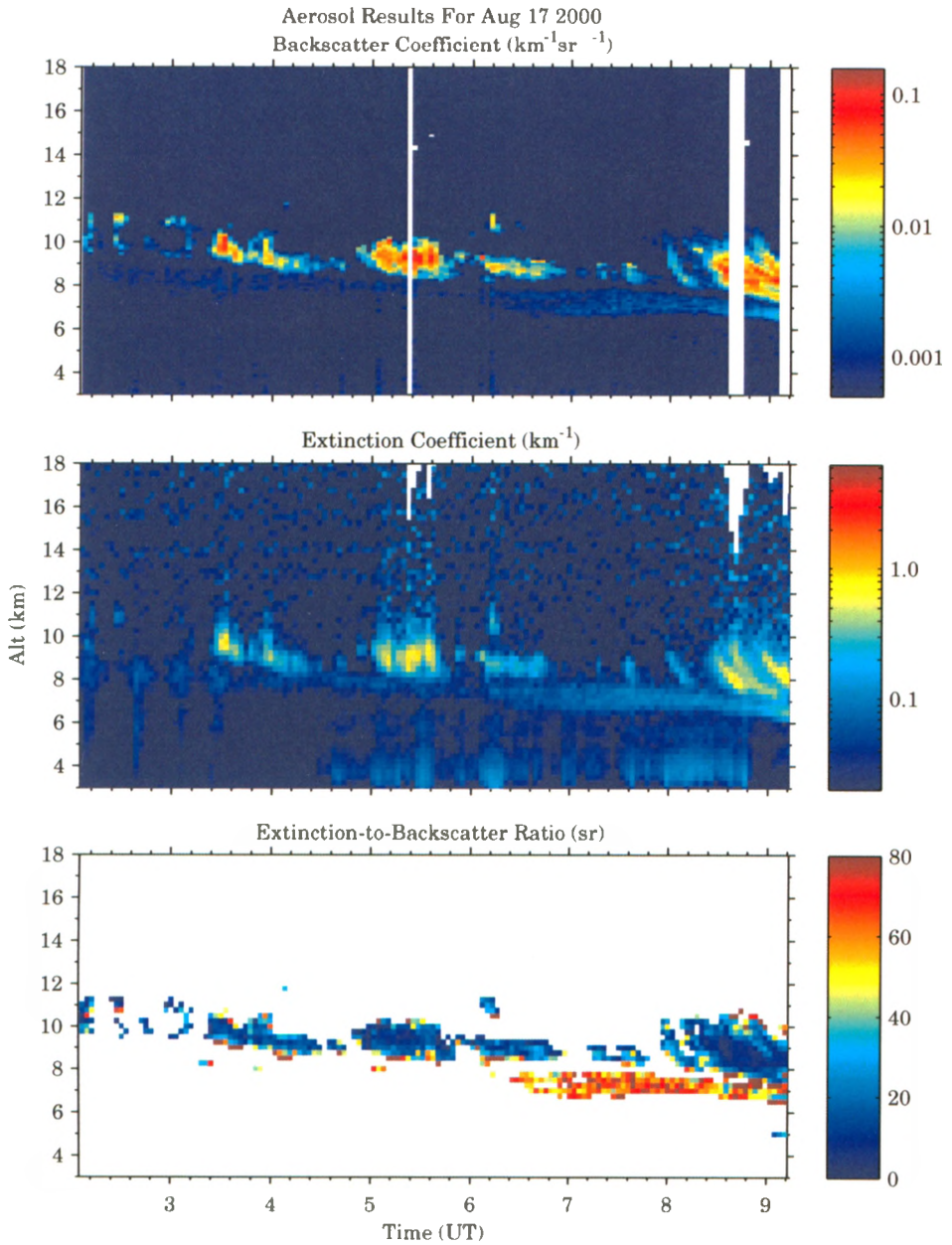

Figure B.2: Small, puffy clouds above distinct, diffuse smoke layer. Ability of E-to-B ratio to disambiguate smoke ($\bar{\mu} = 64 \pm 2$ sr, $\sigma = 18$ sr) and clouds ($\mu = 18.2 \pm 0.5$ sr $\sigma = 9$ sr) is demonstrated.

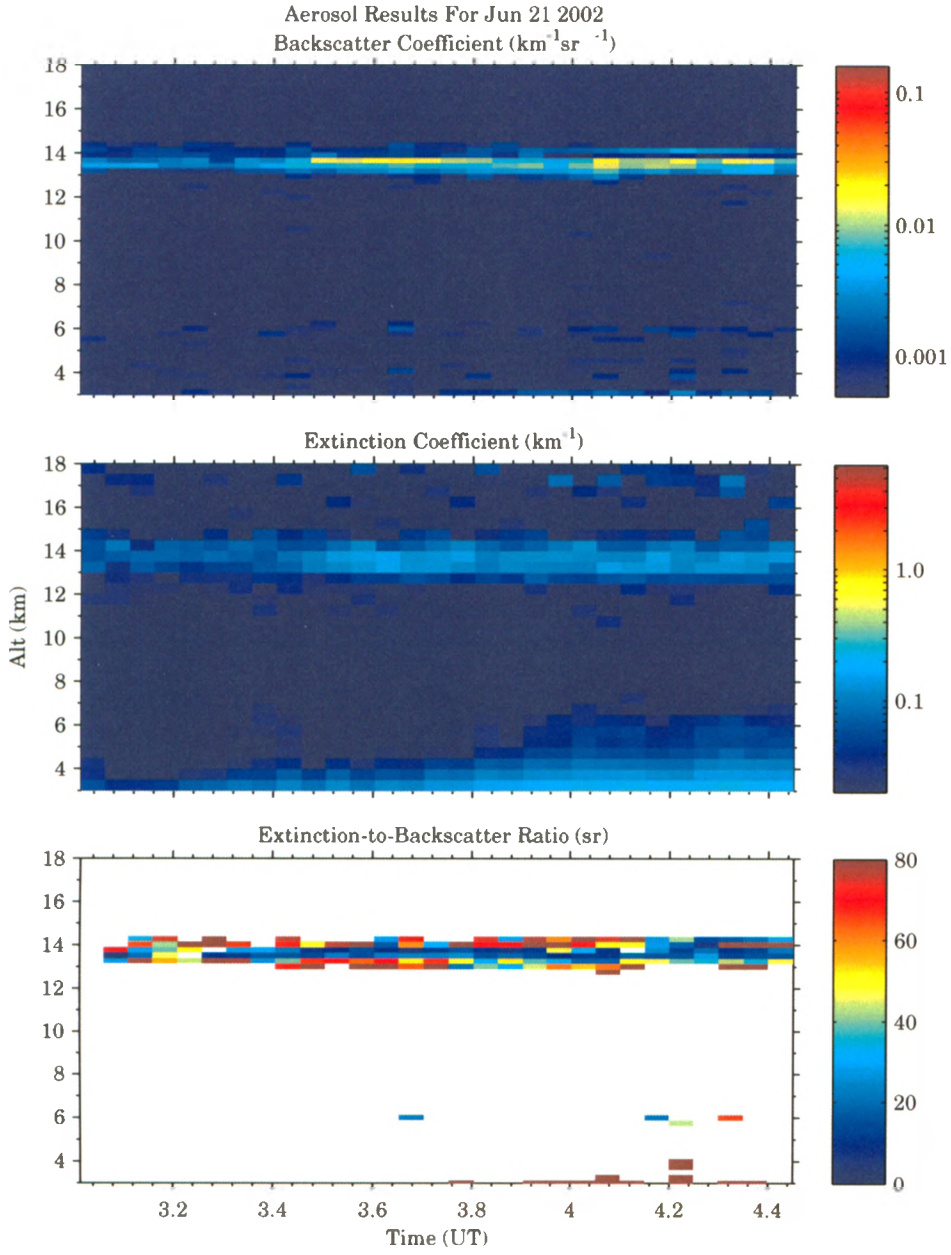

Figure B.3: Layer feature of high E-to-B ratio with strongly scattering region embedded inside. Interpreted as smoke with entrained water/ice. Some noisy but detectable measurements are present below the colour range of the plots (refer to mean profile plot).

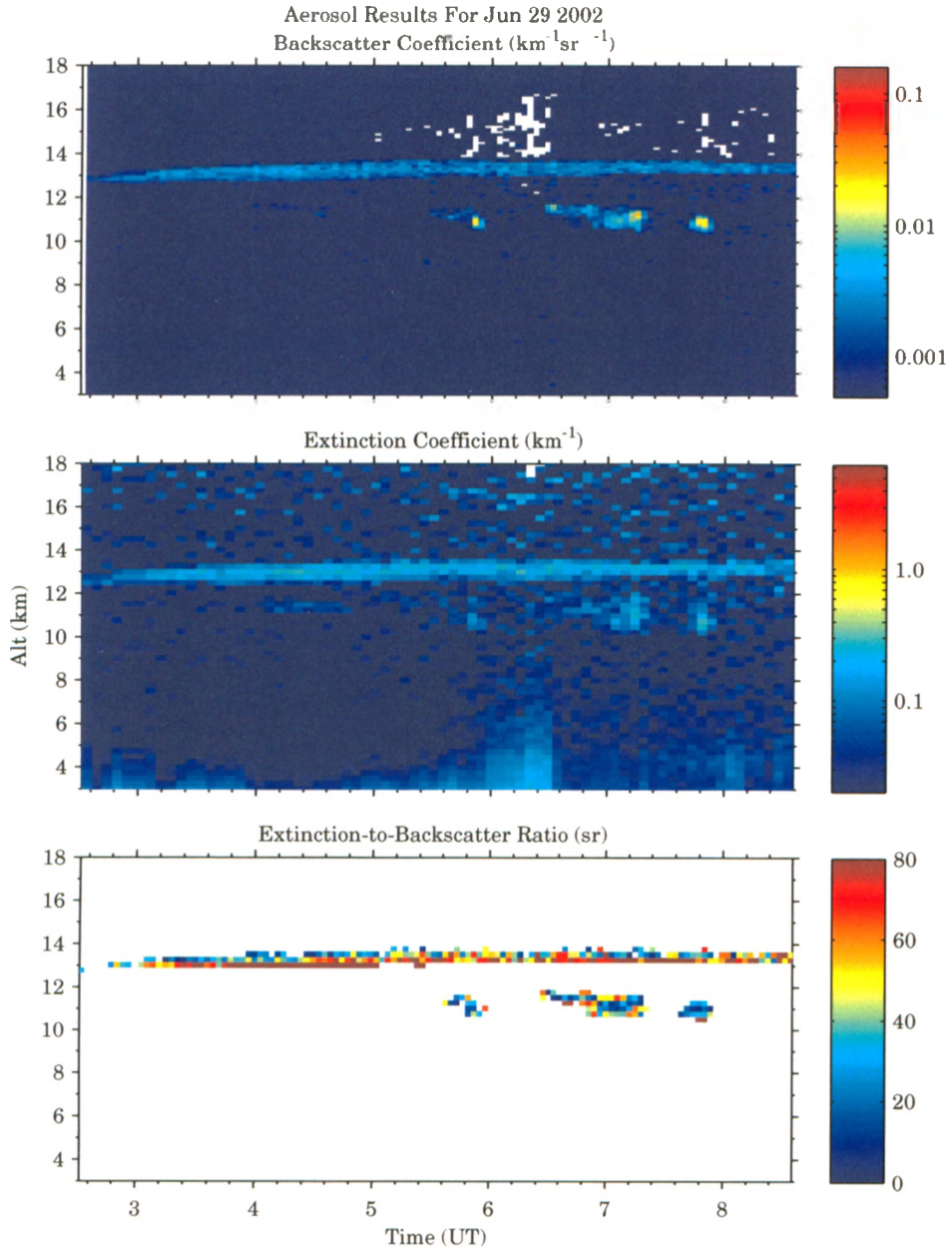

Figure B.4: Prominent layer feature topping at 13.5 km. Fairly diffuse with relatively strong extinction. Ratio is high, but calculation at edges is inconsistent – problematic due to narrow extent.

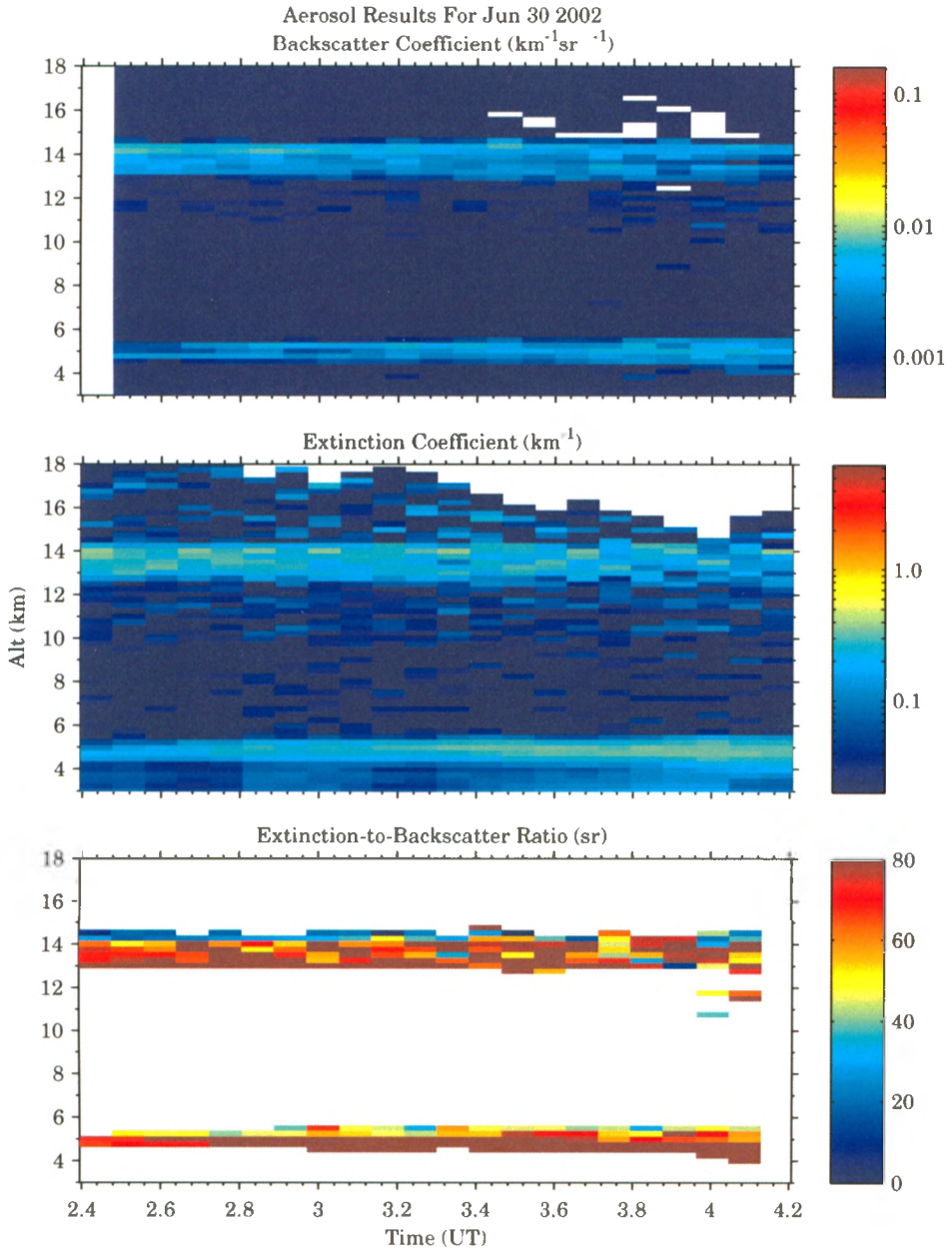

Figure B.5: Fairly bright layer feature with even stronger extinction. Definitely smoke. Distinct bright upper portion above dimmer lower section, with sharp boundary at 12.5 km.

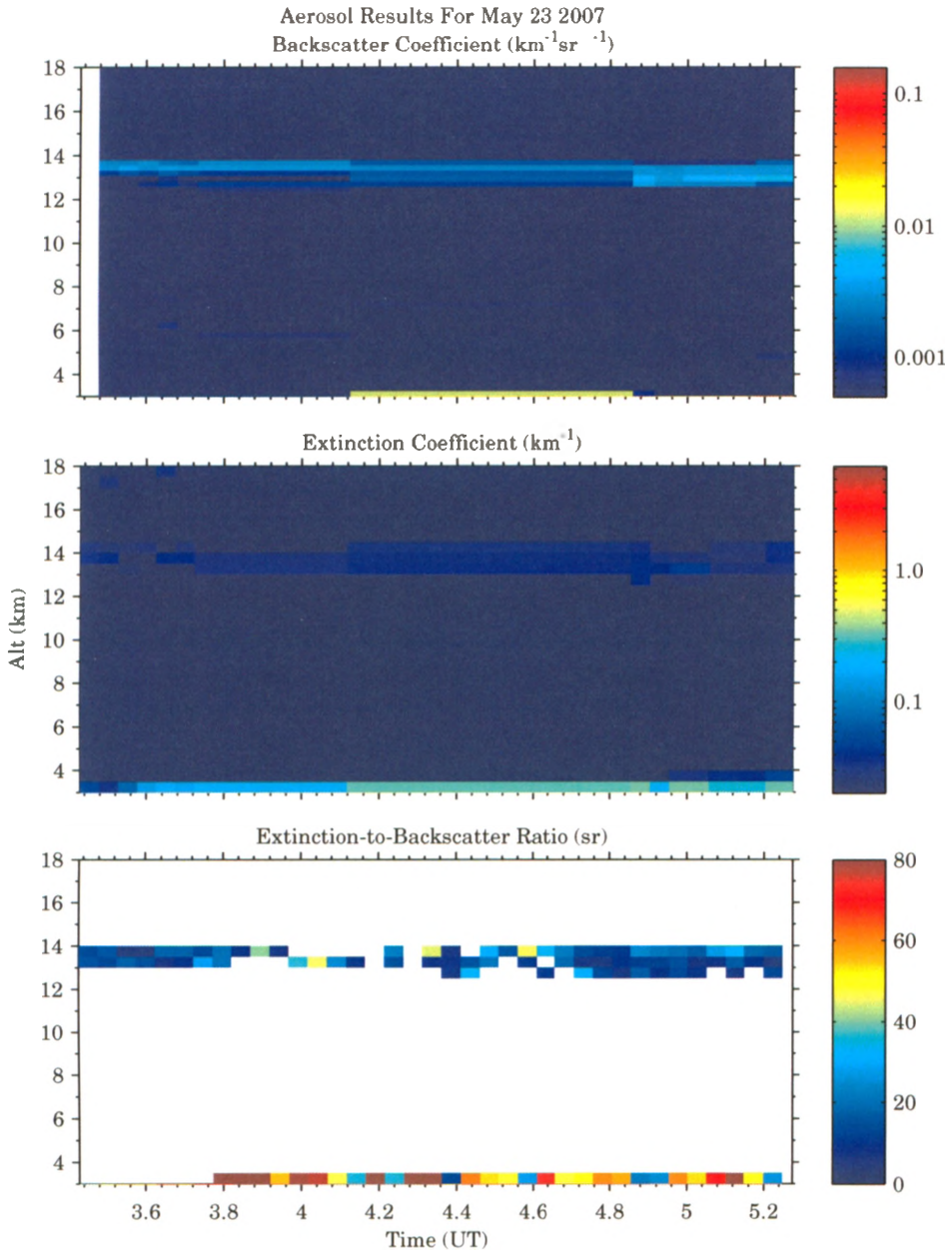

Figure B.6: Thin, extended, diffuse, high-altitude layer that was a strong candidate for smoke based on the backscatter data. Low extinction measurements and corresponding ratio, however, successfully resolved this as a thin cirrus cloud.

Bibliography

Amiridis, V., Balis, D. S., Giannakaki, E., Stohl, A., Kazadzis, S., Koukouli, M. E., and Zanis, P. (2009). Optical characteristics of biomass burning aerosols over southeastern europe determined from uv-raman lidar measurements. *Atmospheric Chemistry and Physics*, 9(7):2431–2440.

Ansmann, A., Riebesell, M., and Weitkamp. C. (1990). Measurement of atmospheric aerosol extinction profiles with a raman lidar. *Opt. Lett.*, 15(13):746–748.

Ansmann, A., Wandinger, U., Riebesell, M., Weitkamp, C., and Michaelis, W. (1992). Independent measurement of extinction and backscatter profiles in cirrus clouds by using a combined raman elastic-backscatter lidar. *Appl. Opt.*, 31(33):7113.

Ansmann, A., Wandinger, U., and Weitkamp, C. (1993). One-year observations of mount-pinatubo aerosol with an advanced raman lidar over germany at 53.5 deg n. *Geophysical Research Letters*, 20:711–714.

Argall, P. S., Sica, R. J., Bryant, C. R., Algara-Siller, M., and Schijns, H. (2007). Calibration of the Purple Crow Lidar vibrational Raman water-vapour mixing ratio and temperature measurements. *Canadian Journal of Physics*, 85:119–129.

Berk, A., Bernstein, L., and Robertson, D. (1989). Modtran: A moderate resolution model for lowtran 7. Technical report gl-tr-89-0122, Air Force Geophysics Laboratory, Hanscom AFB, MA.

Bogumil, K., Orphal, J., Homann, T., Voigt, S., Spietz, P., Fleischmann, O. C., Vogel, A., Hartmann, M., Kromminga, H., Bovensmann, H., Frerick, J., and Burrows, J. P. (2003). Measurements of molecular absorption spectra with the sciamachy pre-flight model: instrument characterization and reference data for atmospheric remote-sensing in the 230-2380 nm region. *Journal of Photochemistry and Photobiology A: Chemistry*, 157(2-3):167 – 184.

Bucholtz, A. (1995). Rayleigh-scattering calculations for the terrestrial atmosphere. *Appl. Opt.*, 34(15):2765–2773.

Chen, W.-N., Chiang, C.-W., and Nee, J.-B. (2002). Lidar ratio and depolarization ratio for cirrus clouds. *Appl. Opt.*, 41(30):6470–6476.

Ferrare, R. A., Turner, D. D., Brasseur, L. H., Feltz, W. F., Dubovik, O., and Tooman, T. P. (2001). Raman lidar measurements of the aerosol extinction-to-backscatter ratio over the Southern Great Plains. *Journal of Geophysical Research*, 106:20333–20348.

Fromm, M. D., Kittaka, C., Vaughan, M., Eloranta, E. W., Ritter, C., Hoffmann, A., and Fricke, K. H. (2008). Plumes cover the northern hemisphere: lidar views of summer 2008 volcanic and pyroconvective injections. *AGU Fall Meeting Abstracts*, pages A1+.

Johnson, N. L., Kemp, A. W., and Kotz, S. (2005). *Univariate discrete distributions*. John Wiley and Sons.

Jost, H.-J., Drdla, K., Stohl, A., Pfister, L., Loewenstein, M., Lopez, J. P., Hudson, P. K., Murphy, D. M., Cziczo, D. J., Fromm, M., Bui, T. P., Dean-Day, J., Gerbig, C., Mahoney, M. J., Richard, E. C., Spichtinger, N., Pittman, J. V., Weinstock, E. M., Wilson, J. C., and Xueref, I. (2004). In-situ observations of mid-latitude forest fire plumes deep in the stratosphere. *Geophys. Res. Lett.*, 31:11101–+.

Kantor, A. J. and Cole, A. E. (1962). Mid-latitude atmospheres, winter and summer. *Pure and Applied Geophysics*, 53:171–188.

Klett, J. D. (1981). Stable analytical inversion solution for processing lidar returns. *Appl. Opt.*, 20(2):211–220.

Knapp, D. J., Weinheimer, A. J., and Ridley, B. A. (2005). In-situ Observations of a Biomass Burning Plume in the Lower Stratosphere During the CRYSTAL-FACE Mission Flight of July 9, 2002. *AGU Fall Meeting Abstracts*, pages B857+.

Krueger, A. J. and Minzner, R. A. (1976). A mid-latitude ozone model for the 1976 u.s. standard atmosphere. *Journal of Geophysical Research*, 81:4477–4481.

Meteorological Service of Canada (2008). World ozone and ultraviolet radiation data centre (woudc). Retrieved from http://www.woudc.org.

Reagan, J. A., Apte, M. V., Ben-David, A., and Herman, B. M. (1988). Assessment of aerosol extinction to backscatter ratio measurements made at 694.3 nm in tucson, arizona. *Aerosol Science and Technology*, 8:215–226.

Schwartz, B. and Govett, M. (1992). A hydrostatically consistent north american radiosonde data base at the forecast systems laboratory, 1946-present. Technical memorandum erl fsl-4, National Oceanic and Atmospheric Administration, NOAA/ERL/FSL 325 Broadway, Boulder, CO 80303.

Sica, R. J., Sargoytchev, S., Argall, P. S., Borra, E. F., Girard, L., Sparrow, C. T., and Flatt, S. (1995). Lidar measurements taken with a large-aperture liquid mirror. 1. rayleigh-scatter system. *Appl. Opt.*, 34(30):6925–6936.

Sica, R. J., Zylawy, Z. A., and Argall, P. S. (2001). Ozone Corrections for Rayleigh-Scatter Temperature Determinations in the Middle Atmosphere. *Journal of Atmospheric and Oceanic Technology*, 18:1223–1228.

Solomon, S., Qin, D., Manning, M., Chen, Z., Marquis, M., Averyt, K., Tignor, M., and Miller, H., editors (2007). *Contribution of Working Group I to the Fourth Assessment Report of the Intergovernmental Panel on Climate Change*. Cambridge University Press, New York.

US Standard Atmosphere (1976). U.s. standard atmosphere, 1976. Technical report, National Aeronautics and Space Administration, Washington, DC.

Wandinger, U. and Ansmann, A. (2002). Measurement of atmospheric aerosol extinction profiles with a raman lidar. *Appl. Opt.*, 41(3):511–514.

Westphal, D. L., Chen, H., Campbell, J. R., Richardson, K., Doyle, J. D., and Fromm, M. D. (2008). Numerical Investigation and Forecasting of the Kasatochi Ash Plume. *AGU Fall Meeting Abstracts*, pages B267+.

Winker, D. M. e. a. (2008). Caliop algorithm theoretical basis document document no: Pc-sci-202 parts 1-4. Technical report, National Aeronautics and Space Administration, Washington, DC.